

# **Uncertainty Quantification and Reduction in Cardiac Electrophysiological Imaging**

by

Azar Rahimi Dehaghani

A dissertation submitted in partial fulfillment of the  
requirements for the degree of Doctor of Philosophy  
in the B. Thomas Golisano College of  
Computing and Information Sciences  
Rochester Institute of Technology

Author signature

Date

Approved by

Director of Ph.D. Program

Date

April 2015

Rochester, NY, USA

# Certificate of Approval

The Ph.D. Degree Dissertation of Azar Rahimi Dehaghani has been examined and approved by the dissertation committee as complete and satisfactory for the dissertation requirement for Ph.D. degree in Computing and Information Sciences at B. Thomas Golisano College of Computing and Information Sciences, Rochester Institute of Technology.

---

Prof. Dana Brooks

---

Prof. Nathan Cahill

---

Prof. Anne Haake

---

Prof. Richard Zanibbi

---

Prof. Daniel Phillips

Dissertation Defense Chairperson

---

Prof. Linwei Wang

Dissertation Advisor

April 2015

# **Uncertainty Quantification and Reduction in Cardiac Electrophysiological Imaging**

by Azar Rahimi Dehaghani

April 2015

## **Abstract**

Cardiac electrophysiological (EP) imaging involves solving an inverse problem that infers cardiac electrical activity from body-surface electrocardiography data on a physical domain defined by the body torso. To avoid unreasonable solutions that may fit the data, this inference is often guided by data-independent prior assumptions about different properties of cardiac electrical sources as well as the physical domain. However, these prior assumptions may involve errors and uncertainties that could affect the inference accuracy. For example, common prior assumptions on the source properties, such as fixed spatial and/or temporal smoothness or sparseness assumptions, may not necessarily match the true source property at different conditions, leading to uncertainties in the inference. Furthermore, prior assumptions on the physical domain, such as the anatomy and tissue conductivity of different organs in the thorax model, represent an approximation of the physical domain, introducing errors to the inference. To determine the robustness of the EP imaging systems for future clinical practice, it is important to identify these errors/uncertainties and assess their impact on the solution. This dissertation focuses on the quantification and reduction of the impact of uncertainties caused by prior assumptions/models on cardiac source properties as well as anatomical modeling uncertainties on the EP imaging solution.

To assess the effect of fixed prior assumptions/models about cardiac source properties on the solution of EP imaging, we propose a novel yet simple  $L_p$ -norm regularization method for volumetric cardiac EP imaging. This study reports the necessity of an adaptive prior model (rather than fixed model) for constraining the complex spatiotemporally changing properties of the cardiac sources. We then propose a multiple-model Bayesian approach to cardiac EP imaging that employs a continuous combination of prior models, each reflecting a specific spatial property for volumetric sources. The 3D source estimation is then obtained as a weighted combination of solutions across all models.

Including a continuous combination of prior models, our proposed method reduces the chance of mismatch between prior models and true source properties, which in turn enhances the robustness of the EP imaging solution.

To quantify the impact of anatomical modeling uncertainties on the EP imaging solution, we propose a systematic statistical framework. Founded based on statistical shape modeling and unscented transform, our method quantifies anatomical modeling uncertainties and establish their relation to the EP imaging solution. Applied on anatomical models generated from different image resolutions and different segmentations, it reports the robustness of EP imaging solution to these anatomical shape-detail variations. We then propose a simplified anatomical model for the heart that only incorporates certain subject-specific anatomical parameters, while discarding local shape details. Exploiting less resources and processing for successful EP imaging, this simplified model provides a simple clinically-compatible anatomical modeling experience for EP imaging systems.

Different components of our proposed methods are validated through a comprehensive set of synthetic and real-data experiments, including various typical pathological conditions and/or diagnostic procedures, such as myocardial infarction and pacing.

Overall, the methods presented in this dissertation for the quantification and reduction of uncertainties in cardiac EP imaging enhance the robustness of EP imaging, helping to close the gap between EP imaging in research and its clinical application.

# Acknowledgements

I would like to express the deepest appreciation to my advisor, Prof. Linwei Wang, for the support, encouragement, inspiration and guidance she provided me throughout my graduate study.

I am grateful to my graduate committee: Profs. Dana Brooks, Nathan Cahill, Anne Haake, and Richard Zanibbi for their insightful comments.

My appreciation goes to my colleagues and good friends Hongda Mao, Mohamed Elshrif, Jingjia Xu, and Ken C.L. Wong, for the useful and stimulating discussions and their pleasant company.

My sincere thanks also go to my friends Yasamin Mokri and Shiva Salek for their priceless presence and support.

Lastly, I would like to express my gratitude to my dear parents, and my sisters for their support, love, presence, and patience.

The work presented in this dissertation is supported by grants from the National Science Foundation, the National Institute of Heart, Lung, and Blood of the National Institutes of Health, and the Howard Hughes Medical Institute.

# Contents

<b>Abstract</b>	<b>ii</b>
<b>Acknowledgements</b>	<b>iv</b>
<b>List of Figures</b>	<b>viii</b>
<b>List of Tables</b>	<b>xii</b>
<b>Abbreviations</b>	<b>xiii</b>
<b>Symbols</b>	<b>xv</b>
<b>1 Introduction</b>	<b>1</b>
1.1 Problem Definition . . . . .	2
1.1.1 Uncertainties in Prior Assumptions on Cardiac Properties . . . . .	4
1.1.2 Uncertainties in Prior Assumptions on the Volume Conductor . . .	5
1.2 Dissertation Contribution . . . . .	6
1.2.1 Addressing Uncertainties in Prior Assumptions on Source Properties	6
1.2.2 Addressing Uncertainties of Anatomical Modeling . . . . .	7
1.3 Dissertation Organization . . . . .	8
<b>2 Background and Related Works</b>	<b>9</b>
2.1 Cardiac Electrophysiology . . . . .	9
2.2 Imaging Cardiac Electrophysiology . . . . .	10
2.2.1 Electrocardiography . . . . .	10
2.2.2 Body-Surface Potential Mapping . . . . .	12
2.2.3 Cardiac Mapping . . . . .	13
2.3 Computational Approaches for Imaging Cardiac Electrophysiology . . . .	14
2.3.1 Cardiac Forward Modeling . . . . .	14
2.3.2 Cardiac Inverse Electrophysiological Imaging . . . . .	16
2.3.2.1 Surface-based EP Imaging . . . . .	17
2.3.2.2 Volumetric EP Imaging . . . . .	18
<b>3 Impact of Prior Assumptions About Source Properties on Cardiac Electrophysiological Imaging</b>	<b>20</b>
3.1 Background . . . . .	20

3.2	<i>L<sub>p</sub></i> -norm Regularization . . . . .	23
3.3	<i>L<sub>p</sub></i> -SVD Regularization . . . . .	24
3.4	Experiments and Results . . . . .	25
3.4.1	Synthetic Experiments . . . . .	26
3.4.1.1	Imaging Sources with Various Sizes Using <i>L<sub>p</sub></i> -norm Regularization . . . . .	26
3.4.1.2	Imaging Source Activity Along the Border of Computer-Simulated Infarct Regions . . . . .	29
3.4.2	Real-Data Experiments on Post-infarction Patients . . . . .	33
3.5	Conclusions . . . . .	34
4	<b>4 Imaging Volumetric Cardiac Source Activity using a Hierarchical Multiple-Model Bayesian Approach</b>	36
4.1	Background . . . . .	36
4.2	Methodology . . . . .	39
4.2.1	Bayesian Inference . . . . .	39
4.2.2	Hierarchical Multiple-Model Bayesian Inference to Volumetric Cardiac Source Imaging . . . . .	41
4.2.2.1	Multiple-Model Prior Term . . . . .	41
4.2.2.2	Data Likelihood Term . . . . .	43
4.2.2.3	Sampling the Posterior using MCMC . . . . .	44
4.3	Experiments and Results . . . . .	46
4.3.1	Synthetic Experiments . . . . .	47
4.3.1.1	Imaging Cardiac Sources with Various Sizes . . . . .	48
4.3.1.2	Imaging Cardiac Source Distribution along the Infarct Border . . . . .	50
4.3.1.3	Imaging Excitation/Repolarization Wavefront in Cardiac Pacing . . . . .	53
4.3.2	Real-Data Experiments . . . . .	57
4.3.2.1	Imaging Infarct Region using MRI as Reference . . . . .	57
4.3.2.2	Imaging Infarct Region using Voltage Mapping as Reference . . . . .	60
4.4	Discussions . . . . .	62
4.5	Conclusions . . . . .	70
5	<b>5 Impact of Prior Assumptions About Anatomical Modeling on Cardiac Electrophysiological Imaging</b>	71
5.1	Background . . . . .	71
5.2	Cardiac Electrophysiological Imaging . . . . .	75
5.2.1	Surface-based EP Imaging Methods . . . . .	75
5.2.2	Transmural EP Imaging Methods . . . . .	76
5.3	Sensitivity Assessment of EP Imaging to Variations in Personalized Ventricular Shapes . . . . .	78
5.3.1	Uncertainty Quantification in Personalized Anatomical Models . . . . .	79
5.3.2	Simulation-Based Sensitivity Evaluation . . . . .	81
5.3.3	Statistical Analysis . . . . .	84
5.4	Experiments and Results . . . . .	85
5.4.1	Synthetic Experiments . . . . .	85

5.4.2 Real-Data Experiments . . . . .	92
5.5 Discussions . . . . .	96
5.6 Conclusions . . . . .	98
<b>6 Cardiac Simplified Anatomical Model</b>	<b>100</b>
6.1 Background . . . . .	100
6.2 Personalized Simplified Anatomical Model of Heart . . . . .	101
6.3 Experiments and Results . . . . .	104
6.4 Conclusions . . . . .	105
<b>7 Summary</b>	<b>107</b>
7.1 Conclusions . . . . .	107
7.2 Future Work . . . . .	110
<b>A Publications</b>	<b>112</b>
<b>Bibliography</b>	<b>115</b>

# List of Figures

2.1	Cardiac electrical conduction system [1]. . . . .	10
2.2	Standard 12-lead ECG [2]. . . . .	11
2.3	Schematic representation of normal ECG [3]. . . . .	11
2.4	Electrode positioning on the body-surface in a 120-lead Dalhousie BSPM standard [4]. . . . .	12
2.5	An example of a BSPM in both anterior and posterior view [5]. . . . .	13
3.1	Illustration of action potential and its spatial gradient during excitation phase of cardiac cycle in a healthy heart. . . . .	22
3.2	Source estimation using $L_p$ -norm regularization for $1 \leq p \leq 2$ . 58 active sources are located at left ventricle mid-anterior. Increasing the $p$ value increases the source size such that $L_1$ -norm obtains too scattered source distribution while $L_2$ -norm provides overly-diffused solution. Cardiac source magnitudes are normalized to 1. . . . .	27
3.3	Source estimation using $L_p$ -norm regularization for $1 \leq p \leq 2$ . 127 active sources are located close to the right ventricle apex. Increasing the $p$ value increases the source size such that $L_1$ -norm obtains too scattered source distribution while $L_2$ -norm provides overly-diffused solution. Cardiac magnitudes are normalized to 1. . . . .	28
3.4	Source overlap (SO, vertical axis) obtained by $L_p$ -norm ( $1 \leq p \leq 2$ , horizontal axis 1) for active sources with different sizes (1 – 100 active sources, horizontal axis 2). . . . .	29
3.5	Illustration of action potential and its spatial gradient during the ST-segment of an ECG cycle in an infarcted heart. . . . .	30
3.6	Estimation of cardiac sources localized along the infarct border using $L_p$ -SVD regularization vs. $L_p(p = 1.5)$ , $L_1$ and $L_2$ -norm counterparts at two consecutive time samples during ST-segment of an ECG cycle. . . . .	31
3.7	Estimation of cardiac sources along the infarct border using $L_p$ -SVD, $p \in \{1.2, 1.5, 1.8\}$ , vs. $L_1$ and $L_2$ -norm counterparts during ST-segment of an ECG cycle. . . . .	32
3.8	Comparison of segment overlap (SO) with respect to infarct border size. . . . .	32
3.9	Estimation of cardiac sources along the infarct border using $L_p$ -SVD ( $p = 1.5$ ) vs. $L_1$ and $L_2$ -norm regularizations for two post-infarction human subjects during the ST-segment of an ECG cycle. . . . .	34
4.1	Single variable slice sampling with stepping-out and shrinkage procedures for selecting and updating an interval. . . . .	45

4.2	Three examples of the posterior mean of reconstructed 3D sources using multiple-model prior <i>vs.</i> Laplace and Gaussian priors. Active sources are centered at the apex of LV and covered 6%, 17%, and 40% of the myocardium in A, B and C, respectively. Posterior distributions of hyperparameter $p$ for the three cases are also shown in the rightmost panel.	49
4.3	Comparison of multiple-model prior with Laplace and Gaussian priors in reconstructing active source regions with different sizes. Source size is defined in terms of percentage of the ventricular myocardium. . . . .	49
4.4	Two examples of the posterior mean estimate of the source distribution (the spatial gradient of action potential) along the infarct border during the ST segment of an ECG cycle, where the infarct is centered at the middle to apical region at the anterior wall of LV (top row) and at the apex (bottom row). The $p$ distribution obtained by our method is also shown at the rightmost panel. . . . .	51
4.5	Comparison of multiple-model prior with Laplace and Gaussian priors in reconstructing active source distribution along the infarct border. Source size represents the size of active sources along the infarct border and is defined in terms of percentage of the left ventricle. . . . .	53
4.6	An example of imaging excitation wavefront propagation in cardiac pacing at 4 time instants during the depolarization phase of an ECG cycle. The pacing point is located at the base of right ventricle. Active source region represents the spatial gradient of action potential. . . . .	54
4.7	Comparison of multiple-model prior with Laplace and Gaussian priors in reconstructing excitation and repolarization wavefronts during an example pacing in one cardiac cycle. . . . .	56
4.8	Overall comparison of multiple-model prior with Laplace and Gaussian priors in reconstructing excitation and repolarization wavefronts in three stages of an ECG cycle. . . . .	56
4.9	Estimation of cardiac source activity (non-blue color) along the infarct region border (black contour) during the ECG ST segment for 4 human subjects. Active source region represents the spatial gradient of action potential. . . . .	58
4.10	(A) CARTO map (the leftmost panel) and its spatial gradient (non-blue region) projected on the heart surface with highlighted infarct region (black contour). (B-D) Estimation of cardiac source activity (non-blue color) along the border of the infarct region. Active source region represents the spatial gradient of action potential. . . . .	61
4.11	Comparison of the presented multiple-model Bayesian approach with Brooks <i>et al.</i> multiple-constraint regularization [6] in imaging volumetric sources located at different segments of LV defined according to standard 17-segment model of LV. . . . .	63
4.12	(A) Examples of posterior distribution of two sources obtained using slice sampling. (B) Comparison of Map <i>vs.</i> posterior mean estimators for multiple-model prior as well as Laplace and Gaussian priors for the second set of synthetic experiments. . . . .	65
4.13	Correlation coefficient obtained using multiple-model prior for active sources in the presence of white Gaussian noises with different SNR levels. . . . .	67

---

5.1	Two different segmentations (red and blue contours) of one MRI slice at the short axis view. . . . .	78
5.2	Outline of the proposed approach to investigate the uncertainty of EP imaging subject to variations in personalized anatomical models. . . . .	79
5.3	Examples of anatomical variations around mean geometry model along (a) first, (b) second, and (c) third principle directions. Mean geometry model is shown in red color while the two sample geometry models are shown in white and blue. . . . .	83
5.4	ECGI solution (epicardial potential) obtained on two ventricular models for the same subject in the healthy setting, at two different time instants of cardiac depolarization and repolarization phases. . . . .	86
5.5	(a) Overlap of two ventricular models of one subject, shown in Fig. 5.4, in short-axis view from base to apex. (b) ECGI solution at two corresponding nodes on the two ventricular models in healthy setting. . . . .	87
5.6	ECGI solution (epicardial potential) obtained on two ventricular models for the same subject in the post-infarction setting, at two different time instants of cardiac depolarization and repolarization phases. . . . .	87
5.7	STD map of ECGI output on a mean anatomical model during ST segment of an ECG cycle for (a) healthy, and (b) post-infarction settings. . . . .	88
5.8	TEPI solution (transmural action potential) obtained on two ventricular models for the same subject in the healthy setting, at two different time instants of cardiac depolarization and repolarization phases. Color encodes the value of action potential. . . . .	89
5.9	(a) Overlap of two ventricular models of one subject, shown in Fig. 5.8, in short-axis view from base to apex. (b) TEPI solution at two corresponding nodes on the two ventricular models in healthy setting. . . . .	90
5.10	TEPI solution (transmural action potential) obtained on two ventricular models for the same subject in the post-infarction setting, at two different time instants of cardiac depolarization and repolarization phases. Color encodes the value of action potential. . . . .	91
5.11	STD map of TEPI output on a mean anatomical model during ST segment of an ECG cycle for (a) healthy, and (b) post-infarction settings. . . . .	92
5.12	(a) ECGI solution for two ventricular models constructed for case 3 and case 4 during depolarization. Black and red contours show the ECGI estimated and the reference infarct region, respectively. (b) STD map of ECGI output on a mean anatomical model for case 3 and case 4 at the corresponding time instants. Color encodes the value of potential magnitude. . . . .	94
5.13	(a) TEPI solution for two ventricular models constructed for case 3 and case 4. Black and red contours show the TEPI estimated and the reference infarct region, respectively. (b) STD map of TEPI output on a mean anatomical model for case 3 and case 4 at the corresponding time instants. Color encodes the value of potential magnitude. . . . .	95
6.1	Cardiac simplified anatomical model . . . . .	103
6.2	ECGI solution for simplified ventricular models of case 3 and case 4 during depolarization. Black and red contours show the ECGI estimated and the reference infarct region, respectively. . . . .	105

- 6.3 TEPI solution for simplified ventricular models of case 3 and case 4. Black and red contours show the TEPI estimated and the reference infarct region, respectively. Color encodes the value of potential magnitude. . . . 106

# List of Tables

3.1	Comparison of segment overlap (SO) with respect to infarct border size. . .	32
4.1	Comparison of infarct quantification with best existing results . . . . .	59
6.1	Summary of parameters, imaging data and operation involved in the proposed simplified ventricular modeling. . . . .	104

# Abbreviations

AHA	american heart association
AT	activation time
AP	action potential
APD	action potential duration
AV node	atrioventricular node
BSP	body surface potential
BSPM	body surface potential mapping
CC	correlation coefficient
CT	computed tomography
ECG	electrocardiography
ECGI	electrocardiography imaging
EP	electrophysiology
gPC-SC	generalized polynomial chaos stochastic collocation
IECG	inverse electrocardiography
IC	infarct center
IS	infarct size
LA	left atrium
LV	left ventricle
LFN-WMN	lead-field normalized weighted minimum norm
LGE	late gadolinium enhancement
MC	monte carlo
MCMC	markov chain monte carlo
MMAE	multiple model adaptive estimation
MI	myocardial infarction
MR	magnetic resonance

MRI	magnetic resonance imaging
MAP	maximum a posteriori
PCA	principle component analysis
PC	polynomial chaos
RA	right atrium
RV	right ventricle
RE	relative error
RT	repolarization time
UT	unscented transform
SC	stochastic collocation
SNR	signal-to-noise ratio
SO	segment overlap
SOCPP	second order cone programming
SSM	statistical shape modeling
STD	standard deviation
SVD	singular value decomposition
SA node	sinoatrial node
TMP	transmembrane potential
TEPI	transmural electrophysiological imaging
WGN	white Gaussian noise

# Symbols

symbol	name
$\Phi$	body surface potential
$\mathbf{H}$	forward transfer matrix
$\mathbf{v}$	cardiac bioelectrical sources
$\mathbf{u}$	action potential
$\mathbf{R}_\lambda$	regularization matrix
$\ \cdot\ $	norm of a vector
$\lambda$	regularization parameter
$\ \cdot\ _p$	norm $p$ of a vector
$\mathbf{T}$	temporal basis function
$\tilde{\mathbf{v}}$	projection of bioelectrical sources to the temporal basis
$\tilde{\Phi}$	projection of body surface potential to the temporal basis
$\mathbf{U}$	spatial basis function of body surface potential
$\mathbf{S}$	singular value of body surface potential
$p$	norm order
$\mathbf{n}$	measurement noise
$m$	number of body surface measurements
$n$	number of cardiac sources
$\mathbf{P}(\cdot)$	probability density function
$\mathbf{P}(\cdot \cdot)$	conditional probability density function
$\Theta$	hyperparameters
$\delta$	source variance
$v_i$	current source at node $i$
$\Sigma$	covariance of measurement noise
$\bar{v}$	mean of a vector

---

$\bar{\mathbf{x}}$	mean shape
$\mathbf{x}_i$	sample geometry in training set
$\mathbf{P}_{\mathbf{x}}$	covariance of geometry models
$(x_i, y_i, z_i)$	coordinates of surface node $i$ representing the geometry
$S$	number of geometry models in training set
$\mathcal{X}_i$	sample geometry
$\mathcal{W}_i$	weight for sample $i$
$\mathcal{N}(.,.)$	Normal distribution
$L$	dimension of the geometry
$\Psi$	eigenvector
$\lambda$	eigenvalue
$\tilde{\mathbf{P}}_{\mathbf{x}}$	approximated covariance matrix
$\lambda_i$	element $i$ in eigen value vector
$\psi_i$	eigenvector $i$
$c$	number of eigenvalues selected
$\mathcal{Y}_i$	EP outcome of sample geometry $\mathcal{X}_i$
$\bar{\mathbf{y}}$	mean of EP samples
$\mathbf{P}_{\mathbf{y}}$	covariance of EP samples
$H_0$	Null hypothesis
$H_1$	Alternative hypothesis
$\theta$	accuracy measure for hypothesis test
$d\theta$	accuracy difference
$(\epsilon_0, \eta_0, \zeta_0)$	center of LV base
$R_{Lendo}$	radius of LV endocardium
$R_{Lepi}$	radius of LV epicardium
$a_l$	ellipticity of the LV shape
$\epsilon - \eta$	short-axis plane
$\zeta$	long axis of the heart
$(\epsilon_0^r, \eta_0^r, \zeta_0^r)$	center of the two concentric circles representing the free wall of RV endocardium
$R_{Rendo}$	radius of right ventricle endocardium
$R_{Rep}$	radius of right ventricle epicardium
$d_r$	distance between $(\epsilon_0, \eta_0, \zeta_0)$ and $(\epsilon_0^r, \eta_0^r, \zeta_0^r)$

$a_r$	elongation of the RV shape
$\phi_e$	extracellular potential
$\Omega_h$	heart volume
$u$	action potential
$\mathbf{r}$	spatial coordinate
$\mathbf{D}_{int}$	intracellular conductivity tensors
$\mathbf{D}_{ext}$	extracellular conductivity tensors
$\mathbf{D}_k$	bulk conductivity tensor
$\phi_i$	potential distributed within the volume conductor $\Omega_i$ external to the heart
$\Omega_i$	volume conductor external to the heart
$\mathbf{D}_i$	conductivity tensor
$\Omega_{t/h}$	total volume external to heart
$\sigma_{blk}$	isotropic bulk conductivity
$\sigma_t$	torso conductivity value
$\Gamma_h$	heart surface
$\Gamma_t$	torso surface

*To my parents,  
for their endless love and support.*

# Chapter 1

## Introduction

Inverse problems are solved across many science and engineering domains by making inferences about the physical system under study from a set of observed data. To eliminate unreasonable solutions that may fit the data, these inferences often need to be guided by data-independent prior knowledge/assumptions about the physical system under study. However, the prior knowledge, independent from measurement data, includes errors and uncertainties that could lead to potential model-data mismatch and affect the inference accuracy. To make an accurate inference, it is important to identify and quantify uncertainties in the prior assumptions, assess their impact on the solution, and develop algorithmic techniques to address the robustness of the inference to these uncertainties.

This dissertation focuses on the quantification and reduction of the impact of uncertainties caused by prior knowledge/assumptions on the statistical inference. It will be carried out in the context of cardiac inverse problem, also known as cardiac electrophysiological (EP) imaging, findings of which determine the robustness of cardiac EP imaging systems.

## 1.1 Problem Definition

Cardiac electrophysiological (EP) imaging, also known as the cardiac inverse problem, is a non-invasive technique used to mathematically estimate cardiac electrical activity from body-surface electrocardiography (ECG) measurements on physical domains of heart and torso. This line of research emerged to address the limitations of current clinical techniques such as ECG and catheter mapping in monitoring and diagnosis of cardiac dysfunctions. ECG provides non-invasive measurements of voltage changes on the body surface which, when displayed over time, can provide diagnostic information about cardiac electrophysiological dysfunctions. However, ECG data is obtained at very low spatial resolution (typically 12-lead recordings), lacking the regional detailed information about cardiac electrical propagation required for interventional therapies such as localization and ablation of the arrhythmogenic substrate. For this purpose, catheter mapping, the invasive counterpart of ECG, is employed in the current clinical setting to directly record the voltage measures at different locations on the heart surfaces. However, this laborious point-to-point mapping procedure is invasive and time-consuming and places the patient at the risk of fatal arrhythmia and exposure to fluoroscopy radiation [7–9]. It also requires a point-by-point mapping procedure that does not allow simultaneous beat-to-beat mapping. As a result, the acquired information requires skillful aggregation and annotation of the clinicians. Furthermore, the catheter mapping technique provides a poor surface surrogate for the transmural electrical events. To overcome the limitations associated with the paradigm of invasive mapping, cardiac EP imaging is developed that *non-invasively* provides a *beat-to-beat* estimation of cardiac electrical dynamics with high spatial resolution.

However, cardiac EP imaging involves solving an inverse problem that is notoriously

ill-posed. This ill-posedness is caused by three different factors: 1) the limited number of ECG measurements compared to the large degree of freedom in the unknown sources, 2) attenuation and smoothing effect of the torso volume conductor, and 3) the underlying biophysics of the problem [10]: even with virtually continuous measurements on the body surface, this problem still lacks a unique solution because, in a *quasi-static* electromagnetic field, different configurations of 3D sources may produce the same surface measurements [11].

This ill-posed inverse problem is often regularized, in a deterministic or non-deterministic form, by incorporating prior knowledge/assumptions about the cardiac electrical sources and the physical domains of heart and torso. Representing the cardiac inverse problem as  $\Phi = \mathbf{H}\mathbf{v}$ , this regularization, in its most general deterministic form, can be formulated as:

$$\min_{\mathbf{v}} \|\Phi - \mathbf{H}\mathbf{v}\| + \|\mathbf{R}_\lambda \mathbf{v}\| \quad (1.1)$$

where  $\Phi$  is input body-surface ECG measurements and  $\mathbf{v}$  denotes the unknown cardiac sources.  $\mathbf{H}$  represents volume conductor model (defining the physical domains of heart and torso) that contains patient-specific anatomical information as well as physical properties of different tissues in the body.  $\mathbf{R}_\lambda$  is the regularization matrix.

Prior assumptions about the sources  $\mathbf{v}$  and the volume conductor model  $\mathbf{H}$  are incorporated into the second and first terms of the regularization 1.1, respectively. Although these prior assumptions help to circumvent the ill-posedness of the problem, the uncertainties/errors caused by them influence the solution of 1.1.

### 1.1.1 Uncertainties in Prior Assumptions on Cardiac Properties

Different fixed prior assumptions on spatial and/or temporal properties of cardiac sources  $\mathbf{v}$  are employed to circumvent the ill-posedness of the cardiac inverse problem. The most commonly used prior assumptions (i.e., prior models) on the source properties include fixed spatial and/or temporal smoothness assumptions ( $L_2$ -norm model) [6, 12–14], spatial sparsity assumptions ( $L_1$ -norm model) [15–18], and with or without physiological models of cardiac electrical activity [19, 20].

However, a fixed prior model does not necessarily reflect complex spatiotemporally changing properties of cardiac sources at different conditions. Cardiac sources undergo a complex spatiotemporal process in each cardiac cycle. Initially, cardiac sources are only active in a few sparsely distributed focal points. They then form an excitation wavefront during the depolarization phase that resembles a sharp edge, separating excited myocardium cells from resting cells. This is followed by a repolarization wavefront that is more extended and smooth compared to the excitation wavefront. Therefore, a sparsity or smoothness-constrained model is intuitively accurate for compact or extended distributions of cardiac sources, respectively. Furthermore, in a pathologic heart with increased heterogeneity in tissue property, the sparsity or smoothness of cardiac sources are hard to predict *a priori*. As a result, using a fixed model for constraining the complex spatiotemporally changing properties of cardiac electrical sources introduces uncertainties to the EP imaging solution, when there is a mismatch between the fixed prior model and true source distribution. The impact of these uncertainties on the EP imaging solution has never been studied before.

### 1.1.2 Uncertainties in Prior Assumptions on the Volume Conductor

Different prior assumptions about the volume conductor model  $\mathbf{H}$  are incorporated to reduce the ill-posedness of the problem and its computational complexity, or to avoid the non-unique solution space. The most commonly used prior assumptions on the volume conductor model include the assumptions on the anatomical models of heart and torso [21, 22] and conductivity parameters of the volume conductor [23].

However, these prior assumptions involve uncertainties/errors, when they represent an approximation (rather than the exact) of the physical domain. While previous studies have addressed the impact of uncertainties in conductivity parameters [24] and certain *global* anatomical parameters (heart size, position and orientation with respect to body-surface electrodes) of the volume conductor model [21, 22, 25] on the EP imaging solution, the importance of uncertainties in highly-detailed anatomical modeling has never been studied before. These inevitable anatomical modeling uncertainties stem from a variety of factors such as image quality, segmentation expertise, segmentation methods, and/or registration techniques, which lead to unresolved uncertainties in the outcome of EP imaging systems. At the same time, detailed anatomical modeling puts high demands on the quality of tomographic images and image-analysis process, the complexity of which reduces the cost-effectiveness of the otherwise promising technique of EP imaging in clinical practice.

These uncertainties originating from prior assumptions on the source properties as well as anatomical modeling uncertainties may compromise the accuracy of the EP imaging solution, raising questions on the robustness of cardiac EP imaging systems for future

clinical practice. As described earlier, these uncertainties have never been studied and addressed before.

## 1.2 Dissertation Contribution

In this dissertation, our goal is to quantify and reduce the effect of the uncertainties caused by prior assumptions about the cardiac source properties and anatomical modeling on the solution of cardiac EP imaging.

### 1.2.1 Addressing Uncertainties in Prior Assumptions on Source Properties

We study the impact of prior assumptions about the source properties on the solution of cardiac EP imaging, followed by a novel EP imaging technique to reduce that impact.

- We first propose a novel yet simple  $L_p$ -norm regularization method for cardiac source imaging to study the impact of fixed prior models (such as  $L_1$ - and  $L_2$ -norm models) on accurate reconstruction of spatiotemporally complex cardiac sources at different conditions. This study indicates limitations of fixed prior models for constraining complex cardiac source structures, raising a need for an adaptive prior model that can automatically reflect spatiotemporal changes in the cardiac sources.
- To overcome the limitations of fixed prior models, we then propose a multiple model Bayesian approach to cardiac EP imaging that employs a continuous combination of prior models, each reflecting a specific spatial property for volumetric

cardiac sources. The 3D source estimation is then obtained as an weighted combination of solutions across all models. Therefore, automatic adjustment of weights changes the contribution of prior models to the final solution at different conditions, reducing the chance of mismatch between prior models and true source distribution.

This physiologically-meaningful multi-model constraint also enables us to reconstruct shape features of the cardiac source structure such as activation front and infarct border, characterization of which is of great therapeutic importance.

In addition, implementing our multiple-model approach in Bayesian framework not only enables automatic estimation of unknown system parameters in addition to source distribution, it also provides complete distribution of cardiac sources that gives more insight through statistical characteristics of the solution.

### 1.2.2 Addressing Uncertainties of Anatomical Modeling

In addition, we study the impact of anatomical modeling uncertainties on the solution of cardiac EP imaging, followed by a clinically feasible anatomical modeling technique.

- We first design a systematic statistical framework to analyze the sensitivity of EP imaging to the anatomical modeling variations. This framework utilizes statistical shape modeling as well as unscented transform to quantify/model otherwise ambiguous uncertainties/variations in anatomical shape details and determine their relation to the EP imaging output. This study reports robustness of cardiac EP imaging to the uncertainties inherent in anatomical modeling, indicating the possibility that high-level complexity in personalized anatomical models might not be necessary for reliable EP imaging. As a result, the process of anatomical modeling

in current EP imaging systems may be simplified for improved clinical feasibility in future practice.

- To improve anatomical modeling experience for clinical practice, we then propose a simplified anatomical model for the heart, based on analytic descriptions of regular 3D geometrical shapes, that only incorporates subject-specific anatomical parameters (heart size, position and orientation with respect to body-surface electrodes), while discarding local shape details. Exploiting less resources and processing for successful EP imaging, this simplified model helps moving EP imaging closer to clinical application.

### 1.3 Dissertation Organization

This dissertation is organized as follows: Chapter 2 reviews the background of cardiac electrophysiology and related EP imaging techniques. Chapter 3 provides the details of our analysis about the impact of fixed prior models on the solution of EP imaging. Details of our proposed multiple-model approach for volumetric EP imaging is demonstrated in chapter 4. Chapter 5 illustrates our proposed systematic statistical approach for quantifying anatomical modeling uncertainties and assessing their impact on the EP imaging solution. Chapter 6 provides detailed description of cardiac simplified anatomical model. We conclude in Chapter 7 by providing a summary of the strengths and limitations of this work, as well as discussions on the future research directions.

## Chapter 2

# Background and Related Works

### 2.1 Cardiac Electrophysiology

The heart is a cone-shaped muscular organ located inside the ribcage between the right and left lungs and beneath the sternum. The anatomical structure of the heart is divided into two halves (right and left), each of which includes two chambers (atrium and ventricle). Contraction of the chambers pumps the blood throughout the body. However, heart contraction is originally stimulated by its electrical activity, which stems from the *sinoatrial (SA) node*. *SA node*, located at the right atrium, generates an electrical impulse that spreads to the *atrioventricular (AV) node*, located between the atria and the ventricles. After a delay at the *AV node*, the electrical impulse propagates to the bundle of *His*, the bundle branches and *Purkinje* fibers, causing contraction of the ventricles. The electrical conduction system of the heart is shown in Fig. 2.1.

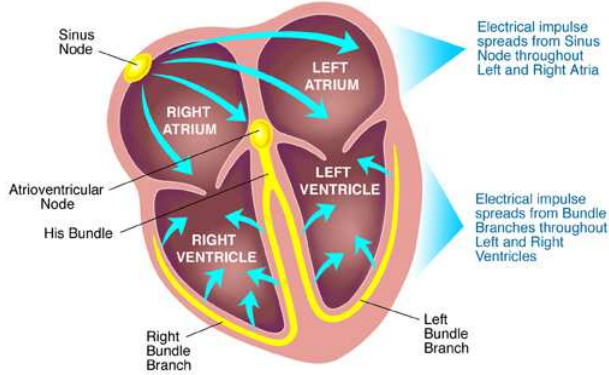


FIGURE 2.1: Cardiac electrical conduction system [1].

## 2.2 Imaging Cardiac Electrophysiology

Cardiac electrophysiology (EP), in the current clinical practice, is imaged using non-invasive and/or invasive methods. The most common non-invasive EP imaging method is standard 12-lead electrocardiography (ECG) that provides body-surface potential at 9 locations over time. An invasive counterpart of ECG is cardiac mapping that is often used to examine the electrical pattern of the heart by point-to-point catheter mapping on the heart surfaces. These techniques are briefly explained in the following sections.

### 2.2.1 Electrocardiography

Electrocardiography (ECG) is used to acquire body-surface potential dynamics in order to non-invasively understand the cardiac conduction system. It translates the electrical impulse generated by the polarization and depolarization of cardiac tissue into a waveform. The standard 12-lead ECG includes three limb leads that are placed on the left arm, right arm and left leg. In addition to the limb leads, it uses six precordial leads on the anterior thorax, as shown in Fig. 2.2.

The schematic of normal ECG tracing is shown in Fig. 2.3. It consists of the following major segments: *P wave*, *PR segment*, *QRS complex*, *ST segment*, and *T wave*. *P wave*

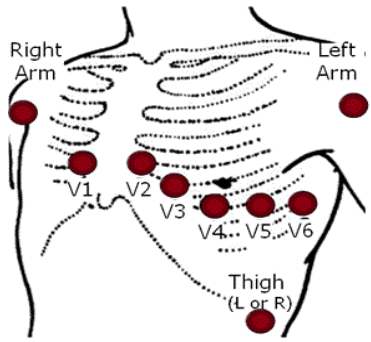


FIGURE 2.2: Standard 12-lead ECG [2].

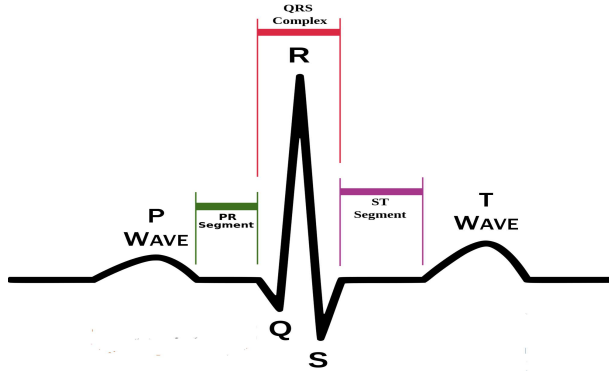


FIGURE 2.3: Schematic representation of normal ECG [3].

corresponds to the atrial depolarization stage. *PR segment* represents the activation propagation through *AV node* and *Purkinje* fibers. The *QRS complex* represents depolarization of ventricular myocardium. *ST segment* corresponds to the period during which the ventricles are depolarized. *T wave* represents repolarization of the ventricles.

Despite simplicity of ECG acquisition, it is obtained at very low spatial resolution (9 lead recordings) on the body surface far from the original electrical source inside the heart. Thus, it lacks the regional detailed information about cardiac electrical propagation required for interventional therapies such as localization and ablation of the arrhythmogenic substrate.

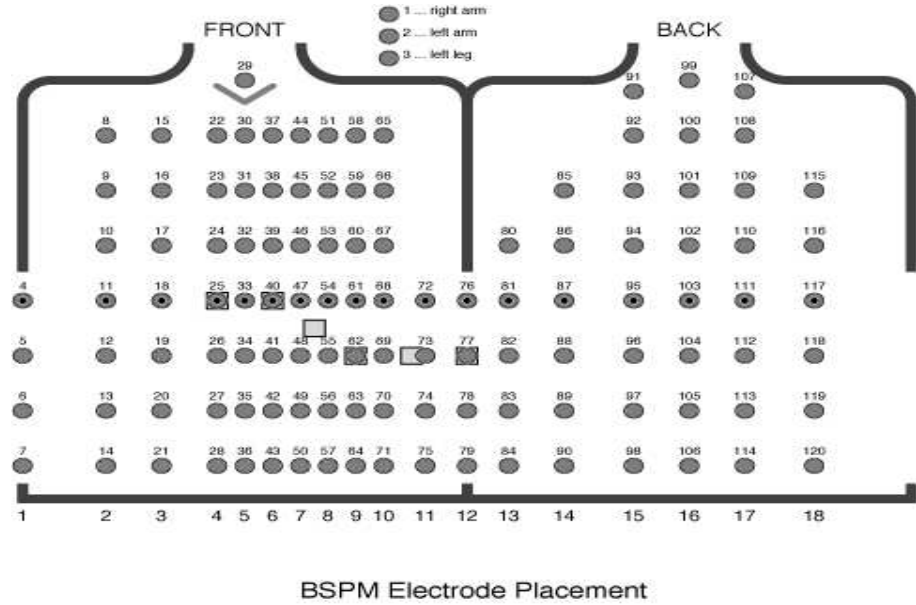


FIGURE 2.4: Electrode positioning on the body-surface in a 120-lead Dalhousie BSPM standard [4].

### 2.2.2 Body-Surface Potential Mapping

A complete version of ECG system is body-surface potential mapping (BSPM) that records potential dynamics at more locations (using 30 to 200+ electrodes) on front and back of the torso. An example BSPM layout (Dalhousie standard), consisting of 120 electrodes, is shown in Fig. 2.4.

Covering front and back of the torso, BSPM provides additional information compared to 12-lead ECG system that helps clinician to follow the source activity inside the heart (Fig. 2.5). It also better reflects local variations in heart activity.

Unfortunately, currently there is no recognized standard for electrode positioning or recording system due to the difficulty in acquisition and interpretation of massive amounts of BSP data. However, computational cardiac EP imaging methods, as will be discussed later in this chapter, rely on it as a main input for inverse estimation.

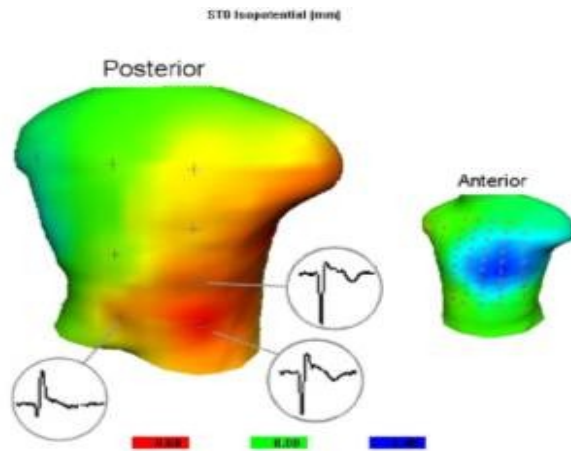


FIGURE 2.5: An example of a BSPM in both anterior and posterior view [5].

### 2.2.3 Cardiac Mapping

When regional details of cardiac electrical activity are needed for interventional therapies, invasive electroanatomic mapping is employed in the current clinical setting to directly record the voltages at different locations of the heart by point-to-point catheter mapping on heart surfaces. In this procedure, cardiac electrophysiologists place one or more catheters within the patient's heart, pace the heart to induce electrical dysfunctions, and record electrical signals produced in the cavity of the heart.

However, this laborious point-to-point mapping procedure has fundamental limitations. First, it is an invasive and time-consuming procedure that places the patient at the risk of fatal arrhythmia and exposure to fluoroscopy radiation [7–9]. Second, it requires a point-by-point mapping procedure that does not allow simultaneous beat-to-beat mapping. As a result, the acquired information requires skillful aggregation and annotation of the clinicians. Third, it provides spatially low resolution surface-based information, which is a poor surface surrogate for the transmural electrical activity across the depth of the myocardium.

## 2.3 Computational Approaches for Imaging Cardiac Electrophysiology

In response to the limitations of the current clinical techniques, computational electrophysiological imaging is developed, which aims to mathematically reconstruct subject-specific cardiac electrical dynamics from body-surface recordings and vice versa. It consists of cardiac forward modeling and inverse problem estimation, both aim to establish the relationship between cardiac electrical sources and body-surface voltage measurements. This line of research has the potential to eliminate the limitations of catheter mapping and improve the current clinical practice of imaging cardiac electrophysiology in terms of accuracy and involved risks.

### 2.3.1 Cardiac Forward Modeling

Cardiac forward modeling seeks to determine the body-surface potential resulting from the activity of cardiac electrical sources. The quasi-static electromagnetism [11] explains the relation between the potential distribution within the torso volume and the cardiac electrical sources as:

$$\nabla \cdot ((\mathbf{D}_{int} + \mathbf{D}_{ext}) \nabla \phi_e(\mathbf{r})) = \nabla \cdot (-\mathbf{D}_{int} \nabla u(\mathbf{r})), \forall \mathbf{r} \in \Omega_h \quad (2.1)$$

$$\nabla \cdot (\mathbf{D}_i \nabla \phi_i(r)) = 0, \forall \mathbf{r} \in \Omega_i, \cup \Omega_i = \Omega_{t/h} \quad (2.2)$$

On a bidomain heart model, equation 2.1 describes how the extracellular potential  $\phi_e$  within the heart volume  $\Omega_h$  originates from the spatial gradient of action potential

$u$ .  $\mathbf{r}$  stands for the spatial coordinate,  $\mathbf{D}_{int}$  and  $\mathbf{D}_{ext}$  are the effective intracellular and extracellular conductivity tensors, and their summation  $\mathbf{D}_k = \mathbf{D}_{int} + \mathbf{D}_{ext}$  is bulk conductivity tensor.

On the monodomain torso model, equation 2.2 describes how the potential  $\phi_i$  distributes within the volume conductor  $\Omega_i$  external to the heart with conductivity tensor  $\mathbf{D}_i$ , assuming that no other active electrical source exists within the torso.

Within the myocardium 2.1, the anisotropic ratio of  $\mathbf{D}_k$  is a magnitude smaller than that of  $\mathbf{D}_{int}$  [26, 27]. Therefore, we only retain the intracellular anisotropy and assume isotropic bulk and torso conductivity, which converts  $\mathbf{D}_k$  and  $\mathbf{D}_i$  to scalars  $\sigma_{blk}$  and  $\sigma_i$ , respectively. This is similar to an oblique dipole layer model, where the anisotropy of primary current is considered whereas that of passive/secondary current is neglected [27]. Intracellular conductivity tensor  $\mathbf{D}_{int}$  is obtained by mapping a 3D experimentally-derived mathematical fiber model to the personalized ventricular geometry of the subject [28]. Its conductivity is assumed to be  $0.24\text{ Sm}^{-1}$  in longitudinal direction and  $0.024\text{ Sm}^{-1}$  in transversal direction [29]. Isotropic bulk conductivity  $\sigma_{blk}$  is calculated as an intermediate value between longitudinal and transversal conductivities ( $0.48\text{ Sm}^{-1}$  and  $0.12\text{ Sm}^{-1}$ , respectively) [29]. Torso is assumed to be homogeneous with conductivity value  $\sigma_t$  equal to  $0.2\text{ Sm}^{-1}$  [29]. Based on these assumptions, the forward relationship between cardiac action potential  $u$  and body-surface voltage data  $\phi$  can be described in the following Poisson's equation 2.3 within the heart and Laplace's equation 2.4 external to the heart:

$$\sigma_{blk} \nabla^2 \phi_e(\mathbf{r}) = \nabla \cdot (-\mathbf{D}_{int} \nabla u(\mathbf{r})), \forall \mathbf{r} \in \Omega_h \quad (2.3)$$

$$\sigma_t \nabla^2 \phi(\mathbf{r}) = 0, \forall \mathbf{r} \in \Omega_{t/h} \quad (2.4)$$

To preserve the continuity of potentials and currents on the interface, a boundary condition on the heart surface  $\Gamma_h$  is defined as:

$$\begin{aligned} \phi_e(\mathbf{r}) &= \phi(\mathbf{r}) \\ \forall \mathbf{r} \in \Gamma_h \end{aligned} \quad (2.5)$$

$$\sigma_{blk} \frac{\partial \phi_e(\mathbf{r})}{\partial n} + \mathbf{D}_{int} \frac{\partial u(\mathbf{r})}{\partial n} = \sigma_t \frac{\partial \phi(\mathbf{r})}{\partial n}$$

Similarly a boundary condition is defined on the torso surface that assumes no current (flux) leaves the torso surface  $\Gamma_t$ :

$$\frac{\partial \phi(\mathbf{r})}{\partial n} = 0 \quad \forall \mathbf{r} \in \Gamma_t \quad (2.6)$$

where  $n$  stands for the outward normal of a surface.

Equations (2.3-2.6) can be numerically solved on a subject heart-torso model to obtain a linear relationship:  $\Phi = \mathbf{Hv}$  [30], between body-surface measurements  $\Phi$  and cardiac source  $\mathbf{v}$ .

### 2.3.2 Cardiac Inverse Electrophysiological Imaging

Cardiac inverse EP imaging, also known as the inverse problem of electrocardiography (IECG), aims to mathematically reconstruct subject-specific cardiac electrical dynamics

from non-invasive body-surface measurements on anatomical regions of heart and torso. Existing EP imaging techniques can be generally divided into two categories, according to how the above bidomain equations are solved in the forward modeling. In earlier approaches, the forward model is constructed on the domain external to the heart surface by solving the Laplace equation (2.4,2.6). In these approaches, the equivalent source model takes the form of epicardium and/or endocardium potentials [31–33] or activation time on the ventricular surface [34–36]. By formulating the source model on the heart surface, these approaches avoid the non-unique solutions induced by the underlying biophysics. Recent efforts start to examine the forward model that includes the domain of 3D myocardium, solving both the Poisson’s equation (2.3,2.5) and the Laplace’s equation (2.4,2.6). The source model in these approaches represent the real physiological sources in the heart, in the form of 3D transmural action potential [19, 20, 37–39], spatial gradient of 3D transmural action potential [40], or current density / activation wavefront [41] throughout the myocardial wall. Because of the 3D source model beneath the heart surface, this type of approaches faces additional challenges of non-unique solutions induced by the underlying biophysics of the problem.

### 2.3.2.1 Surface-based EP Imaging

Mainstream EP imaging approaches reconstruct EP characteristic on the heart surfaces. In these methods, cardiac sources are characterized by their reflection on the heart surface (epicardium and/or endocardium) as potential distribution. Lacking any physiologically-meaningful priors, these methods apply regularization with a fixed prior model to overcome the ill-posedness of this inverse problem, such as Tikhonov regularization (zero-order, first-order, and second-order) and truncated singular value decomposition (SVD) regularization [31]. Other efforts incorporate additional physiological

constraints to the solutions including spatial and/or temporal smoothness of the potential distribution [6, 42]. Recently,  $L_1$ -norm based sparsity models have also been used to enforce low-dimensional features of the solutions in space [15–17]. Although, these methods provide the electrical dynamics of the heart from closer distance to the electrical sources inside the heart with higher resolution compared to body-surface ECG, extracting electrophysiological characteristics of the heart such as activation and repolarization time still is not straight forward. Other EP imaging methods directly recover the activation front on the heart surfaces [34, 35]. The advantage of these methods over the potential-based methods is the reduction in the number of unknowns that leads to a better-posed problem. In addition, activation-based methods show better stability and accuracy in the presence of measurement and geometry errors. However, the problem of activation front imaging is non-linear and non-convex, requiring a physiologically accurate models.

Although, these surface-based approaches provide non-invasive, simultaneous EP data, they provide limited information about the 3-dimensional potential dynamics beneath the heart surface that is of more direct medical interest. Furthermore, fixed prior models used in these surface-based approaches do not effectively reflect spatiotemporal changes of cardiac electrical sources, leading to errors/uncertainties in the final solution.

### 2.3.2.2 Volumetric EP Imaging

In the past decade, transmural (volumetric) EP imaging has been emerged that considers transmural source models in forms of transmural action potential [19, 20, 37–39], spatial gradient of 3D transmural action potential [40], or current density / activation wavefront [41]. In the reconstruction of current density or activation wavefront, different orders of smoothness constraints have been imposed on the spatial or temporal

properties of the solution, through methods such as Laplacian weighted minimum norm [37], or lead-field normalized weighted minimum norm (LFN-WMN) in combination with truncated-SVD [41]. In the reconstruction of transmural action potential, physiological constraints are often used [19, 20, 39]. For instance, Ohyu *et al.* proposed a maximum a posteriori (MAP) estimation of transmural action potential (AP) by modeling AP as a simplified template step function [39]. Another example is the method proposed by He *et al.* that presents a parametrized cellular automaton heart model, where deterministic regularization is used to optimize the model parameters [20]. However, deterministic optimization presented in [20] cannot efficiently handle noise and often is dependent on the initial condition. Wang *et al.* also proposed another transmural EP imaging approach that guides MAP estimation of the transmembrane potential distribution using a 3D whole-ventricle electrical excitation model [19]. In contrast to the deterministic method [20], the statistical model presented in [19] takes into account the model and data uncertainties.

Although these methods provide volumetric imaging of cardiac electrical dynamics, the fixed prior model used in these methods [19, 20] conflicts with the complex structural properties of the cardiac electrical sources and cannot adaptively reflect the change in the source structure. This conflict impacts the solution of EP imaging methods by introducing errors/uncertainties in the solution.

## **Chapter 3**

# **Impact of Prior Assumptions**

## **About Source Properties on**

## **Cardiac Electrophysiological**

## **Imaging**

### **3.1 Background**

Cardiac electrophysiological (EP) imaging utilizes computational techniques to non-invasively estimate cardiac bioelectrical source activity from body-surface ECG measurements on anatomical models of heart and torso. In general, EP imaging involves solving a severely ill-posed inverse problem which lacks a unique transmural solution in its most unconstrained form. This ill-posedness is caused by the underlying biophysics of the problem: different configurations of 3D sources may produce the same surface measurements [11]. In addition, the attenuation and smoothing effect of the

medium between cardiac sources and body-surface measurements (torso volume conductor) increase the ill-posedness of this problem. Furthermore, the limited number of surface measurements compared to the large degree of unknown sources adds to the ill-posedness of this problem. Proper assumptions of the solutions must be made in order to overcome the ill-posedness of the problem and obtain a unique solution.

Over the past three decades, many approaches have been developed for non-invasive cardiac EP imaging with the focus on finding proper prior assumptions/models for the source distribution. First, different equivalent source models are used as an implicit constraint on the solution. These models can be in general classified into two groups: 1) surface-based source models in forms of epicardial potential [31–33], or activation time of the ventricular surface [34–36], and 2) volumetric source models in forms of intramural action potential [19, 20, 37–39, 43], or current density/activation front throughout the myocardial wall [41]. The surface-based source models implicitly overcome the lack of unique solutions by constraining the solution on the heart surface, while the transmural source models rely on further assumptions to overcome this physical ill-posedness. Second, assumptions on different properties of the equivalent source models are used to further regularize the ill-posed inverse problem. For example, spatial and/or temporal smoothness of the source models have been commonly used and enforced through different numerical techniques such as Tikhonov regularization (zero-order, first-order, and second-order) [14], truncated SVD [12, 13], and Kalman filter framework [6]. Recently,  $L_1$ -norm based sparsity models have also been used to enforce low-dimensional features of the solutions in space [15–18]. In addition, physiological prior knowledge generated from computational models of 3D electrical excitation has also been adopted to constrain transmural EP imaging [19, 20].

While these predefined models are beneficial in circumventing the ill-posedness of the

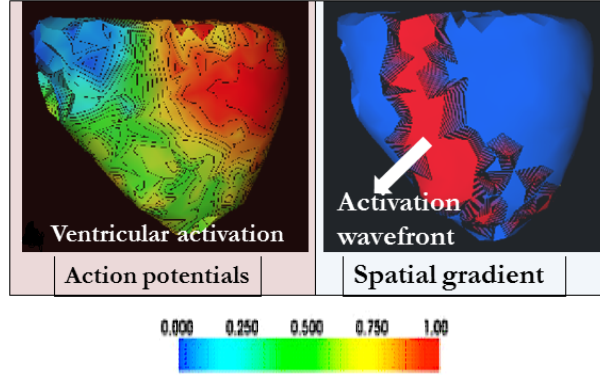


FIGURE 3.1: Illustration of action potential and its spatial gradient during excitation phase of cardiac cycle in a healthy heart.

problem, they also rely on fixed assumptions that may not generalize to the property of EP excitation at different conditions. For example, they may enforce the source distribution to follow a pre-assumed spatial structure that does not necessarily reflect the spatiotemporal evolution of cardiac sources. Cardiac sources undergo a complex spatiotemporal process in each cardiac cycle. Initially, cardiac sources are only active in a few sparsely distributed focal points. They then form an excitation wavefront during the depolarization phase that resembles a sharp edge separating excited myocardium cells from resting cells (Fig. 3.1). This is followed by a repolarization wavefront that is more extended and smooth compared to the excitation wavefront. Therefore, a sparsity model is intuitively ideal when the sources exhibit compact spatial properties, *e.g.*, at the beginning of the excitation phase, while a smoothness-constrained model better suits extended distributions of cardiac sources, *e.g.*, repolarization phase. Furthermore, in a pathologic heart with increased heterogeneity in tissue property, the sparsity or smoothness of sources are hard to predict *a priori*. Overall, a fixed prior model may have its limitations when used for constraining the complex spatiotemporal property of cardiac electrical excitation.

Based on these observations, we design a set of experiments to specifically study the impact of fixed prior assumptions/models (such as  $L_1$ - and  $L_2$ -norm models) about the

cardiac source properties on the solution of EP imaging at different conditions. Toward this goal, we first propose a novel yet simple  $Lp$ -norm regularization method, where  $p$  value is selected empirically, to reconstruct volumetric cardiac sources. We then take one step further to incorporate temporal information into the  $Lp$ -norm regularization to promote the temporal consistency and stability of the reconstruction in the presence of measurement noise. To do so, we assume that cardiac sources share the same temporal basis functions as the surface measurements. Decomposing the surface measurement into spatial and temporal components using singular value decomposition (SVD), we apply  $Lp$ -norm regularization to the remaining spatial component. In both approaches, changing the  $p$  value between 1 and 2, we assess the impact of different but fixed spatial prior models (including  $L1$ - and  $L2$ -norm models) on the accuracy of source reconstruction.

In two sets of phantom and real-data experiments, we investigate the impact of fixed prior models on cardiac source estimation and demonstrate the necessity of an adaptive (rather than fixed) prior model for accurate reconstruction of different source structures and sizes.

### 3.2 $Lp$ -norm Regularization

To assess the impact of fixed prior models on the accuracy of the source reconstruction, we propose a  $Lp$ -norm regularization approach for 3D cardiac source reconstruction. This regularization can be formulated as:

$$\begin{aligned} \min_{\mathbf{v}} & \quad ||\Phi - \mathbf{Hv}||_2^2 + \lambda ||\mathbf{v}||_p \\ & \quad ||\mathbf{v}||_p = (\sum_{i=1}^n [v_i]^p)^{1/p}, \quad 1 < p < 2 \end{aligned} \tag{3.1}$$

where  $\Phi$  is body-surface measurements at one time instant,  $\mathbf{v}$  is cardiac sources (spatial gradient of action potential),  $n$  is the dimension of  $\mathbf{v}$ , *i.e.*, the number of discrete nodes used to represent the ventricular myocardium. Changing the  $p$  value in regularization 3.1 enables us to assess the impact of different fixed prior models on the accuracy of source reconstruction.

### 3.3 $Lp$ -SVD Regularization

We then take one step further to incorporate temporal information to the  $Lp$ -norm regularization 3.1 in order to improve temporal consistency and robustness to noise. To achieve this goal, we follow the assumptions of the isotropy model presented in [44] and assume that cardiac sources share the same temporal basis functions as ECG measurements. These temporal basis functions can be obtained by different transformations, and in this study we consider taking the singular value decomposition of ECG measurements:

$\Phi = \mathbf{U}\mathbf{S}\mathbf{T}'$ , where  $\mathbf{T} = [\mathbf{t}_1, \mathbf{t}_2, \dots, \mathbf{t}_k]$  defines the orthonormal temporal basis functions. Projecting both ECG measurements and cardiac sources onto the basis functions  $\mathbf{T}$ , new variables  $\tilde{\Phi} = \Phi\mathbf{T}$  and  $\tilde{\mathbf{v}} = \mathbf{v}\mathbf{T}$  are obtained to represent the corresponding projection coefficients. We then apply  $Lp$ -norm regularization to reconstruct new variable  $\tilde{\mathbf{v}}$  from  $\tilde{\Phi}$ . In this way, the  $Lp$  regularization problem can be formulated only on the spatial domain as:

$$\begin{aligned} \min_{\tilde{\mathbf{v}}} & \quad \|\tilde{\Phi} - \mathbf{H}\tilde{\mathbf{v}}\|_2^2 + \lambda\|\tilde{\mathbf{v}}\|_p \\ & \quad \|\tilde{\mathbf{v}}\|_p = (\sum_{i=1}^n [\tilde{v}_i]^p)^{1/p}, \quad 1 < p < 2 \end{aligned} \tag{3.2}$$

where  $n$  is the dimension of  $\tilde{\mathbf{v}}$ , *i.e.*, the number of discrete mesh-free nodes used to represent the ventricular myocardium. Solving the regularization problem 3.2, the optimal

coefficient  $\tilde{\mathbf{v}}$  would be obtained. The cardiac sources  $\mathbf{v}$  are then calculated as linear combinations of the temporal basis functions:  $\mathbf{v} = \tilde{\mathbf{v}}\mathbf{T}$ .

Imposing  $Lp$ -norm prior model with varying  $p$  value on the spatial component of the sources promotes different spatial structures as often observed in the heart. Therefore, changing  $p$  value between 1 and 2,  $Lp$ -norm spatial prior model provides a flexible tool to analyze the impact of fixed prior models on localizing sources with different sizes. Furthermore, solving the regularization 3.2 in the transformed domain spanned by the temporal basis of the measurement  $\Phi$  imposes temporal consistency of the reconstructed sources. Solving the problem in the singular vector domain 3.2 has an additional advantage of reducing the size of the problem and increasing the robustness to noise. In typical situations, where the number of time instances for  $\Phi$  is in the order of hundreds, the leading singular vectors of  $\Phi$  are less than 10 (accounting for  $\geq 95\%$  of the data variation). The leading singular vectors are obtained by taking the  $c$  highest singular values that provide 95% of the data variation. Thus, solving 3.2 only for the first  $c$  leading singular vectors results in  $\geq 90\%$  reduction of the problem size as well as an increased robustness to noise.

Adopting second-order cone programming (SOCP), we convert regularization 3.2 to SOCP problem and solve it using the CVX toolkit [45].

### 3.4 Experiments and Results

We conduct two sets of synthetic and real-data experiments using our proposed  $Lp$ -norm and  $Lp$ -SVD regularization methods to investigate the impact of imposing fixed prior models on spatial properties of cardiac sources on the accuracy of source reconstruction.

### 3.4.1 Synthetic Experiments

In the synthetic experiments, we consider a heart-torso model derived from a human subject. The torso surface is represented by triangulated elements with 370 vertices. The ventricular myocardium is represented by evenly-distributed points with 7 mm resolution and confined by the ventricular surface.

The accuracy of 3D source estimation is evaluated using the *source overlap (SO)* defined as the intersection divided by the union between the estimated and the true region of cardiac sources:

$$SO = \frac{\text{simulated sources} \cap \text{estimated sources}}{\text{simulated sources} \cup \text{estimated sources}} \quad (3.3)$$

#### 3.4.1.1 Imaging Sources with Various Sizes Using $L_p$ -norm Regularization

In the first set of experiments, we investigate the impact of fixed prior models using  $L_p$ -norm regularization without temporal information on localizing cardiac source regions with different sizes. In total, 44 settings are studied, considering a region of active cardiac sources sized from 1% to 45% of the left ventricle. These source regions are placed at different locations inside the ventricular myocardium. The nodes lying within the region of active sources are assigned with values 1, while the rest of the ventricular nodes are set to be 0. For each setting, the corresponding ECG measurements are simulated on the 370 vertices on the body-surface, and are corrupted with white Gaussian noise (30 dB SNR) before being input to the  $L_p$ -norm method to reconstruct the region of active cardiac sources.

For every source setting,  $L_p$ -norm estimation (without temporal constraint) at single time instant is obtained using  $p \in \{1, 1.1, 1.3, 1.5, 1.7, 1.9, 2\}$ .

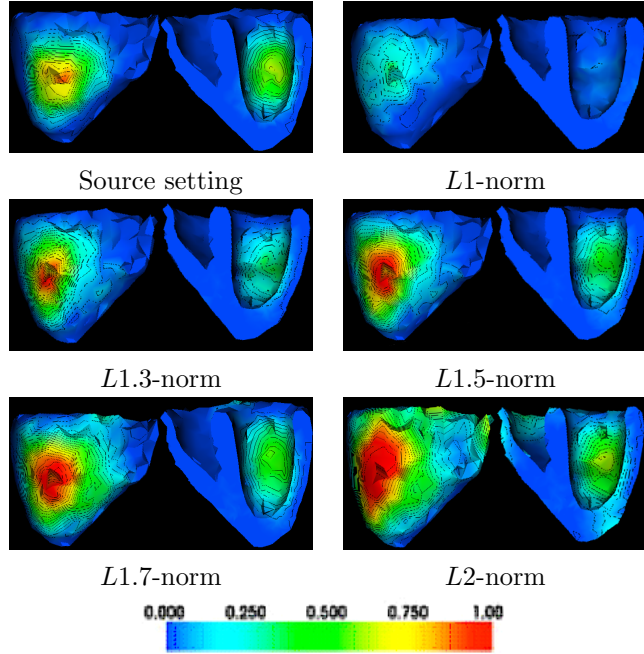


FIGURE 3.2: Source estimation using  $L_p$ -norm regularization for  $1 \leq p \leq 2$ . 58 active sources are located at left ventricle mid-anterior. Increasing the  $p$  value increases the source size such that  $L_1$ -norm obtains too scattered source distribution while  $L_2$ -norm provides overly-diffused solution. Cardiac source magnitudes are normalized to 1.

Fig 3.2 shows an example of source estimation using  $L_p$ -norm regularization for  $1 \leq p \leq 2$ , where the active region is located at mid-inferior of the left ventricle. The  $L_1$ -norm estimation of active sources results in a very sparse source reconstruction ( $SO = 0.05$ ) scattered in the true region of active sources, and nearly no active sources were detected close to the endocardium. Increasing the  $p$  value for the  $L_p$ -norm regularization, the detected source region size increases. At  $p = 1.3$ , we obtain a more accurate estimation of source region ( $SO=0.38$ ), which is located very close to the true region of active sources. As  $p$  continues to increase, the estimated source region becomes more extended but still has a relatively compact center. There is a sudden change of pattern in the solution when  $p$  equals to 2, where the estimated source region ( $L_2$  solution) becomes very diffused ( $SO=0.22$ ). Another example is presented in Fig 3.3, where the active cardiac sources are located close to the right ventricle apex. Similar pattern can be observed in the source estimation by increasing the  $p$  value from 1 to 2, while the most

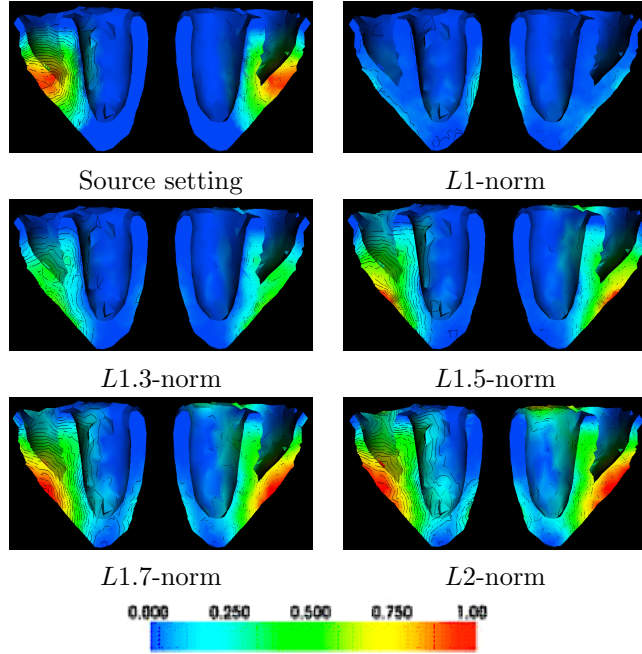


FIGURE 3.3: Source estimation using  $L_p$ -norm regularization for  $1 \leq p \leq 2$ . 127 active sources are located close to the right ventricle apex. Increasing the  $p$  value increases the source size such that  $L_1$ -norm obtains too scattered source distribution while  $L_2$ -norm provides overly-diffused solution. Cardiac magnitudes are normalized to 1.

accurate result is obtained at  $p = 1.7$ . These two examples demonstrate that different source sizes may require different prior models to be accurately estimated.

Fig 3.4 summarizes the mean SO (vertical-axis) between the true and estimated source region obtained using  $L_p$ -norm regularization, as  $p$  increases from 1 to 2 (horizontal axis 1) and as the size of active region increases (horizontal axis 2). As shown, focal small source regions are better estimated using  $L_1$ -norm model with low false-positives. However, the solution produced by  $L_1$ -norm regularization for medium and large source regions has a high under-estimation (low numerator in the calculation of the SO) and therefore a low value of SO. On the other extreme, the smeared solution of  $L_2$ -norm regularization is able to accurately detect large source regions. However,  $L_2$ -norm estimation tends to have a high over-estimation (high denominator in the calculation of the SO) for small regions leading to a low SO value. For source regions of medium sizes, the maximum SO is obtained, when  $1.5 \leq p \leq 1.6$ . These experiments show that

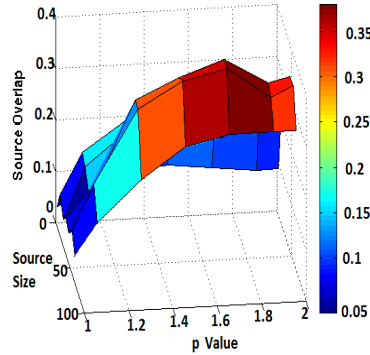


FIGURE 3.4: Source overlap (SO, vertical axis) obtained by  $L_p$ -norm ( $1 \leq p \leq 2$ , horizontal axis 1) for active sources with different sizes (1–100 active sources, horizontal axis 2).

accurate estimation of sources with different sizes requires different (rather than fixed) prior models.

### 3.4.1.2 Imaging Source Activity Along the Border of Computer-Simulated Infarct Regions

In the second set of experiments, we examine the impact of fixed prior models on estimating the source distribution along the infarct border during the ST-segment of an ECG cycle. During the ST-segment of an ECG cycle, there is no cardiac flow in a healthy heart. In an infarcted heart, in comparison, only the viable myocardium would exhibit coherent high plateau potential, while the necrotic tissue in the scar core will exhibit low plateau potential. These two regions will be separated by the infarct border with localized cardiac sources, as shown in Fig. 3.5. Realistic transmural action potential propagation is simulated by the Aliev-Panfilov [46] model. Next, the spatial gradient of action potential is calculated that represent our true sources. The corresponding ECG measurements on the body-surface are then simulated and the time frames corresponding to ST-segment are selected and corrupted with 20 dB noise as inputs to reconstruct the cardiac source distribution.

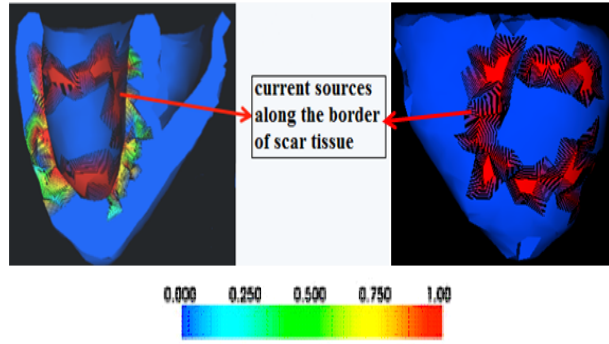


FIGURE 3.5: Illustration of action potential and its spatial gradient during the ST-segment of an ECG cycle in an infarcted heart.

### Impact of Time Incorporation on $L_p$ -norm Regularization

We first examine the importance of incorporating temporal information into the  $L_p$ -norm regularization in an infarcted heart during the ST-segment of an ECG cycle. Fig. 3.6 shows an example of cardiac source distribution along the infarct border that extends from basal to mid anterior and anterolateral LV (black contour) at 2 consecutive time samples during ST-segment. In total, 80 sources are located in the infarct border.  $L_1$  regularization produces a scattered solution of 24 ( $SO = 0.08$ ) and 20 active sources ( $SO = 0.06$ ), respectively.  $L_2$  regularization produces a diffused solution of 211 ( $SO = 0.26$ ) and 221 sources ( $SO = 0.24$ ). Neither of the methods is able to capture the structure of the cardiac sources along the infarct border. In comparison, the  $L_p$  regularization ( $p = 1.5$ ) detects 92 ( $SO = 0.35$ ) and 89 ( $SO = 0.31$ ) active sources that are closer to the ground truth but are inconsistent between the 2 time instances.  $L_p$ -SVD ( $p = 1.5$ ) detects 90 and 88 sources ( $SO = 0.39$  and  $0.38$ ) in regions consistent with the *true* infarct border. The importance of a proper fixed prior model (in this example, a  $L_p$  prior with  $p = 1.5$ ) is evident in reflecting the complex spatial shape of source distribution in this example. The incorporation of temporal constraints (the proposed SVD) is shown to further improve the temporal consistency of the solution especially in the presence of measurement noises.

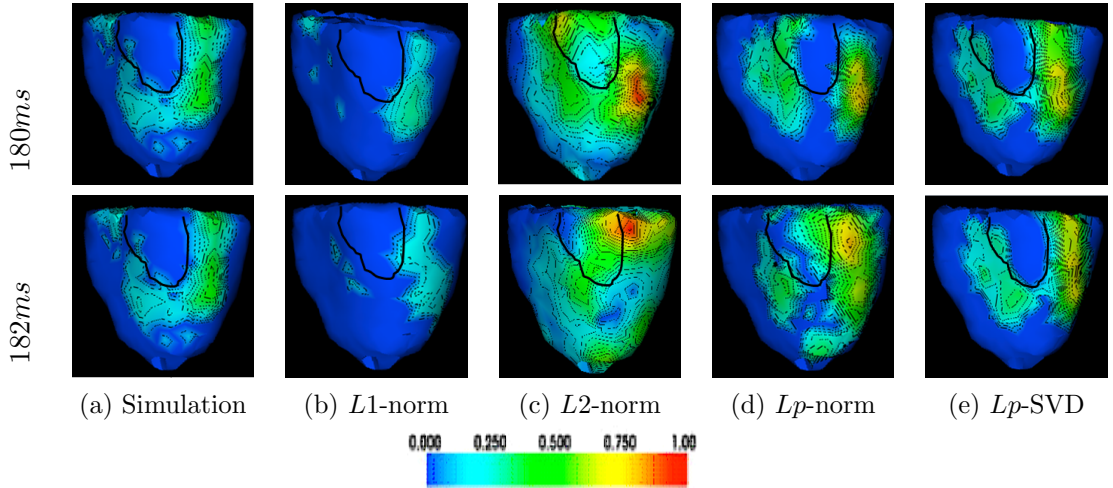


FIGURE 3.6: Estimation of cardiac sources localized along the infarct border using  $L_p$ -SVD regularization vs.  $L_p(p = 1.5)$ ,  $L_1$  and  $L_2$ -norm counterparts at two consecutive time samples during ST-segment of an ECG cycle.

### Imaging Sources Along the Infarct Border With Temporal Information

We consider 72 experiments with infarct regions located at different areas within the left ventricles (LV). The size of the infarct regions range from 1% to 45% of the LV. Fig. 3.7 shows an example with 69 sources distributed along the border of an infarct that extends from apex to apical inferior and lateral LV.  $L_1$  regularization produces a scattered solution with  $SO = 0.08$  while  $L_2$  diffused solution has  $SO = 0.26$ . In comparison,  $L_p$ -SVD ( $p = 1.5$ ) regularization provides a solution that is more consistent with the *true* infarct border with maximum  $SO = 0.41$ . This benefit of the  $L_p$ -SVD ( $p = 1.5$ ) is particularly evident when the infarct border is of medium size (20% ~ 30% of the LV), indicating the importance of different prior models for different source sizes.

Fig 3.8 presents SO mean and standard deviation between the true and estimated infarct border during the ST segment of an ECG cycle obtained using  $L_p$ -SVD, as  $p$  increases from 1 to 2 and as the size of infarct border increases. Summary of these experiments is also provided in Table 3.1. It can be seen that incorporating temporal information has increased the overall performance of source reconstruction using  $L_p$ -SVD regularization, compared to  $L_p$ -norm regularization (Fig. 3.4) without temporal information. Other

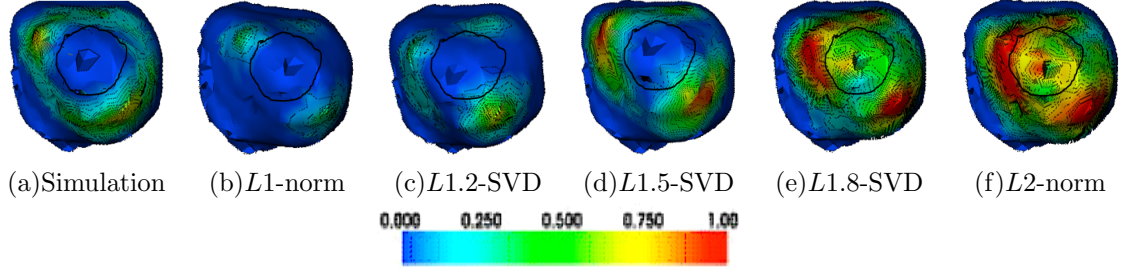


FIGURE 3.7: Estimation of cardiac sources along the infarct border using  $L_p$ -SVD,  $p \in \{1.2, 1.5, 1.8\}$ , vs.  $L1$  and  $L2$  counterparts during ST-segment of an ECG cycle.

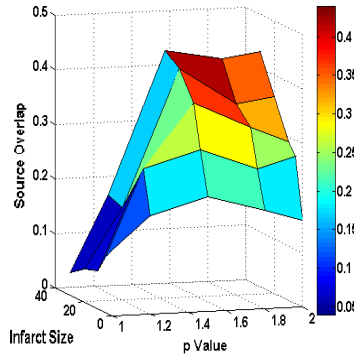


FIGURE 3.8: Comparison of segment overlap (SO) with respect to infarct border size.

TABLE 3.1: Comparison of segment overlap (SO) with respect to infarct border size.

Size/ Method	$0 \sim 5\%$ $n = 8$	$5\% \sim 10\%$ $n = 12$	$10\% \sim 20\%$ $n = 13$	$20\% \sim 30\%$ $n = 22$	$> 30\%$ $n = 17$
$L1$ -norm	$0.12 \pm 0.03$	$0.10 \pm 0.04$	$0.07 \pm 0.008$	$0.06 \pm 0.03$	$0.04 \pm 0.01$
$L1.2$ -SVD	$0.18 \pm 0.02$	$0.26 \pm 0.06$	$0.23 \pm 0.03$	$0.17 \pm 0.05$	$0.18 \pm 0.02$
$L1.5$ -SVD	$0.21 \pm 0.05$	$0.29 \pm 0.02$	$0.37 \pm 0.04$	$0.42 \pm 0.04$	$0.44 \pm 0.02$
$L1.8$ -SVD	$0.18 \pm 0.06$	$0.25 \pm 0.02$	$0.32 \pm 0.03$	$0.35 \pm 0.11$	$0.42 \pm 0.02$
$L2$ -norm	$0.16 \pm 0.07$	$0.27 \pm 0.02$	$0.29 \pm 0.02$	$0.36 \pm 0.10$	$0.43 \pm 0.02$

than that, both methods show similar performances at reconstructing sources with different sizes and structures. Overall, high performance of  $L2$ -norm model and  $L_p$ -SVD (with  $p=1.5$ ) for estimating large and medium size source regions, respectively, indicates that different source sizes/structures require different prior model for accurate source reconstruction.

### 3.4.2 Real-Data Experiments on Post-infarction Patients

Because of the important therapeutic value of the infarct border and what we observed in our initial synthetic experiments, we continue to conduct an initial real-data experiment on two post-infarction human subjects to assess the impact of fixed prior model in detecting cardiac sources along the infarct border during the ST-segment of an ECG cycle using the proposed  $L_p$ -norm prior model.

Experimental data were collected from two patients with prior myocardial infarction and made available to this study by *2007 PhysioNet / Computers in Cardiology Challenges* [47]. MRI scan of the patient has 8-mm inter-slice spacing and 1.33 mm/pixel in-plane resolution. Body-surface ECG maps were recorded by *Dalhousie University* standards [48] at 123 known anatomical sites and interpolated to 370 nodes of the *Dalhousie* torso model [4]; each ECG recording consists of a single averaged PQRST complex sampled at 2k Hz. Gold standards of the infarct were provided by cardiologists who examined the late Gadolinium enhanced (LGE) MR scans of the patients, and were provided in terms of the location and size of the infarct with regard to the 17-segment division of the LV according to AHA standards [49]. Specifically, according to the gold standard, in case 1 the infarct is centered at segment 8 and extends to segments 1, 2, 3, 9, 13, 14 and 15. The infarct center in case 3 is located at segment 10 and 11, between mid-inferior and mid-inferolateral of the LV of the subject (highlighted with black contour on Fig. 3.9) and extends to the neighboring segments (4, 5, 9, 12, 15, 16).

In both cases,  $L_1$ -norm (Fig. 3.9a) results in a very sparse solution scattered far from the infarct center during the ST-segment. Regions of cardiac sources provided by  $L_2$ -norm (Fig. 3.9b) are diffused and cover the infarct center. Neither of the methods is able to reveal any information on the location or the structure of the infarct border. The

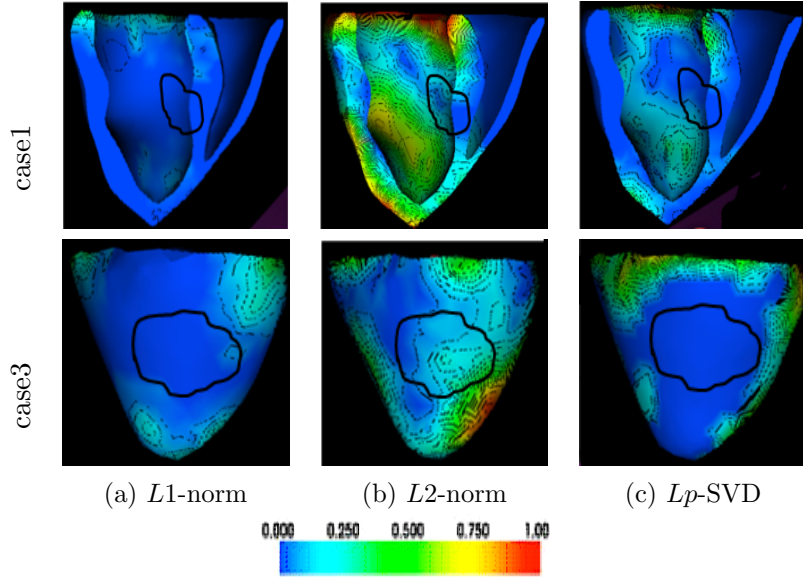


FIGURE 3.9: Estimation of cardiac sources along the infarct border using  $Lp$ -SVD ( $p = 1.5$ ) vs.  $L1$  and  $L2$ -norm regularizations for two post-infarction human subjects during the ST-segment of an ECG cycle.

proposed  $Lp$ -SVD solution ( $p = 1.5$ ) (Fig 3.9c) provides a more accurate estimation of the cardiac sources that distribute around the center of the infarct.

### 3.5 Conclusions

The inverse problem of volumetric cardiac source imaging is notoriously ill-posed without a unique solution. Different efforts to solve this ill-posed problem are mainly focused on imposing a fixed prior model on the spatial and/or temporal properties of cardiac cardiac sources. However, complex spatiotemporal property of cardiac cardiac sources determines that common fixed prior models ( $L1$ - and  $L2$ -norm models) are no longer proper because the underlying assumption (either too focal or too smooth) does not reflect the property of the source distribution at different conditions. We proposed a novel yet simple application of the  $Lp$ -norm regularization to analyze the impact of fixed prior models on cardiac source imaging with different structure/sizes. Furthermore, we

incorporated temporal information using the SVD technique to improve consistency over time and robustness to noise.

Our experimental results showed the limitations of fixed prior models ( $L1$ - and  $L2$ -norm models) in imaging sources with different sizes/structure. These limitations was more evident in imaging source activity along the infarct border, where spatial distribution of cardiac sources is not known *a priori*. Although in these experiments  $Lp$ -norm with  $p = 1.5$  obtained better results compared to  $L1$ - or  $L2$ -norm models, different conditions (source structures/sizes) may require different  $p$  values (different prior models) to obtain accurate solution.

In addition, this study showed the potential of  $Lp$ -norm prior model with varying  $p$  value as an adaptive prior model that can reflect spatiotemporal changes of cardiac sources.

Following the same assumptions as isotropy model [44], we used  $Lp$ -SVD regularization to primarily study the impact of spatial prior model on the solution of EP imaging. While  $Lp$ -SVD regularization provided temporal consistency and noise robustness for imaging sources during ST-segment of an ECG cycle, it may not provide a proper temporal basis function for the entire cardiac cycle, as detailed in this recent study [50]. Obtaining a proper temporal model is the focus of our future work, as discussed in Chapter 7.

In the next chapter, we address the limitation of fixed prior model by casting the  $Lp$ -norm regularization problem into a Bayesian framework and treat  $p$  as a hyperparameter to be estimated simultaneously from the data. Incorporating a continuous combination of prior models using  $Lp$ -norm model, our proposed approach overcomes the limitation of fixed prior model in reflecting different source structures.

## **Chapter 4**

# **Imaging Volumetric Cardiac**

## **Source Activity using a**

## **Hierarchical Multiple-Model**

## **Bayesian Approach**

### **4.1 Background**

Volumetric cardiac electrophysiological (EP) imaging requires solving a severely ill-posed problem. Existing efforts to overcome its ill-posedness mainly focus on imposing a fixed prior assumption/model on spatial and/or temporal properties of the current sources. However, fixed prior models may enforce the source distribution to follow a pre-assumed spatial structure that does not necessarily reflect the spatiotemporal evolution of cardiac current sources. In the previous chapter, we studied the impact of fixed prior models on the solution of EP imaging for different source structures/extents. The importance

of an adaptive prior model for optimal reconstruction of sources at different conditions were demonstrated through two sets of phantom and real-data experiments.

In this chapter, we present a multiple-model approach to reduce the model-data mismatch during volumetric cardiac EP imaging by allowing the prior model to adapt to available ECG measurements. A primary objective of this study is to investigate how the uncertainty in a prior model may affect EP imaging solutions and whether allowing the measurement data to pick a favorable set of models may reduce this effect. Therefore, we present a hierarchical Bayesian approach that employs a continuous combination of prior models, each reflecting a specific spatial property for transmural sources. Specifically, multiple models are incorporated as an  $Lp$ -norm prior for cardiac sources where the hierarchical structure allows the inclusion of  $p$  as an unknown hyperparameter with a prior uniform distribution: in this way, compared to a fixed model (*i.e.*, a pre-defined value for  $p$ ), this model consists of a continuous set of models, corresponding to different values of  $p$ , as defined by its density function. To examine how some models may be favored over others by different measurement data, the posterior distribution of cardiac sources and hyperparameter  $p$  is calculated using a Markov Chain Monte Carlo (MCMC) technique. The posterior distribution of  $p$  automatically determines the weight for each prior model to contribute to the posterior distribution of cardiac sources. In another word, the posterior distribution of  $p$  quantifies the reliance of 3D source estimation on different prior models, providing an understanding of how different combinations of prior models ( $p$  value ranging between 1 and 2) are preferred by different measurement data. In addition, the hierarchical Bayesian structure allows us to estimate additional parameters, including the variance of the measurement noise and the source prior, to be automatically inferred from the data. This alleviates the challenge of finding optimal parameters that often arises in the deterministic regularization [6, 16, 17].

Incorporating multiple prior models for imaging cardiac sources are conceptually similar to multiple-constraint method proposed by Brooks *et al.* that adopts a pre-defined finite set of models (constraints) with different order of  $L_2$ -norm in a deterministic regularization scheme for imaging equivalent source distribution on the heart surface [6]. The proposed multiple-model Bayesian approach can be considered as a generalization of Brooks *et al.* method to 1) include both  $L_1$ -norm and  $L_2$ -norm equivalent priors in the regularization, and 2) incorporate a continuous rather than discrete set of prior models through the use of hyperparameter  $p$  in a Bayesian framework that automates the estimation of the model combination. The proposed approach, in essence, can also be interpreted as the multiple model adaptive estimation (MMAE) that is commonly used for motion analysis and target tracking [51–53]. Like MMAE, a set of models are considered, where the weighted combination of all solutions determines the final solution. Nevertheless, there are two main differences that distinguish our work from MMAE. First, our approach considers a continuous distribution of models rather than a finite set of models. Therefore, it avoids the need to pre-define a finite number of models to sufficiently cover the model space. Second, MMAE is often used with minimum mean square error estimator such as Kalman filter to provide a point estimation of the output, while we are interested in a full Bayesian analysis of the output distribution.

The proposed multiple-model volumetric cardiac source imaging is performed on two sets of synthetic and real-data experiments, reconstructing 3D source distributions with different structures and sizes. To investigate the effect of fixing the prior model, in each experiment, solutions are also obtained by pre-defining the value of  $p$  in the  $L_p$ -norm to 1 and 2, respectively, in the proposed method. The results show that the posterior combination of models (the posterior distribution of  $p$ ) as determined by the ECG data differs substantially among different experimental settings. Furthermore, high variance

and complex distributions of  $p$  emerge when more complex pathological conditions are involved. This underscores the importance of 1) adapting prior models to different underlying source structures; and 2) utilizing a combination of models rather than one single model for a better match with complex source properties. These abilities, as demonstrated by the experiments, improve the robustness of imaging transmural electrical sources with different structures and sizes in comparison to fixed-model approaches.

While targeted at the application of noninvasive EP imaging in this chapter, the underlying concept of the presented work can be generalized to a broader variety of inverse problems that face the challenge of model-data mismatch.

## 4.2 Methodology

The inverse problem of cardiac EP imaging can be formulated as:

$$\mathbf{b} = \mathbf{Hv} + \mathbf{n}, \quad (4.1)$$

where  $\mathbf{b}$  represents the  $m \times 1$  body-surface measurement vector at one time instant,  $\mathbf{v}$  is  $n \times 1$  cardiac sources,  $\mathbf{H}$  denotes  $m \times n$  transfer matrix, and  $\mathbf{n}$  is  $m \times 1$  measurement noise.

### 4.2.1 Bayesian Inference

Bayesian inference refers to the general procedure of constructing a probability distribution for unknown parameters from given measurements, assuming both unknown parameters and known measurements to be random variables [54, 55].

Starting from the Bayes' rule of probability, the joint probability distribution of unknown parameters and given measurements,  $P(x, y)$ , is represented as:

$$P(x, y) = P(x|y)P(y), \quad (4.2)$$

where  $x$  is the unknown parameters of interest and  $y$  is the given measurements.  $P(x|y)$  is the conditional probability distribution of  $x$  given  $y$ .  $P(y)$  is the marginalized probability distribution of  $y$ :  $P(y) = \int P(x, y)dx$ .

Therefore, the *posterior* probability of  $x$  given  $y$  is constructed as:

$$P(x|y) = \frac{P(x, y)}{P(y)} = \frac{P(y|x)P(x)}{P(y)}. \quad (4.3)$$

According to (4.3), our prior knowledge about the unknown parameters  $x$  is incorporated in prior term  $P(x)$  to produce the posterior probability distribution  $P(x|y)$ , given the data likelihood term  $P(y|x)$ . Since probability  $P(y)$  is independent of  $x$ , it is considered as a normalizing constant that can be omitted:

$$P(x|y) \propto P(y|x)P(x). \quad (4.4)$$

Different techniques can be used to analyze this posterior distribution. For example, *maximum a posterior* (MAP) estimation will produce an estimate of the mode of the

posterior distribution that maximizes the posterior probability. The solution of this optimization problem, however, gives a point estimate of  $x$  without providing information about its distribution. To fully characterize the posterior distribution of  $x$  when  $P(x|y)$  is not analytically tractable, simulated-based methods such as Markov Chain Monte Carlo (MCMC) or approximation methods such as Variational Bayes (VB) can be used [54, 55].

In this work, we focus on characterizing the full posterior distribution because we are interested in the posterior distribution of  $p$  in order to analyze the different combination of final models as determined by the ECG data.

#### 4.2.2 Hierarchical Multiple-Model Bayesian Inference to Volumetric Cardiac Source Imaging

From a Bayesian perspective, assuming the source  $\mathbf{v}$  and the measurement data  $\mathbf{b}$  as random variables, at each time instant, the posterior probability of the unknown cardiac source  $P(\mathbf{v} | \mathbf{b})$ , according to the Bayes' theory, is related to the prior distribution of the sources  $P(\mathbf{v})$  and the likelihood distribution of measurement data given sources  $P(\mathbf{b} | \mathbf{v})$ :

$$P(\mathbf{v} | \mathbf{b}) \propto P(\mathbf{b} | \mathbf{v})P(\mathbf{v}). \quad (4.5)$$

##### 4.2.2.1 Multiple-Model Prior Term

Fixed-model approaches of EP imaging consider a specific prior distribution for the source  $\mathbf{v}$  that imposes a pre-defined assumption on the source distribution. For example, considering Gaussian distribution for the sources imposes smoothness on the solution,

while assuming Laplace prior distribution for the sources induces sparsity on the solution.

Here, we consider  $Lp$ -norm prior for statistically independent sources  $\mathbf{v}$ ,  $\|\mathbf{v}\|_p = (\sum_i (v_i)^p)^{1/p}$ , represented using a zero-mean generalized Gaussian distribution [56] for the source prior as:

$$P(\mathbf{v} \mid p, \delta) = w(p)^n \delta^{-n} \exp(-c(p) \sum_i \left| \frac{v_i}{\delta} \right|^p), \quad (4.6)$$

$$w(p) = \frac{p\Gamma(3/p)^{1/2}}{2\Gamma(1/p)^{3/2}}, \quad c(p) = \left[ \frac{\Gamma(3/p)}{\Gamma(1/p)} \right]^{p/2},$$

where  $n$  denotes the number of sources and  $p$  represents the order of the  $Lp$ -norm prior. Fixing the  $p$  value to 1 or 2 converts the source prior distribution (4.6) to a Laplace distribution or Gaussian distribution, respectively. To incorporate a continuous combination of multiple models, we let  $p$  be an unknown random variable (hyperparameter). To give no prior preference over the value of  $p$ , we assume it to follow a uniform distribution between 1 and 2:

$$P(p) = \begin{cases} 1, & p \in [1, 2] \\ 0, & \text{otherwise} \end{cases}. \quad (4.7)$$

Parameter  $\delta$  denotes the variance (inverse of precision) of the source prior, assumed to be equal for all sources and constant over time. It plays a similar role to the regularization parameter in a deterministic setting, controlling the contribution of the source prior to

the regularization. To avoid the challenge of finding an optimal value for  $\delta$  through empirical studies, we also assume it to be an unknown hyperparameter with a uniform distribution.

#### 4.2.2.2 Data Likelihood Term

Assuming zero-mean normal distribution for the measurement noise, and spatially independent measurements  $\mathbf{b}$ , the likelihood term follows a Gaussian distribution as:

$$P(\mathbf{b} \mid \mathbf{v}, \eta) = \frac{1}{\sqrt{(2\pi)^m \eta^m}} \exp\left(-\frac{1}{2\eta^2} (\mathbf{b} - \mathbf{H}\mathbf{v})^T (\mathbf{b} - \mathbf{H}\mathbf{v})\right), \quad (4.8)$$

where  $m$  denotes the number of body-surface measurements and  $\eta^2$  represents the noise variance, assumed to be equal for all measurements. The noise variance controls the contribution of the data-fitting term to the regularization. Here, we also consider it to be an unknown hyperparameter with a uniform distribution.

Substituting the likelihood and prior terms in (4.5), the joint posterior distribution (4.5) can be re-formulated as:

$$P(\mathbf{v}, \Theta \mid \mathbf{b}) \propto P(\mathbf{b} \mid \mathbf{v}, \eta) P(\eta) P(\mathbf{v} \mid p, \delta) P(p) P(\delta), \quad (4.9)$$

where  $\Theta = \{\delta, p, \eta\}$  denotes a vector of size 3 including the three hyperparameters.

#### 4.2.2.3 Sampling the Posterior using MCMC

A full Bayesian analysis of this problem is obtained by sampling the joint posterior distribution (4.9) using a MCMC technique called slice sampling [57]. Slice sampling generates samples of a random variable by uniformly sampling from under the curve of its density function. Unlike Gibbs sampling [58] that requires conditional distributions of unknown random variables, or Metropolis-Hastings scheme [55] that requires an accurate selection of the proposal distribution for an efficient random walk, slice sampling enables us to directly sample the joint posterior distribution with minimum tuning required. Assuming a one-dimensional random variable  $z$  with probability density function proportional to  $f(z)$ , the single variable slice sampling can be summarized into 4 steps as:

(a) Take an initial value  $z_0$  for  $z$ .

(b) Draw a real value  $g$  uniformly from interval  $[0, f(z_0)]$ , defining a horizontal slice

$$S = \{z : g < f(z)\}.$$

(c) Find an interval  $I = (L, R)$  around  $z_0$  that contains all or most of the slice  $S$ : using stepping-out and shrinkage procedures, an interval of width  $w$  is randomly positioned around  $z_0$ , and then expanded in steps of size  $w$  until both ends are outside the slice. These two ends determine  $L$  and  $R$ , which in turn identify interval  $I$ .

(d) Draw a new sample  $z_1$  uniformly from the interval  $I$ , such that it belongs to the slice  $S$ . If it does not belong to slice  $S$ , use it to shrink the interval  $I$  and repeat step (d). If it belongs to slice  $S$ , accept it as a new sample and start over from step (b) using the new sample as a new initial value  $z_0$ .

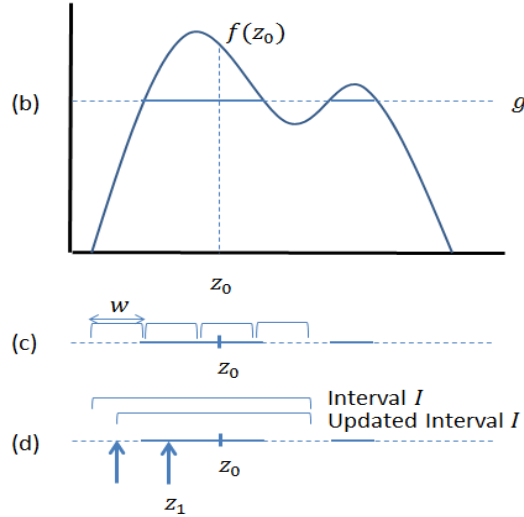


FIGURE 4.1: Single variable slice sampling with stepping-out and shrinkage procedures for selecting and updating an interval.

Different approaches can be utilized to select two ends of the interval  $I$  in step (c). Here, we use the stepping-out and shrinkage procedures to identify  $L$  and  $R$ , as explained in Fig. 4.1. For details of other interval selection methods refer to [57]. A multivariate distribution can be sampled by repeated use of univariate slice sampling to sample each variable in turn. To determine whether the samples are representative of the source distribution (convergence), several chains with different starting points are generated. Comparing the variance between different chains, the convergence is identified when the chains are no longer differentiable. In addition, the early iterations are discarded as they are under the influence of the starting point.

Given samples from the posterior distribution (4.9), the posterior distribution of sources  $P(\mathbf{v}|\mathbf{b})$  is calculated as an integral over hyperparameters  $\Theta$ :

$$P(\mathbf{v}|\mathbf{b}) = \int P(\mathbf{v}, \Theta|\mathbf{b}) d\Theta. \quad (4.10)$$

The integration of the joint probability distribution  $P(\mathbf{v}, \Theta|\mathbf{b})$  over three hyperparameters  $\Theta = \{p, \delta, \eta\}$  provides the marginal probability distribution of sources  $P(\mathbf{v}|\mathbf{b})$ . This integration (4.10) can be converted to a summation over the sample hyperparameters as:

$$P(\mathbf{v}|\mathbf{b}) = \sum_p \sum_\eta \sum_\delta P(\mathbf{v}, p, \eta, \delta|\mathbf{b}). \quad (4.11)$$

Therefore, a combination of multiple models (different  $p$  values in the  $Lp$ -norm prior) contributes to the final posterior distribution of cardiac sources  $P(\mathbf{v}|\mathbf{b})$ , where each model is weighted/modulated by the posterior probability of its occurrence determined by the data. To analyze the estimate of cardiac sources, we examine the posterior mean,  $E[P(\mathbf{v}|\mathbf{b})] = \sum_{j=1}^k \mathbf{v}^j P(\mathbf{v}^j|\mathbf{b})$ , where  $k$  is the number of samples.

### 4.3 Experiments and Results

We conduct two sets of synthetic and real-data experiments to evaluate the performance of the presented multiple-model approach in comparison to a fixed-model approach in reconstructing sources with different sizes and structures.

Both the multiple-model and fixed-model approaches are implemented using the same overall Bayesian framework as described in section II: for the former,  $p$  is treated as a hyperparameter as detailed earlier; for the latter, the value of  $p$  is fixed at 1 and 2 to represent, respectively, a Laplace (sparsity) and Gaussian (smoothness) density prior. For all experiments, slice sampling is executed with 3 chains, each with different initial value, containing 20000 samples. The number of chains and the length of each chain are

determined based on both sensitivity analysis and convergence criteria. Hyperparameter  $p$  is initialized to a uniformly selected value between 1 and 2. Similarly, source variance initial value is selected from the interval  $[0, 3]$ , where the bounds are defined large enough to cover all possible values for the source variance. Likewise, noise variance is uniformly picked from the interval  $[0.1, 10e - 5]$  to cover different noise levels. The first 3000 samples of each chain are dropped to remove the impact of the initial value on the samples. From these samples that represent the posterior distribution of the cardiac sources and hyperparameters (including  $p$ ), we focus our analysis on: 1) the distribution of  $p$  as an indication of the model combination preferred by the data; and 2) posterior mean of cardiac sources in order to evaluate the accuracy of the estimation.

### 4.3.1 Synthetic Experiments

To test the impact of the prior model on the accuracy of source construction, we conduct three different sets of synthetic experiments on image-derived human heart-torso models. The torso surface is represented by 370 nodes. The heart volumes are represented by evenly-distributed nodes with resolution between  $4mm$  to  $7mm$ . The 3D source reconstruction accuracy is measured in terms of correlation coefficient (CC) between the true sources and the posterior mean of estimated sources, defined:

$$CC = \frac{\mathbf{v}_e - \bar{\mathbf{v}}_e}{\|\mathbf{v}_e - \bar{\mathbf{v}}_e\|} \cdot \frac{\mathbf{v}_s - \bar{\mathbf{v}}_s}{\|\mathbf{v}_s - \bar{\mathbf{v}}_s\|}, \quad (4.12)$$

where  $\mathbf{v}_s$  and  $\mathbf{v}_e$  are the true sources and the posterior mean of estimated sources, respectively.  $\|\cdot\|$  represents the magnitude of a vector and  $\bar{\mathbf{v}}$  denotes the mean of a vector.

#### 4.3.1.1 Imaging Cardiac Sources with Various Sizes

In this set of experiments, we investigate the effect of prior models when the cardiac sources to be reconstructed range in sizes from 5% to 40% of the ventricles. In total, 40 different settings are considered, where active source region is placed at different locations in the ventricular myocardium. Cardiac sources within the active region are assigned with value 1, while the rest are assigned with value 0. It is noteworthy that these settings do not reflect physiologically meaningful configurations of cardiac sources typically seen in the heart. They are meant to mimic the change in sparse *vs.* diffuse structures in cardiac sources in a simplified manner, with a focus on revealing how these changes may affect the need of different prior models. For example, settings of focal and extended sources resemble sparse source distribution at the beginning of the excitation and extended source distribution along diseased regions of the heart, respectively. For each setting, 370-lead ECG data is simulated and corrupted with 20 dB Gaussian noise as input in the multiple-model approach.

Fig. 4.2 presents three examples, where the active source region is centered at left ventricle (LV) apex and covered 6% , 17%, and 40% of LV (Fig. 4.2A, 4.2B, and 4.2C), respectively. The use of a sparse Laplace prior is able to detect the focal source ( $CC= 0.69$ ), but its performance decreases when the region of active sources expands ( $CC= 0.60$  and  $0.40$ ). In contrast, using a smooth Gaussian prior provides an overly-smooth solution for the focal source region ( $CC= 0.52$ ), but it obtains better estimation of larger source regions ( $CC= 0.65$  and  $0.68$ ). By using a multiple-model prior, the posterior mean is similar in accuracy to that obtained with a Laplace prior for the focal region ( $CC= 0.67$ , Fig. 4.2A), but it outperforms both fixed-model approaches in larger source regions with  $CC= 0.70$  and  $0.74$  (Fig. 4.2B and 4.2C). Interestingly, distributions

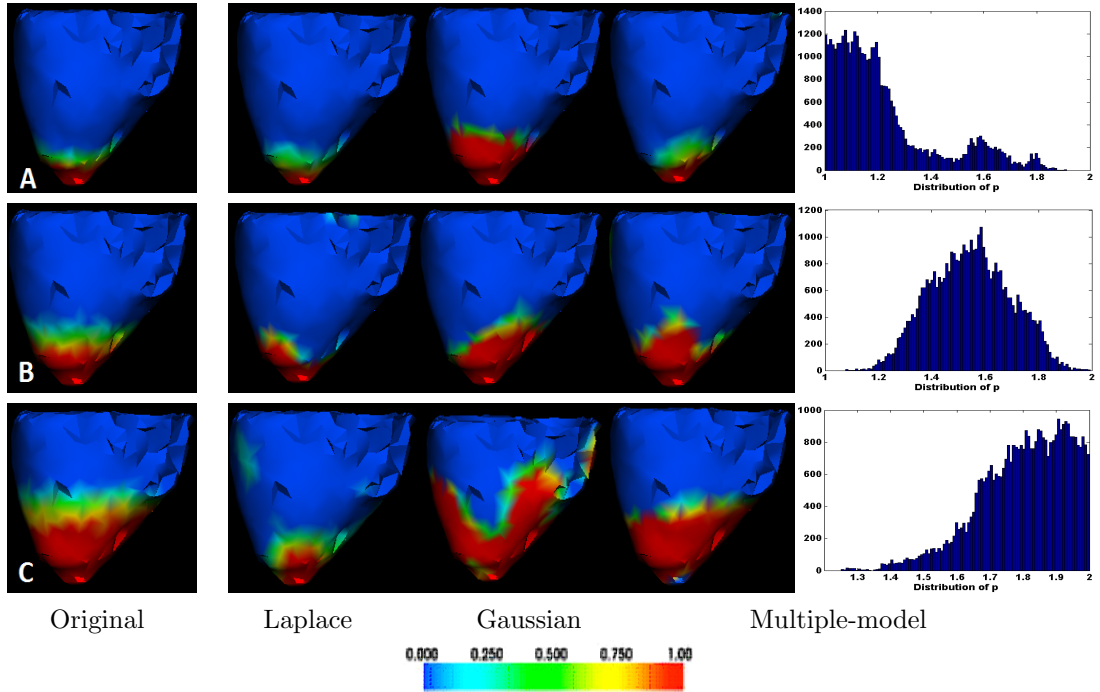


FIGURE 4.2: Three examples of the posterior mean of reconstructed 3D sources using multiple-model prior *vs.* Laplace and Gaussian priors. Active sources are centered at the apex of LV and covered 6%, 17%, and 40% of the myocardium in A, B and C, respectively. Posterior distributions of hyperparameter  $p$  for the three cases are also shown in the rightmost panel.

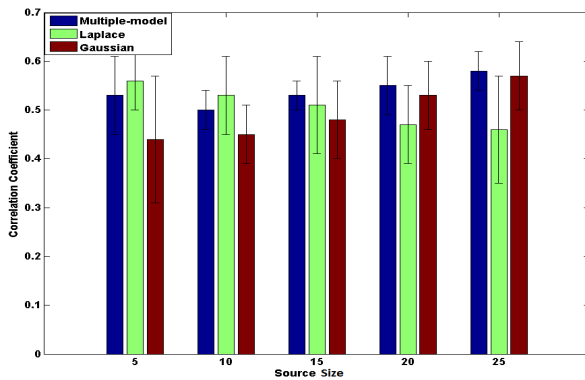


FIGURE 4.3: Comparison of multiple-model prior with Laplace and Gaussian priors in reconstructing active source regions with different sizes. Source size is defined in terms of percentage of the ventricular myocardium.

of hyperparameter  $p$  for these 3 cases (Fig. 4.2) suggest that higher weights are assigned by data to the value of  $p$  closer to 1 for the focal source. This weight distribution for  $p$  shifts to higher values closer to 2 when the source region expands.

As illustrated in Fig. 4.3, in these 40 different settings of source distributions, the use of

multiple-model prior delivers consistent results for sources with various sizes, while the use of fixed-model priors only satisfactorily captures specific types of source distributions. One-way ANOVA test is used to check (test) the overall difference between the mean results of multiple-model prior ( $CC = 0.52 \pm 0.08$ ), Laplace prior ( $CC = 0.50 \pm 0.11$ ), and Gaussian prior ( $CC = 0.48 \pm 0.13$ ) among all source region sizes and all locations. The ANOVA test reports non-significant difference among three groups, which might be due to: 1) simplicity of the settings that Laplace and Gaussian priors perform relatively well in estimating a compact source region, confirmed by the very symmetric distribution of  $p$ , or 2) dependency of the results on the source region size, meaning that the overall mean of Laplace and Gaussian priors is similar while Laplace prior provides accurate results for small source regions and not very accurate results for large source regions and Gaussian prior behaves vice versa. Therefore, we also perform the paired student's t-test, reporting the multiple-model prior significantly higher accuracy than that of the Laplace or Gaussian priors ( $p < 0.005$ ).

This set of experiments demonstrates that different models are required to successfully estimate sources with different sizes and structures. While fixed-model approaches better detect specific source regions, adaptively changing the distribution of  $p$  (model combinations) according to the data is capable of estimating source regions with different sizes and structures.

#### 4.3.1.2 Imaging Cardiac Source Distribution along the Infarct Border

In the second set of synthetic experiments, we examine the feasibility of the proposed method in estimating the source distribution along the infarct border during the ST segment of an ECG cycle. During the ST segment of an ECG cycle, in an infarcted heart, only the viable myocardium would exhibit coherent high action potential, while

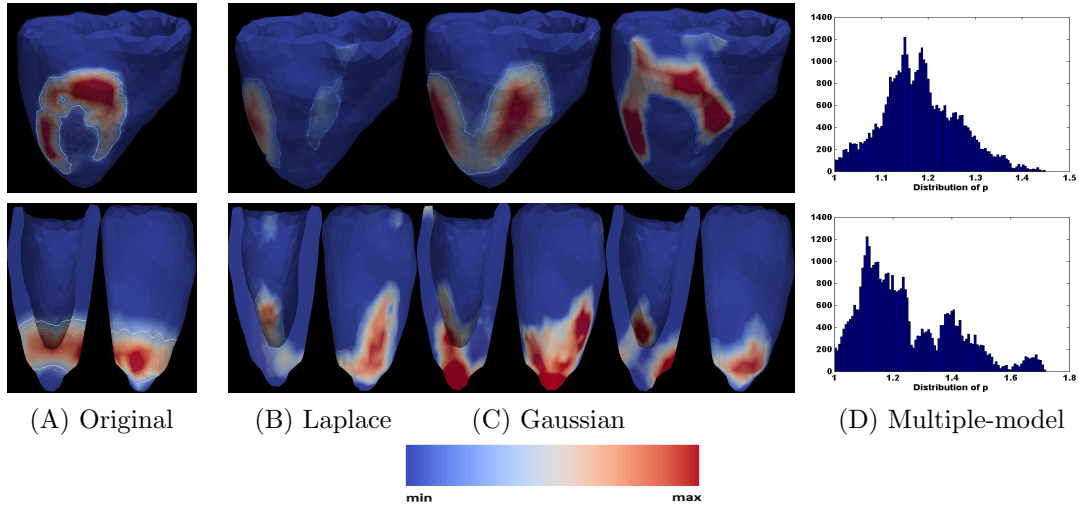


FIGURE 4.4: Two examples of the posterior mean estimate of the source distribution (the spatial gradient of action potential) along the infarct border during the ST segment of an ECG cycle, where the infarct is centered at the middle to apical region at the anterior wall of LV (top row) and at the apex (bottom row). The  $p$  distribution obtained by our method is also shown at the rightmost panel.

the necrotic tissue in the scar core exhibits low potential. These two regions are separated by the infarct border with localized cardiac sources. In total, we consider 116 cases of infarcts at different locations and with different border sizes ranging from 5% to 55% of the LV. In these experiments, action potential at the core of infarct regions is set to 0, while it is set to 1 at healthy regions. The *true* cardiac source distribution along the infarct border is therefore calculated as spatial gradient of action potential. Finally, body-surface ECG measurements associated with each setting are simulated and corrupted with 20 dB (SNR) Gaussian noise to serve as the input for the multiple-model approach.

Fig. 4.4 presents two examples of imaging 3D source distribution along infarct border. In the top row, infarct core is located at the middle to apical region at the anterior wall of LV; in the bottom row, infarct is centered at the apex of LV (Fig. 4.4A). As shown, the use of Laplace prior detects a few sparse patches of active sources without providing information about the center or structure of the infarct region (Fig. 4.4B, CC= 0.25 top row, and CC= 0.37 bottom row). The use of Gaussian prior better identifies the

infarct region, though its estimations are smeared, such that the estimated sources extend to the infarct center (Fig. 4.4C, CC= 0.43 top row, and CC= 0.44 bottom row). The source distributions along the infarct are significantly better estimated using the multiple-model prior, outlining both the location and shape of the infarct (Fig. 4.4D, CC= 0.67 top row, and CC= 0.63 bottom row). In addition, as shown in the estimated posterior distribution of  $p$  in Fig. 4.4D, the optimal ranges of value for  $p$  differ with cases, indicating different source structures preferred different set of prior models. In the example at the top row, the  $p$  distribution is centered around 1.2 and stretched equally on both sides, implying a region with small to medium size (37% of the LV). In the example at the bottom row, the value of  $p$  is mainly distributed between 1 and 1.2, indicating a relatively small source region (25% of the LV).

Fig. 4.5 summarizes multiple-model prior performance compared to that of fixed-model approaches in reconstructing source distributions along the infarct border with different sizes. Unlike Laplace and Gaussian priors that satisfactorily capture specific types of source distributions, multiple-model prior obtains consistent results for sources with various sizes. In these 116 settings, multiple-model prior results with overall accuracy CC=  $0.55 \pm 0.09$  are significantly better than that of Laplace and Gaussian priors (CC=  $0.45 \pm 0.12$  and CC=  $0.46 \pm 0.08$ , respectively) based on one-way ANOVA test ( $p = 3.7512e - 014$ ) followed by paired student's t-test ( $p < 0.005$ ).

These experiments illustrate the advantage of multiple-model prior in estimating source distribution along the infarct border. Since the infarct border size/structure is not known *a priori*, fixed-model approaches run the risk of imposing constraints on the source distribution that are not consistent with the underlying source structures. In contrast, multiple-model prior reflects the source structure through the weights ( $p$  distribution) estimated for the models to correctly identify the infarct border.

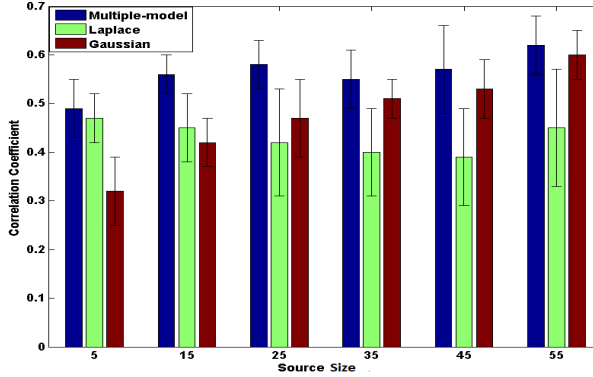


FIGURE 4.5: Comparison of multiple-model prior with Laplace and Gaussian priors in reconstructing active source distribution along the infarct border. Source size represents the size of active sources along the infarct border and is defined in terms of percentage of the left ventricle.

#### 4.3.1.3 Imaging Excitation/Repolarization Wavefront in Cardiac Pacing

In this set of experiments, we increase the complexity of the experimental settings and consider realistic structures of sources that are generated by Aliev-Panfilov model [59] describing spatiotemporal propagation of action potentials in the ventricles. Four different heart geometries are used in these experiments. These heart models are coupled with identical 370-vertices torso. For each heart model, 5 different random pacing locations are considered. For each pacing location, action potential propagation are simulated during a cardiac cycle using Aliev-Panfilov model. Next, the spatial gradient of action potential is calculated to obtain *true* cardiac source distribution representing excitation/repolarization wavefront in the cardiac cycle. The corresponding 370-lead body-surface measurements are simulated and corrupted with 20 dB noise. The performance of multiple- *vs.* fixed-model approached is evaluated in reconstructing the propagation of cardiac sources at 20 different time instants during a cardiac cycle.

Fig. 4.6 presents an example of excitation wavefront propagation at 4 time instants during depolarization phase of an ECG cycle. In this example, the pacing location is at the base of right ventricle (Fig. 4.6A, top row). The use of Laplace prior produces

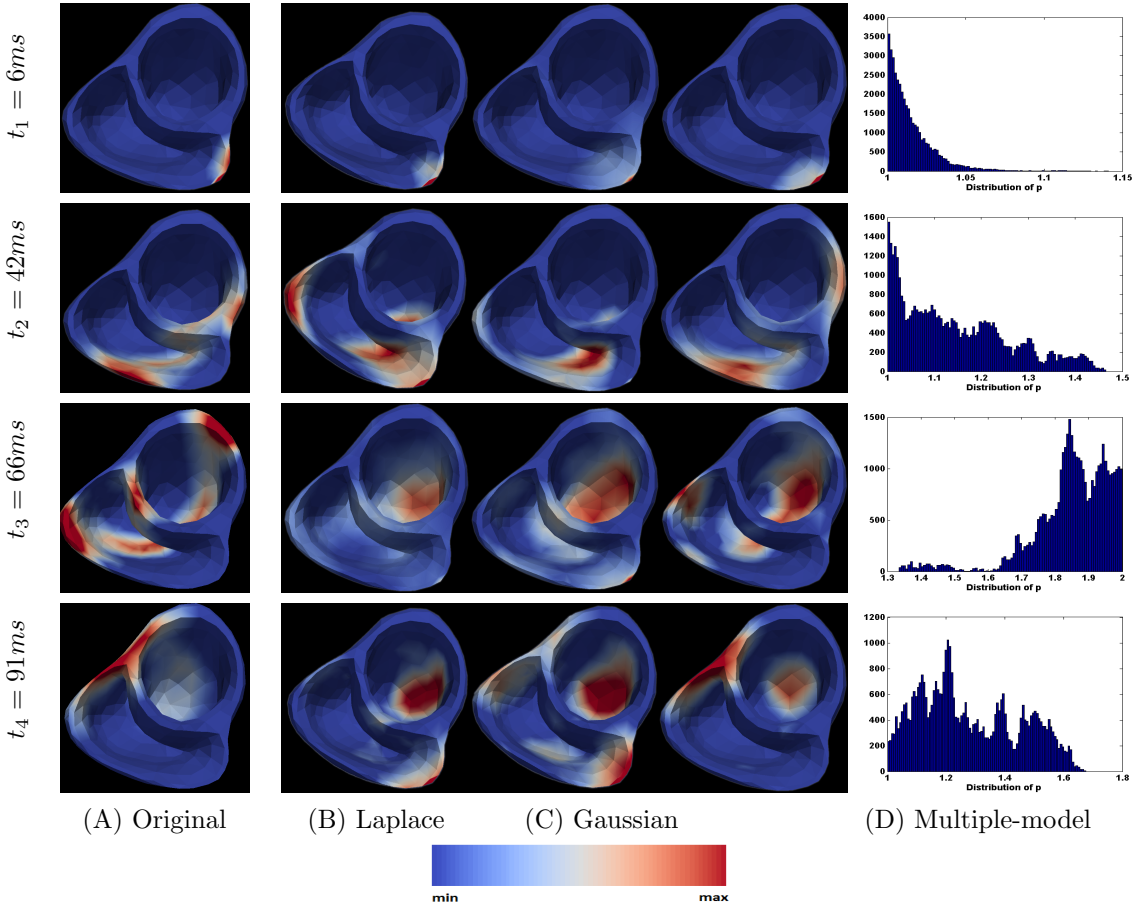


FIGURE 4.6: An example of imaging excitation wavefront propagation in cardiac pacing at 4 time instants during the depolarization phase of an ECG cycle. The pacing point is located at the base of right ventricle. Active source region represents the spatial gradient of action potential.

relatively sparse solutions (Fig. 4.6B) that accurately detects source distribution at the very beginning of the pacing ( $t_1$ , CC= 0.73). Its performance, however, decreases when the source region become larger such that only part of the active region is identified ( $t_2$ : CC= 0.42,  $t_3$ : CC= 0.37, and  $t_4$ : CC= 0.26). Its solution also involves false source detection at two time instants ( $t_2, t_4$ ). Gaussian prior solution (Fig. 4.6C) is more consistent with the original source propagation, though it has a false-positive source region at  $t_4$  and a relatively more diffuse over-estimation of the focal source at  $t_1$  ( $t_1$ : CC= 0.69,  $t_2$ : CC= 0.47,  $t_3$ : CC= 0.41, and  $t_4$ : CC= 0.35). The use of multiple-model prior obtains the source detection with the highest CC throughout different time instants, with less false-positive detection (Fig. 4.6D,  $t_1$ : CC= 0.71,  $t_2$ : CC= 0.59,  $t_3$ :

$\text{CC} = 0.53$ , and  $t_4$ :  $\text{CC} = 0.64$ ). The posterior distribution of  $p$  is also consistent with the size of different sources (Fig. 4.6D, the rightmost panel). At  $t_1$ , when the source region is very focal,  $p$  distribution favors values close to 1. When the source region expands, in the subsequent time instants, the  $p$  distribution shifts toward 2, such that the largest source region ( $t_3$ ) favors  $p$  values very close to 2. The fact that the posterior distribution of  $p$  varies with the spatiotemporal change of the propagating source clearly demonstrates the need of automatically adapting the prior models when imaging spatiotemporally varying cardiac sources. Furthermore, it is noteworthy that the posterior distribution of  $p$  is associated with larger variance, and more complex shape as the spatial structure of the cardiac sources become more complex in the second (Fig. 4.4) and third (Fig. 4.6) set of synthetic experiments, indicating the need of combining multiple models instead of identifying one single fixed model to constrain the imaging.

We also take a closer look at an example pacing in one cardiac cycle to study the performance of the multiple-model prior compared to fixed-model approaches over time. Fig. 4.7 shows the CC obtained by multiple-model prior and Laplace and Gaussian priors during depolarization and repolarization phases, each at 5 time instants. The CC accuracy is more consistent for multiple-model prior over a cardiac cycle while fixed-model approaches fluctuate more often over time. Low standard deviation (STD) of multiple-model prior ( $\pm 0.03$ ) also confirms its consistent performance over time compared to higher STD of fixed-model approaches (Laplace prior STD:  $\pm 0.08$ , and Gaussian prior STD:  $\pm 0.06$ ).

For this set of experiments, the overall performance of multiple-model prior in imaging excitation and repolarization wavefronts during three stages of an ECG cycle is summarized in Fig. 4.8, in comparison with fixed-model approaches. At early excitation phase, where sources are sparse, our method performance compares with that of Laplace

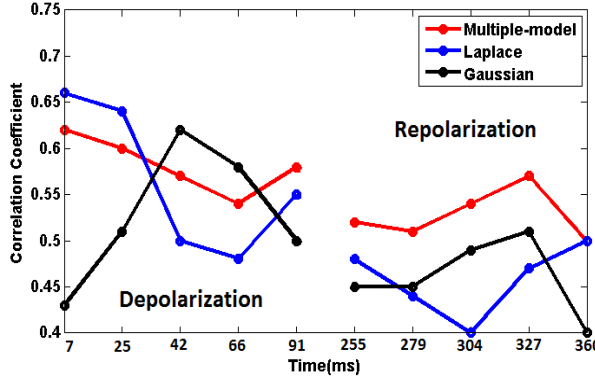


FIGURE 4.7: Comparison of multiple-model prior with Laplace and Gaussian priors in reconstructing excitation and repolarization wavefronts during an example pacing in one cardiac cycle.

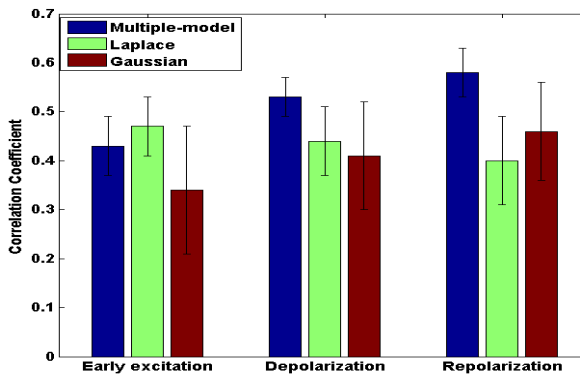


FIGURE 4.8: Overall comparison of multiple-model prior with Laplace and Gaussian priors in reconstructing excitation and repolarization wavefronts in three stages of an ECG cycle.

prior. Nevertheless, multiple-model prior outperforms fixed-model approaches in other phases of an ECG cycle. Conducting one-way ANOVA test on the results obtained using multiple-model prior as well as Laplace and Gaussian priors ( $CC = 0.53 \pm 0.05$ ,  $CC = 0.44 \pm 0.07$ , and  $CC = 0.42 \pm 0.11$ , respectively) reports that at least one group mean is significantly different from the other group means with  $p = 5.5128e - 073$ . The paired student's t-test also confirms that multiple-model prior results are significantly higher than that of Laplace and Gaussian priors with  $p < 0.005$ .

These experiments demonstrate that time-varying cardiac source structures call for not only an automatic adaptation of the prior models to the ECG data, but also the combination of multiple models rather than an optimal model in constraining the imaging.

### 4.3.2 Real-Data Experiments

Real-data experiments are conducted on two different groups of post-infarction patients. As explained earlier, in an infarcted heart, cardiac source activity is expected to be seen along the border of the infarct core during the ST segment of the ECG cycle. The reference infarct region for the first four patients is provided by cardiologists who examined the delayed enhancement MRI of the four patients, while the other two patients have voltage mapping as reference.

#### 4.3.2.1 Imaging Infarct Region using MRI as Reference

The first four patients underwent cardiac MRI for 3D infarct enhancement. Detailed specification of these four datasets is described in Chapter 3, section 4.2.

As shown in Fig. 4.9A, the center of infarct region (black contour) in case 1 is located at mid-anteroseptal of the heart. The sparse solution of Laplace prior only detects part of the infarct region border. The overly-diffused estimation of Gaussian prior does not reveal any information about the location or structure of the infarct region. In comparison, multiple-model prior is able to outline the distribution of sources along the infarct region (non-blue regions). Similar performance is observed in case 2, where the infarct region extends from basal inferior and inferoseptal to mid-inferior and inferoseptal. In case 3, the infarct region is centered at mid-inferior of the LV and extended to the septum and inferior LV. Multiple-model prior outperforms estimations obtained using Laplace and Gaussian priors as they both include a false positive infarct region at the right ventricle (RV). Case 4 has two infarct regions centered at basal anterior and apical inferior. Laplace prior behaves similar to other cases. Gaussian prior could only detect one of the infarct regions, which is falsely extended to RV. Multiple-model prior precisely

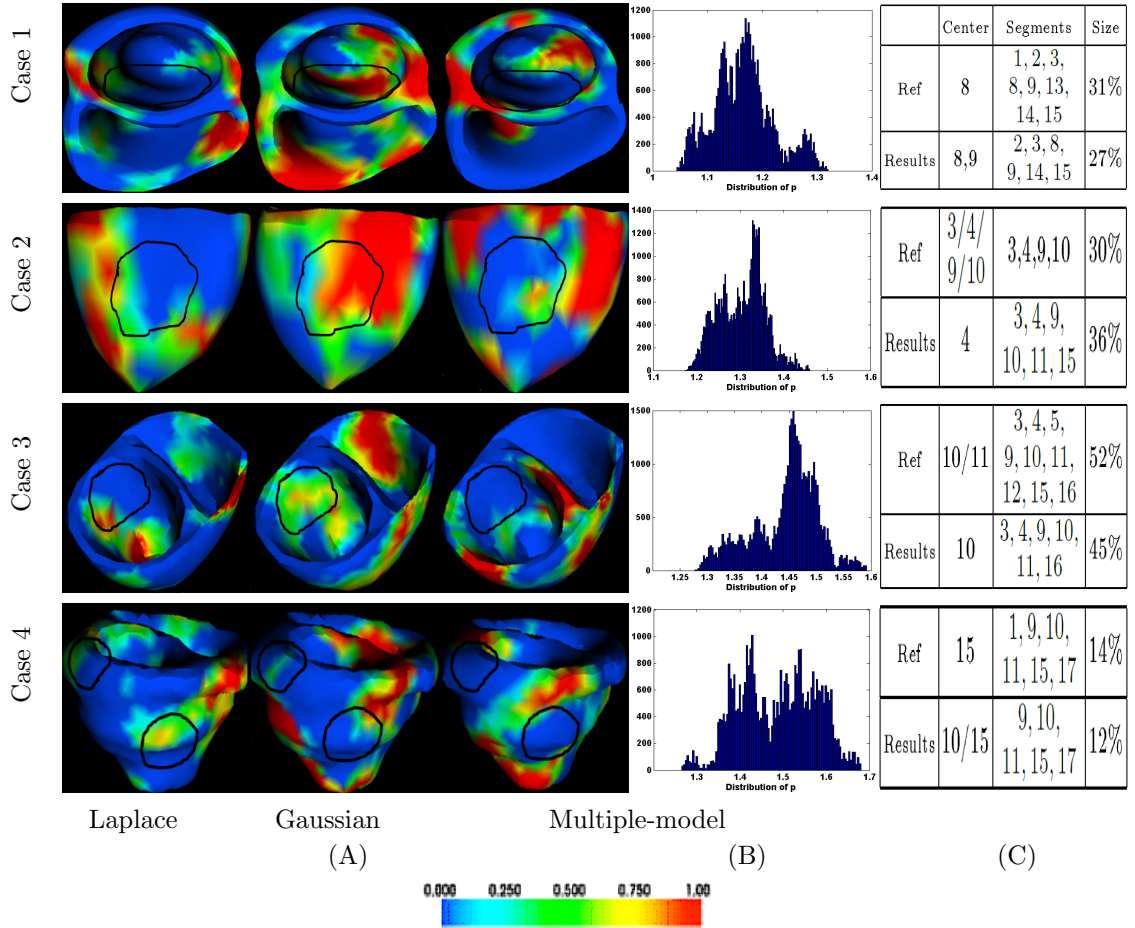


FIGURE 4.9: Estimation of cardiac source activity (non-blue color) along the infarct region border (black contour) during the ECG ST segment for 4 human subjects. Active source region represents the spatial gradient of action potential.

detects the infarct region located at apical inferior, although it only shows some source activity around basal anterior without providing more information about the infarct structure/size.

For quantitative evaluation, we threshold the solution to obtain the region bordering the infarct core. The threshold value is decided by repeated application of  $k$ -mean clustering, where  $k$  is first set to a large value and then is decreased in order to find an appropriate number of clusters. The difference between clusters' values determines the threshold value. This approach is similar to region growing technique, where a large  $k$  value in  $k$ -mean clustering results in a large number of small regions. By decreasing the  $k$  value the

TABLE 4.1: Comparison of infarct quantification with best existing results

		Reference	Our method	Xu	Wang	Mneimneh	Dawoud	Farina
case 3	size	52%	45%	N/A	47%	27%	35%	10%
	center	10/11	10	10/15	10	10/11	4	12
	segments	3,4,5,9,10, 11,12,15,16	3,4,9,10,11,16	3,8,9,10,11,12,14,15,17	2,3,4,5,8,11,12,16,17	N/A	3,4,5,10,11	N/A
case 4	size	14%	12%	N/A	11%	12%	40%	0.2%
	center	15	10/15	15	9	N/A	4	11
	segments	1,9,10,11,15,17	9,10,11,15,17	1,7,9,10,11,15,17	1,4,6,7,9,14	N/A	3,4,5,6,9,10,1	N/A

size of regions start to grow until appropriate region size is achieved. We then calculate the infarct region in terms of location (using the 17-segment model of LV) and size (ratio of infarct region volume to the total LV volume), as shown in Fig. 4.9C. Interestingly, as shown in Fig. 4.9B, in cases 1 and 2 that have relatively compact infarct regions (30%), the posterior density of  $p$  exhibits a relatively compact distribution centered around 1.2. For case 3 that has a large infarct region (52%), the distribution of  $p$  shifts toward higher values ( $\sim 1.5$ ) with a larger tail on one side. In case 4, although the infarct region is small (14%), the source distribution is expected to be more diffused because of the presence of two separate infarct regions. Accordingly, the posterior density of  $p$  is more evenly distributed from 1.4 to 1.6 with a larger variance. These results further demonstrate the capability and necessity of a multiple-model approach to automatically adjust the contribution of different models based on the source structure and, in some cases, to utilize a set of more evenly weighted models than one optimal model when dealing with complex source structures.

Table 4.1 compares the accuracy of infarct quantification for cases 3 and 4 with the results obtained on the same data by five other methods. In brief, Xu *et al.* solves the problem by estimating the volumetric action potential using a total-variation prior [18]. Wang *et al.* obtains volumetric action potential using a physiological-model based maximum *a posteriori* estimation [60]. Dawoud *et al.* reconstructs epicardial potential

from body-surface measurements using Tikhonov regularization followed by a morphology classification to calculate infarct size and location [4]. Farina *et al.* uses a spherical infarct model inside a detailed 3D cardiac excitation model to deterministically optimize the infarct location and size [61], and Mneimneh *et al.* directly analyzes the ECG without solving any inverse EP imaging problems. [62]. As shown, in both cases, the results obtained by multiple-model prior are comparable to volumetric action potential imaging methods [18, 60] and outperformed the other three approaches [4, 61, 62]. It also reports less false positive infarct compared to those in [18, 60].

#### 4.3.2.2 Imaging Infarct Region using Voltage Mapping as Reference

The other two patients have ventricular tachycardia due to previous infarct and underwent catheter voltage mapping of the scar substrates. The datasets include CT images of heart/torso geometries as well as 123-lead BSP measurements for each subject that are acquired at the *Cardiac Electrophysiology Laboratory of the QEII Health Sciences Center, Halifax, Canada* [63]. Axial CT scans of these two cases include slices with 0.8-3 mm inter-slice spacing and 0.86 mm pixel spacing. The torso surface for these two cases is described by triangular elements with 120 vertices. Patient-specific heart-torso models are constructed from CT scans of individual patients. BSP measurements are recorded by Dalhousie University standards [48] at 123 known anatomical sites; each BSP recording consisted of a single averaged PQRST complex sampled at 2 kHz. For these two patients, the reference infarct data is obtained through invasive bipolar voltage recordings collected on the epicardium of the heart using the CARTO system [63]. Infarct core is identified as a region with peak-to-peak bipolar voltage  $< 0.5mV$  and the region with voltage between 0.5 mV to 1.5 mV indicates infarct border. CARTO data is registered to CT first through a rigid alignment based on visual inspection using

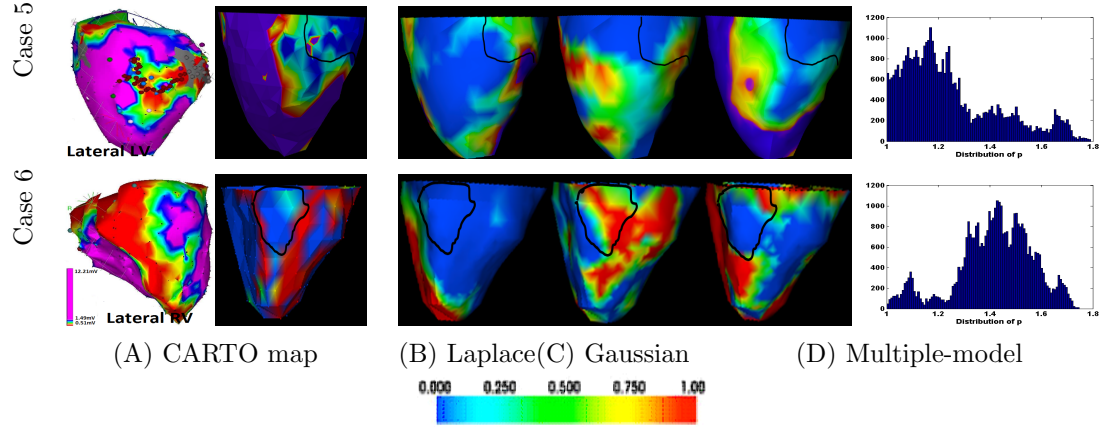


FIGURE 4.10: (A) CARTO map (the leftmost panel) and its spatial gradient (non-blue region) projected on the heart surface with highlighted infarct region (black contour). (B-D) Estimation of cardiac source activity (non-blue color) along the border of the infarct region. Active source region represents the spatial gradient of action potential.

Amira 4.1 software (Mercury Computer Systems, Chelmsford, MA), followed by coherent point drifting method for non-rigid registration [64, 65]. Infarct region is identified after thresholding as described earlier, and its quantitative accuracy is evaluated in terms of overlap (SO) with the infarct region delineated from the CARTO voltage map. SO is defined as intersection between estimated and reference source regions over union of estimated and reference source regions. Note that SO is half of the Dice coefficient commonly used in segmentation techniques.

As shown in Fig. 4.10, the use of Laplace prior can partially identify source activity along the infarct border without providing detailed information about the structure of the infarct core (case 5: SO= 0.34, case 6: SO= 0.31). The use of Gaussian prior has better estimation of source distribution along infarct border in case 5 (SO= 0.48) while its estimation in case 6 is smeared and extended to the infarct center (SO= 0.36). Multiple-model prior performance in delineating the infarct core is improved compared to fixed models in both cases (case 5: SO= 0.51, case 6: SO= 0.53). Specifically in case 6, multiple-model prior not only identifies the infarct region, it detects the source activity at heterogeneous region close to the apex. Similar to previous observations, in

these real-data experiments with complex infarct structures, the posterior density of  $p$  exhibits a more even and complex distribution with larger variances.

## 4.4 Discussions

### 1) Comparison with Multiple-Constraint Regularization Method by Brooks *et al.* [6]

As mentioned in the introduction, the proposed multiple-model prior is conceptually similar to multiple-constraint regularization method proposed by Brooks *et al.* for estimating epicardial potential distribution from body-surface measurements [6]. Brooks deterministic approach imposes a finite set of prior models with different orders of  $L2$ -norm on spatial property of equivalent cardiac sources on the epicardium. A special case of this deterministic regularization method with zero-order and first-order Tikhonov constraints is then used for epicardial potential imaging, formulated as:

$$\min_{\mathbf{v}} \|\mathbf{b} - \mathbf{Hv}\| + \lambda_1 \|\mathbf{v}\|_2 + \lambda_2 \|\mathbf{Rv}\|_2, \quad (4.13)$$

where,  $\mathbf{R}$  is the gradient matrix,  $\lambda_1$  and  $\lambda_2$  are regularization parameters, and  $\mathbf{v}$  is equivalent cardiac sources on the epicardium. For more details of this method refer to [6].

Here, we implement and compare this method with the presented multiple-model Bayesian approach for imaging volumetric cardiac sources. Regularization parameters are determined using L-surface method, as explained in [6] as an extension of L-curve method.

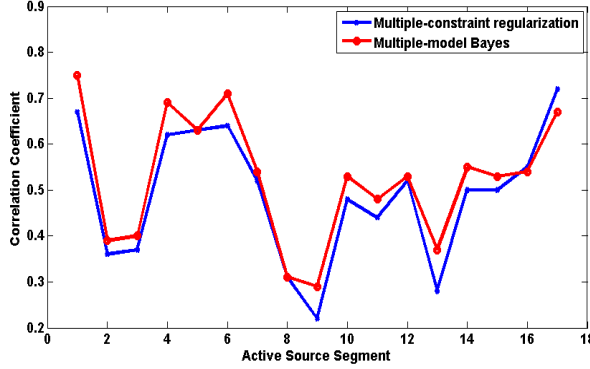


FIGURE 4.11: Comparison of the presented multiple-model Bayesian approach with Brooks *et al.* multiple-constraint regularization [6] in imaging volumetric sources located at different segments of LV defined according to standard 17-segment model of LV.

We consider 17 different settings, where active sources are located at different segments of LV defined according to standard AHA 17-segment model of LV [49]. The active source segment is set to value 1, while the rest is set to value 0. For each setting, the body-surface measurements are simulated and corrupted with 20 dB Gaussian noise.

Fig. 4.11 shows the results obtained by the presented multiple-model Bayesian approach compared to Brooks *et al.* multiple-constraint regularization. While both approaches obtain similar performance trend in these 17 different settings, the presented multiple-model Bayes provides better overall source estimation ( $CC = 0.52 \pm 0.14$ ) compared to Brooks multiple-constraint regularization ( $CC = 0.49 \pm 0.13$ ). According to paired student t-test, the multiple-model Bayes obtains significantly higher accuracy ( $p = 0.005$ ); though a larger experiments set is required for more conclusive comparison.

It must be noted that Brooks method is originally aimed to estimate epicardial potential distribution while its implementation in this work targets estimation of volumetric sources in the myocardium.

The Bayesian framework of the multiple-model approach enables automatic estimation of hyperparameters such as distribution of  $p$ , source variance and noise variance in

addition to source distribution. In comparison, the multiple-constraint regularization involves the challenge of finding proper regularization parameters for the generic model, although this challenge is overcome in the special case of two constraints using L-surface method.

## 2) Posterior Mean *vs.* MAP Estimators

In this work, we use the posterior mean of the source distribution to evaluate the accuracy of the estimation of cardiac sources. This choice is made based on the assumption about the distribution of measurements and sources that followed Gaussian distribution and generalized Gaussian distribution, respectively. As a result, the posterior distribution of sources follows generalized Gaussian distribution, which is a unimodal distribution that justifies the posterior mean as a valid point estimator for the sources. This unimodal distribution also indicates that MAP and posterior mean would provide close results.

For comparison purposes, we also calculate MAP estimation of the source distribution in the second set of synthetic experiments. Examples of two source distributions obtained using slice sampling are shown in Fig. 4.12A. As shown, the unimodal posterior distribution of sources explains comparable results of MAP and posterior mean estimators (as shown in Fig. 4.12B). A slightly lower accuracy of MAP estimator can be explained by its sensitivity to sampling errors in the solution while posterior mean is more robust to these errors by averaging over a set of solutions.

## 3) Deterministic Formulation of Proposed Bayesian Method

The posterior distribution (4.9) being solved in this work can be formulated in a deterministic form by taking negative logarithm from two sides of the equation (4.9) as:

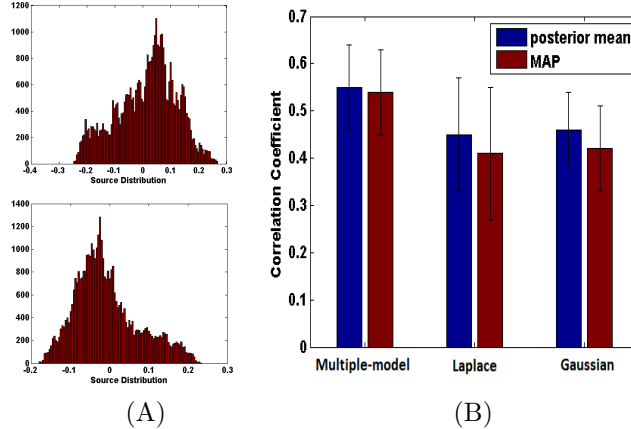


FIGURE 4.12: (A) Examples of posterior distribution of two sources obtained using slice sampling. (B) Comparison of Map *vs.* posterior mean estimators for multiple-model prior as well as Laplace and Gaussian priors for the second set of synthetic experiments.

$$\begin{aligned} -\log(P(\mathbf{v}, \Theta | \mathbf{b})) &\propto -\log(P(\mathbf{b} | \mathbf{v}, \eta)) - \log(P(\mathbf{v} | p, \delta)) \\ &\quad -c, \end{aligned} \tag{4.14}$$

where  $c$  is a constant value resulted from taking logarithm of uniform distribution of the hyperparameters. Dropping the constant  $c$  and calculating the logarithm of the likelihood and the source prior terms would convert (4.14) to:

$$-\log(P(\mathbf{v}, \Theta | \mathbf{b})) \propto \|\mathbf{b} - \mathbf{Hv}\| + \lambda \|\mathbf{v}\|_p, \tag{4.15}$$

where the regularization parameter  $\lambda$  is determined from noise variance  $\eta^2$  and source variance  $\delta$ . Using the posterior mean as a point estimator for cardiac sources is then equivalent to taking the expectation of (4.15).

Solving this problem for Laplace or Gaussian prior distribution for the sources converts the functional (4.15) to:

$$\|\mathbf{b} - \mathbf{Hv}\| + \lambda \|\mathbf{v}\|_z, \quad z = 1 \text{ or } 2, \quad (4.16)$$

where  $z = 1$  ( $L1$ -norm) is equivalent to assuming Laplace distribution for the sources while  $z = 2$  ( $L2$ -norm) corresponds to Gaussian distribution for the sources. Posterior mean of the source distribution is then equivalent to taking the expectation of the functional (4.16). Note that solving (4.16) in a Bayesian framework, the regularization parameter ( $\lambda$ ) is automatically estimated along with the source distribution. It is noteworthy that posterior distribution (4.9,4.14,4.15) instead of an MAP estimate is being sought in this work because of our interest in analyzing the full posterior distribution of the hyperparameter  $p$ , with the intention to examine the model combination as determined by ECG data.

#### 4) Initialization Impact

Another advantage of the proposed Bayesian approach is in considering source variance  $\delta$  and noise variance  $\eta^2$  as hyperparameters and estimating them in addition to source distribution. As mentioned in the methodology section, the values of  $\delta$  and  $\eta$  affect the accuracy of Bayesian inference by controlling the contribution of the prior and the data-fitting term. To verify the robustness of our approach to initial values of these parameters, we conduct experiments with different measurement noises (SNR levels ranging from 50 to 10 dB). For all experiments, initial values of  $\delta$  and  $\eta$  are identical. As shown in Fig. 4.13, a slight change in CC value of different measurement noises

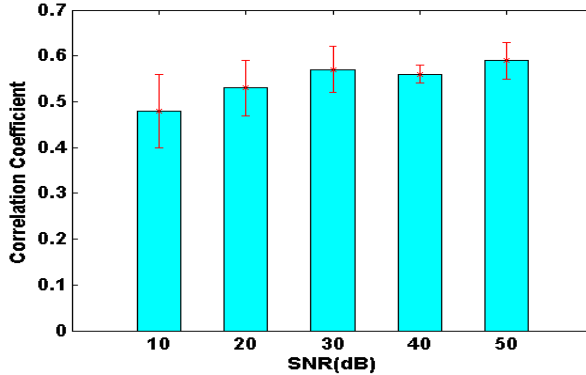


FIGURE 4.13: Correlation coefficient obtained using multiple-model prior for active sources in the presence of white Gaussian noises with different SNR levels.

demonstrates the ability of the hierarchical approach to automatically adapt hyperparameter values to deliver high performance. In these experiments, the final value of  $\delta$  is mainly distributed over the range of 0.3 to 0.6, regardless of its initial value.

### 5) Computational Cost

Our proposed approach obtains full posterior distribution of sources and hyperparameters by relying on MCMC slice sampling technique to obtain samples from the high-dimensional solution space (in the order of 1000). As a result of this high-dimensional solution space, it takes an average of 1 minute to converge on an iMac 2.9GHz Quad-Core Intel Core i5 with 16GB DDR3 SDRAM. The computational cost of Laplace and Gaussian priors implemented in this work (by fixing  $p$  value to 1 and 2, respectively) is similar because they also rely on sampling the same high-dimensional solution space with one less hyperparameter. In comparison, regularization methods take an average of 20 seconds to obtain a point estimate (rather than the full distribution) on the same machine.

## 6) Other Remarks

Implementing multiple model concept in the form of  $Lp$ -norm prior with varying parameter  $p$  is similar to the source separation method reported in [66], where  $Lp$ -norm prior model is used to promote different source structures.

In the first set of real-data experiments, ECG data were collected from 120 leads and interpolated to 370 vertices for the inverse solution. In the second set of real-data experiments, ECG data collected from 120 leads were directly used for the inverse solution. We experimented with both types of inputs in our past work, and no substantial difference was observed. It might be because interpolation does not provide *extra* data but increases the redundant data (linearly dependent on the original 120-lead data). In addition, ECG data are usually involves noise and require pre-processing before being used for the EP imaging, such as detrending and denoising. Here, we used averaging over time to remove the noise. Beat-to-beat variability of the ECG signals was observed in our data and is a topic of our future study.

The anisotropy of the conductivity tensors reflects fiber structure that can be obtained experimentally or based on mapping techniques. The former is not yet readily available in in-vivo human subjects, while the latter has been commonly used in literature, such as in detailed ventricular modeling [67]. In this work, the latter approach is adopted where 3D fiber model is obtained by mapping a 3D experimentally-derived mathematical fiber model [28] to the personalized ventricular geometry of the subject. To obtain the exact conductivity values of a specific subject is a much more challenging problem and requires parameter estimation methods such as in [68]. Here literature value is adopted [69]. Both fiber mapping and conductivity values may introduce uncertainty/errors to the forward modeling, which in turn impact the solution of EP imaging. Assessing these

uncertainties is a challenging yet important question that need to be addressed in future work.

The overall CC obtained by multiple-model prior for imaging volumetric cardiac sources (on average 0.50) is lower than those reported in [15, 31, 70] (between 0.70 to 0.90). It is likely because of the use of transmural source models instead of surface-based source models. Furthermore, it might be caused by the type of transmural source models we used, *i.e.*, the gradient of action potential, which corresponds to complex and relatively compact structures such as propagation wavefront and infarct border. In our future work, we will use other error measures, such as relative difference measure (RDM) and magnification error norm (MAG), to further analyze our results.

Our proposed method only focuses on automatic adaptation of spatial prior model to the source spatial properties. Therefore, comparison with temporal-constraint based approaches such as those presented in [60, 71] was not considered. In our future work, we plan to integrate the proposed spatial multiple model approach with a temporal model of cardiac source propagation to guide the source evolution over time while automatically adapting to source spatial properties. Similar approach has been undertaken by our group in integrating a spatial sparsity model with a temporal source propagation model using hierarchical Bayes [72].

The infarct model used in this work is obtained based on the physiological properties of action potential during the ST segment of an ECG cycle, exhibiting low voltage amplitude at infarcted region and high voltage amplitude at viable tissues. The source model along the infarct border is obtained as the spatial gradient of action potential. Although this simplified infarct model provides different source structures for validating our method, it does not consider heterogeneous infarct regions. In our future work, we

will include infarct border zone in our simulation setting. It is noteworthy that the microscopic structure of infarct border zone is not yet well established and it is common practice in electrophysiological simulation to consider the parameter in the border zone to have intermediate values between that of the infarct core and healthy zones [73]. We will also consider extending the presented work to the imaging of ischemic regions utilizing previously reported cellular models of ischemia [74, 75].

In this work, we focused on source distributions with resolutions around 4-7 mm. In future work, we will study how the resolution of source distribution impacts the performance of multiple-model prior, the findings of which will enable us to optimize the computational cost of MCMC sampling by minimizing the number of sources (unknown parameters) to be estimated.

## 4.5 Conclusions

Noninvasive cardiac EP imaging involves solving an ill-posed problem, which is often regularized by imposing fixed prior models on the spatial distribution of sources. Although fixed-model techniques are able to accurately estimate specific source distributions, they may not always reflect the time-varying property of cardiac sources. In this work, we proposed a multiple-model hierarchical Bayesian approach for 3D source estimation to reduce model-data mismatch by incorporating a continuous combination of multiple models, contribution of which is inferred from the measurements. Experimental results demonstrated the necessity of different prior models for estimating complex source structures and the ability of the presented multiple-model approach to automatically adapt the model combination to measurement data in reflection of the source property.

## Chapter 5

# Impact of Prior Assumptions

## About Anatomical Modeling on

## Cardiac Electrophysiological

## Imaging

### 5.1 Background

Non-invasive cardiac electrophysiological (EP) imaging utilizes personalized anatomical models to establish the mathematical relationship between the cardiac electrical source  $\mathbf{v}$  and body-surface measurements  $\Phi$  ( $\Phi = \mathbf{H}\mathbf{v}$ ), where the constructed transfer matrix (volume conductor model)  $\mathbf{H}$  is specific to each subject's heart-torso geometry. The role of anatomical modeling in the accuracy of EP imaging has been previously studied. It was shown that using a generic instead of personalized anatomical model in EP imaging fails to accurately estimate cardiac electrical activity of individual subjects

[22]. Further studies also confirmed that certain *global* anatomical parameters, such as size, position and orientation of the heart with respect to electrode placement on the torso, must be subject-specific in order for non-invasive EP imaging to be accurate [21, 25]. Therefore, it has been a standard practice in current EP imaging systems to utilize a high-quality, anatomically-detailed heart-torso model generated from individual subjects' tomographic scans.

Personalized anatomically-detailed heart-torso model can be constructed either directly from patient's tomographic data or by customizing a template model to patient's anatomy [76]. However, taking either approach, construction of detailed anatomical models puts high demands on the quality of tomographic images needed. It also involves a time-consuming, expert-dependent image-analysis process, the complexity of which reduces the cost-effectiveness of the otherwise promising technique of EP imaging in clinical practice. Furthermore, it introduces model variations stemming from a variety of factors such as image quality, segmentation expertise, segmentation methods, and/or registration techniques. This in turn leads to unresolved uncertainties in the outcome of EP imaging systems that bring questions to their robustness in clinical practice.

In this study, we investigate the impact of the variation in detailed personalized anatomical modeling on EP imaging outcomes. This will help us understand and verify the robustness of current EP imaging systems to modeling variations inherent in these systems. Furthermore, it will shed light on the quality of anatomical models that is actually needed for reliable EP imaging, which in the long term will provide guidance for establishing a clinically practicable procedure of anatomical modeling for EP imaging. Considering the solution of the inverse EP problem  $\mathbf{y}$  as a function of input anatomical model  $\mathbf{x}$ ,  $\mathbf{y} = g(\mathbf{x})$ , where  $g$  represents the complex process of the inverse estimation of cardiac electrical activity, we approach our problem in two steps: 1) modeling the

probabilistic/statistical distribution of the input variable  $\mathbf{x}$ , the personalized anatomical models, and 2) quantifying the uncertainty of the outcome  $\mathbf{y}$  in relation to the uncertainty in input  $\mathbf{x}$ . In this study, we focus on the variation in modeling the ventricles of individual subjects.

To model the variations in input variable  $\mathbf{x}$ , we propose a novel application of statistical shape modeling (SSM) [77]. SSM provides a parametric shape model that captures the pattern of variability among a set of shapes. It is conventionally used to represent the shape variation among a *population* of subjects. However, in the context of EP imaging, the importance of subject-specific global anatomical parameters has been established [21, 25]. Therefore, in this study, the variation to be modeled is that of the personalized shapes, assuming that its global parameters have been correctly personalized to the individual's images. To do so, we build an SSM for each specific subject rather than a population of subjects. Training SSM over a set of *subject-specific* anatomical models derived from the same subject's anatomical images with different image quality, different inter-/intra-individual segmentation, or different segmentation methods, we derive a parametric description of the variation in personalized anatomical model in terms of their mean and variance.

To assess the sensitivity of the output variable  $\mathbf{y}$  to the uncertainties in input variable  $\mathbf{x}$ , there are two general groups of techniques: analytical vs. simulation-based approaches. Analytical approach is based on the differentiation of system equations with respect to the parameters of interest [78]. In our problem, the system  $g$  represents a complex process including the construction of personalized anatomical models, the calculation of transfer matrix  $\mathbf{H}$ , and the inverse estimation of cardiac electrical activity. Therefore, it cannot be explicitly formulated and analytically assessed.

Alternatively, simulation-based approaches provide sensitivity evaluation based on multiple simulations of the system  $g$  for different input values. The most well-known simulation-based approach is Monte Carlo (MC) analysis that generates a large number of random samples from the input parameter space. These samples are then propagated through the system to obtain the corresponding outputs, using which the statistics of the output variable can be calculated. However, given the large dimensionality of the input anatomical model  $\mathbf{x}$  (more than 1000 points), application of MC analysis to our problem will require a large number of simulations that is computationally expensive if not impossible.

Deterministic sampling is another class of simulation-based techniques that balances between the analytical and random sampling techniques. An example of such techniques is generalized polynomial chaos-stochastic collocation (gPC-SC) method that approximates the system function by a linear combination of orthogonal polynomials using collocation points (samples). These collocation points are derived with the aid of collocation methods originally used in numerical differentiation/integration [79]. This method was previously used to study the sensitivity of the forward electrocardiographic simulation to the position of the heart [25]. However, the number of required collocation points increases exponentially with the dimension of the input variable. Alternatively, unscented transform (UT) is a deterministic sampling method that preserves the system equation  $g(\mathbf{x})$  intact and approximates the distributions of input/output variables instead. Particularly, it uses optimization methods to find a *minimal* number of samples that can preserve the statistical moments of a given distribution up to a desired order [80]. Compared to SC, in the presence of a high-dimensional input variable  $\mathbf{x}$ , UT requires substantially less number of samples to accurately estimate statistics of output variable up to the second moment [81].

Therefore, we will apply the UT to the SSM, trained for each subject, to draw a set of samples from the statistical distribution of input personalized anatomical models. EP imaging will be carried out on each sample to obtain the corresponding outcome. The statistics of the EP imaging outcome will be calculated to study its uncertainty subject to anatomical modeling variations.

The feasibility of our approach in quantifying and assessing the impact of anatomical modeling variations on the EP imaging solution is demonstrated in two sets of phantom and real-data experiments. In these experiments, we employ two of the existing EP imaging methods as testbeds: epicardial-based electrocardiographic imaging (ECGI) [31] and transmural electrophysiological imaging (TEPI) [19].

## 5.2 Cardiac Electrophysiological Imaging

### 5.2.1 Surface-based EP Imaging Methods

As described in Chapter 2, surface-based EP imaging considers equivalent source models on the ventricular surface in forms of epicardial potential [31–33], or activation time [34–36]. These surface-based EP imaging methods often overcome the ill-posedness of the inverse problem by employing regularization with various constraints on spatial and/or temporal properties of the solution, such as Tikhonov regularization (zero-order, first-order, second-order) [14], truncated-SVD [12, 13], state-space filtering framework (Kalman filter) [6], and recently  $L_1$ -norm based sparsity models [15–17].

In this study, we consider epicardial-based electrocardiographic imaging (ECGI) technique, as presented in [31]. ECGI solves the inverse problem for the equivalent current source models located on the epicardium of the heart. Using boundary element method,

equations (2.4,2.6) can be numerically solved on a subject heart-torso model to obtain linear relationship between body-surface measurements  $\Phi$  and epicardial potential  $\mathbf{v}_e$ :  $\Phi = \mathbf{H}\mathbf{v}_e$ . ECGI then solves the inverse problem using zero-order Tikhonov regularization treating each time instant separately:

$$\hat{\mathbf{v}}_e = \arg \min_{\mathbf{v}_e} \|\Phi - \mathbf{H}\mathbf{v}_e\|^2 + \beta \|\mathbf{v}_e\|^2 \quad (5.1)$$

The first term in equation 5.1 provides the least square solution while the second term imposes constraint on the spatial smoothness of the solution. The regularization parameter  $\beta$  controls the relative weight of two terms. For details of the ECGI algorithm, please refer to [31].

### 5.2.2 Transmural EP Imaging Methods

In the past decade, transmural EP imaging has been emerged that considers transmural source models in forms of transmural action potential [19, 20, 37–39], or current density / activation wavefront [40, 41]. These volumetric approaches often overcome the ill-posedness of the inverse problem by imposing different orders of smoothness constraints on the spatial or temporal properties of the solution, through methods such as Laplacian weighted minimum norm [37], or lead-field normalized weighted minimum norm (LFN-WMN) in combination with truncated-SVD [41] and/or incorporating physiological models of cardiac excitation wavefront propagation [19, 20, 39].

In this study, we consider transmural electrophysiological imaging (TEPI) method, as presented in [19]. TEPI solves the inverse problem for the transmural action potential within the myocardium. Using a proper combination of numerical methods, such as

mesh-free and boundary element methods [19, 82], one can numerically solve equations (2.3-2.6) on a subject heart-torso model, and obtain linear relationship between body-surface measurements  $\Phi$  and transmural action potential  $\mathbf{u}$ :  $\Phi = \tilde{\mathbf{H}}\mathbf{u}$ . For detailed specification of the heart-torso models and calculation of the forward problem using mesh-free and boundary element methods, please refer to [82].

TEPI combines a physiological spatiotemporal prior of action potential with body-surface potential data through Bayesian statistical regularization to overcome the ill-posedness of the problem. Assuming action potential  $\mathbf{u}$  and body-surface potential  $\Phi$  as random variables, TEPI seeks the *maximum a posteriori* (MAP) estimate of  $\mathbf{u}_k$  at time instant  $k$  that maximizes the posterior density function of  $\mathbf{u}_k$  given all body-surface measurements  $,\Phi_{1:k}$ , up to the time instant  $k$ , where  $k = 1, \dots, t$  and  $t$  is the total number of measurements over time.

$$\hat{\mathbf{u}}_k = \arg \max_{\mathbf{u}_k} \{f(\mathbf{u}_k | \Phi_{1:k})\} \quad (5.2)$$

At each time step  $k$ , a prediction of the distribution of  $\mathbf{u}_k$  is first obtained by a probabilistic simulation of a macroscopic Aliev-Panfilov model [59] based on its estimation from the previous iteration  $\mathbf{u}_{k-1}$ . An MAP estimation of  $\mathbf{u}_k$  is then calculated using the predicted prior and the likelihood according to the Bayes rules. For details of TEPI, please refer to [19].

### 5.3 Sensitivity Assessment of EP Imaging to Variations in Personalized Ventricular Shapes

Anatomical modeling involves variations and uncertainties that are caused by different factors such as different segmentation techniques, inter-/intra-individual difference in segmentation, and image quality. As an example, Fig. 5.1 presents two different segmentation results (red and blue contours) of one cardiac MRI slice at the short axis view performed by two experts. The visible difference in local details of endocardium and epicardium contours would eventually lead to two different heart models built for the same subject. In contrast with global anatomical parameters (heart size, position and orientation) whose importance on EP imaging is well established, the influence of these local shape variations on the accuracy of EP imaging has not been investigated or well understood.

To determine the sensitivity of the EP imaging outcome  $\mathbf{y}$  to the local anatomical modeling variations  $\mathbf{x}$ , we formulate the problem as  $\mathbf{y} = g(\mathbf{x})$ , where  $\mathbf{x}$  contains the 3D coordinates of all surface nodes,  $\mathbf{y}$  is the corresponding EP imaging outcome, and  $g$  represents a complex process including the construction of personalized anatomical models, the calculation of transfer matrix  $\mathbf{H}$ , and the inverse estimation of cardiac electrical activity. As summarized in Fig. 5.2, first, we will model the statistical distribution

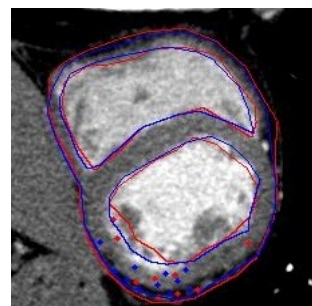


FIGURE 5.1: Two different segmentations (red and blue contours) of one MRI slice at the short axis view.

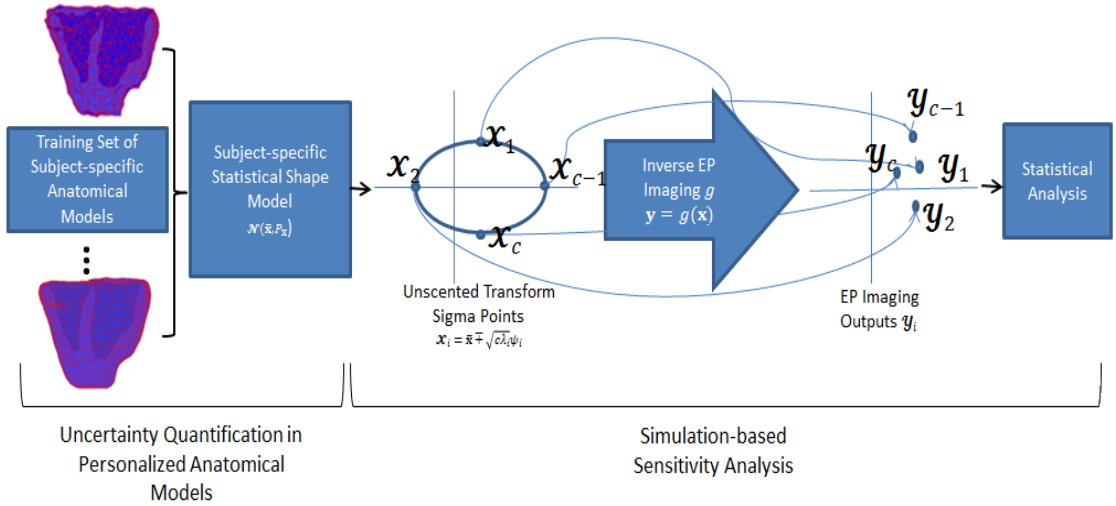


FIGURE 5.2: Outline of the proposed approach to investigate the uncertainty of EP imaging subject to variations in personalized anatomical models.

accounting for variations in personalized anatomical modeling. Second, we will quantify the output uncertainty resulting from the input variation. Detailed descriptions of these two steps are provided in the following sections.

### 5.3.1 Uncertainty Quantification in Personalized Anatomical Models

As a first step, we need to quantify the variations/uncertainties in personalized anatomical models. Because of the importance of *subject-specific* global anatomical parameters (heart size, position, and orientation with respect to torso) on the accuracy of EP imaging [21, 25], we train a *personalized* SSM for each subject on a set of anatomical models that have identical global parameters correctly customized to the subject. This set of training models will include shape variations resulted from two major causes: different image resolution and inter-individual difference in segmentation. For the former, cardiac MR/CT images of each subject are downsampled to generate different image resolutions. For the latter, different experts are recruited to perform manual segmentations for each subject's images. These segmentation results by different users on images with different

resolutions provide the basis for constructing the training set of anatomical models to build the subject-specific SSM.

For each segmentation result, a surface mesh of the heart will be built with nodal positions represented in Cartesian coordinates  $(x_i, y_i, z_i \ i = 1, 2, \dots, n)$ . For each subject, all surface meshes in the training set have the same number of nodes with known correspondence. Concatenating the coordinates of all  $n$  nodes to one vector, each surface mesh (anatomical model) can be described as  $\mathbf{x} = (x_1, y_1, z_1, \dots, x_n, y_n, z_n)^T$ . It must be noted that, as mentioned earlier, the training anatomical models for each subject are aligned and share identical global anatomical parameters tailored to that subject.

Constructing the statistical shape model consists of two steps: 1) extracting the mean shape, 2) calculating the covariance matrix of the training shapes [77]. The mean shape  $\bar{\mathbf{x}}$  is calculated by averaging over all training samples as:

$$\bar{\mathbf{x}} = \frac{1}{s} \sum_{i=1}^s \mathbf{x}_i \quad (5.3)$$

The covariance matrix  $\mathbf{P}_{\mathbf{x}}$  of the training samples is calculated as:

$$\mathbf{P}_{\mathbf{x}} = \frac{1}{s-1} \sum_{i=1}^s (\mathbf{x}_i - \bar{\mathbf{x}})(\mathbf{x}_i - \bar{\mathbf{x}})^T \quad (5.4)$$

The variation of personalized anatomical models for a specific subject is thus modeled as a high-dimensional Gaussian random variable with mean  $\bar{\mathbf{x}}$  and covariance  $\mathbf{P}_{\mathbf{x}}$ :  $\mathcal{N}(\bar{\mathbf{x}}, \mathbf{P}_{\mathbf{x}})$ .

### 5.3.2 Simulation-Based Sensitivity Evaluation

Given the statistical description of personalized anatomical modeling, we are interested in quantifying the resulting statistical distribution of the EP imaging output. As described earlier, the complex relationship  $g$  between EP imaging output  $\mathbf{y}$  and the input anatomical model  $\mathbf{x}$  cannot be analytically formulated. Therefore, simulation-based techniques should be used to obtain output statistics based on multiple simulations of  $\mathbf{y} = g(\mathbf{x})$  using samples drawn from the input distribution  $\mathbf{x}$ . Because of the high-dimensionality of  $\mathbf{x}$ , we employ the unscented transform (UT) to reduce the number of samples and accordingly the number of EP imaging processes needed to be carried out.

UT is established based on the principle that, given a nonlinear function  $\mathbf{y} = g(\mathbf{x})$ , *it is easier to approximate a probability distribution than it is to approximate an arbitrary nonlinear function* [80]. Accordingly, a set of weighted points (sigma points),  $S = \{i = 1, 2, \dots, p : \mathcal{X}_i, \mathcal{W}_i\}$ , is selected deterministically so as to minimize the error in approximating the statistical moments of  $\mathbf{x}$  up to a desired order. Applying the nonlinear function  $g$  to each point yields a set of transformed points, statistics of which gives an estimate of the output statistics that otherwise could not be derived analytically.

Given the Gaussian shape model  $\mathcal{N}(\bar{\mathbf{x}}, \mathbf{P}_{\mathbf{x}})$ , derived in the previous section, different sets of sigma points can be used to capture the output statistics up to the second order. An example that we employed in our study is a set of  $2L$  sigma points (samples) symmetrically-distributed around the mean along the direction of second-order variation:

$$\begin{aligned}\mathcal{X}_i &= \bar{\mathbf{x}} + (\sqrt{L\mathbf{P}_{\mathbf{x}}})_i, \mathcal{W}_i = 1/2L, i = 1, \dots, L \\ \mathcal{X}_{i+L} &= \bar{\mathbf{x}} - (\sqrt{L\mathbf{P}_{\mathbf{x}}})_i, \mathcal{W}_{i+L} = 1/2L, i = 1, \dots, L\end{aligned}\tag{5.5}$$

where  $L$  represents dimension of the input variable  $\mathbf{x}$  ( $3n$  in this case,  $n$  being the number of nodes in the shape model) and  $(\sqrt{L\mathbf{P}_x})_i$  denotes the  $i$ th row or column of the matrix  $\sqrt{L\mathbf{P}_x}$ .  $\mathcal{W}_i$  is the weight assigned to the  $i$ th sigma point.

Because  $L = 3n$  is large in our study ( $n$  is at the order of  $10^3$ ),  $2L$  sigma points still requires a large amount of EP imaging processes. To further reduce the number of sigma points needed, we propose to sample the sigma points only along the predominant (instead of all) directions of variance in  $\mathbf{x}$ . To extract the principal directions of variance in  $\mathbf{x}$ , principle component analysis (PCA) is applied to  $\mathbf{P}_x$  to decompose the covariance matrix into the principle modes of variations  $\Psi$  (eigenvectors) and the corresponding value of variances  $\lambda$  (eigenvalue).

$$\sqrt{\mathbf{P}_x} = \sqrt{\lambda}\Psi \quad (5.6)$$

The modes of variations are sorted in an order with descending variances such that  $\lambda_1 \geq \lambda_2 \geq \dots \geq \lambda_{3n}$ . Therefore, the covariance matrix  $\mathbf{P}_x$  can be approximated by the  $c$  highest modes of variations as

$$\sqrt{\tilde{\mathbf{P}}_x} \approx [\sqrt{\lambda_1}\psi_1; \sqrt{\lambda_2}\psi_2; \dots; \sqrt{\lambda_c}\psi_c] \quad (5.7)$$

Replacing the full size covariance matrix  $\mathbf{P}_x$  with the reduced covariance matrix  $\tilde{\mathbf{P}}_x$  in equation (5.5), we can reduce the number of required sigma points to  $2c$  as:

$$\begin{aligned} \mathcal{X}_i &= \bar{\mathbf{x}} + \sqrt{c\lambda_i}\psi_i, \mathcal{W}_i = 1/2c \quad i = 1, \dots, c \\ \mathcal{X}_{i+c} &= \bar{\mathbf{x}} - \sqrt{c\lambda_i}\psi_i, \mathcal{W}_{i+c} = 1/2c \quad i = 1, \dots, c \end{aligned} \quad (5.8)$$

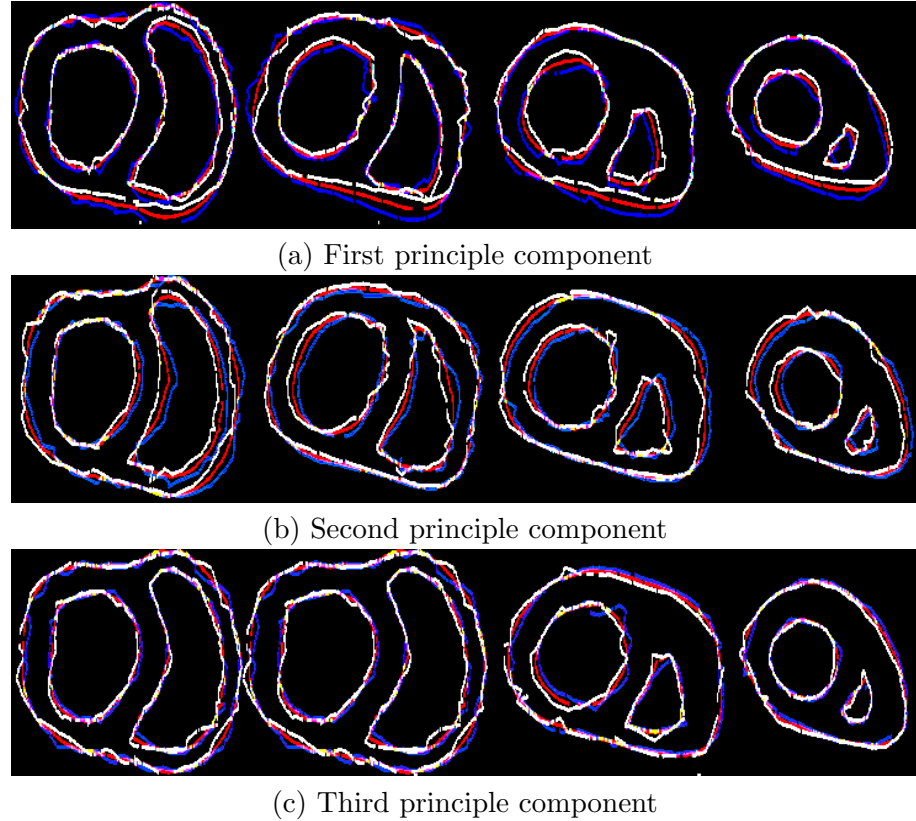


FIGURE 5.3: Examples of anatomical variations around mean geometry model along (a) first, (b) second, and (c) third principle directions. Mean geometry model is shown in red color while the two sample geometry models are shown in white and blue.

To guarantee plausible shapes,  $\sqrt{c}$  should be restrained to a certain interval. A common approach is to limit  $\sqrt{c}$  to lie within  $[-3, +3]$ , treating all modes as independent distributions [77]. This is approximately equivalent to taking the first 10 eigenvectors ( $c = 10$ ) in sampling the sigma points, which accounts for 98% of the total variation ( $\sum_{i=1}^L \lambda_i$ ). As an example, Fig. 5.3 presents anatomical variations around mean geometry  $\bar{\mathbf{x}}$  (shown in red color) along the (a) first, (b) second, and (c) third principle directions (white and blue contours show  $-3\sqrt{\lambda_i}$  and  $+3\sqrt{\lambda_i}$   $i \in \{1, 2, 3\}$ , respectively).

Each sigma point represents a personalized anatomical model following the statistical distribution modeled for a specific subject using his or her SSM.

### 5.3.3 Statistical Analysis

For each subject, on each anatomical model  $\mathcal{X}_i$  sampled from his/her personalized SSM, EP imaging can be carried out using identical BSP data acquired for that specific subject:

$$\mathcal{Y}_i = g(\mathcal{X}_i) \quad (5.9)$$

According to the UT theory, the first two moments of the output distribution can be estimated as

$$\bar{\mathbf{y}} = \sum_{i=0}^{2c} \mathcal{W}_i \mathcal{Y}_i \quad (5.10)$$

$$\mathbf{P}_{\mathbf{y}} = \sum_{i=0}^{2c} \mathcal{W}_i (\mathcal{Y}_i - \bar{\mathbf{y}})^2 \quad (5.11)$$

In this way, the mean and variance of EP imaging output (5.10, 5.11) are calculated, which provide information about the distribution/uncertainty of the EP imaging solutions.

In addition, pooled from results across multiple subjects, we conduct a statistical test of equivalence to investigate the statistical equivalency of the EP imaging outputs  $\mathcal{Y}_i$  obtained on different anatomical models  $\mathcal{X}_i$  drawn from subject-specific SSM models. To do so, a specific accuracy measure  $\theta$  (explained in section 5.4) is extracted from the EP imaging outputs.  $\theta$ s obtained on the same subject yet with different anatomical models (drawn from the SSM) are randomly paired up and the difference of each pair ( $d\theta$ ) is calculated. The hypothesis test of equivalence based on paired t-test is then performed

on the  $d\theta$ s of multiple subjects. Assuming parameter  $d\theta \sim \mathcal{N}(\delta, \sigma^2)$  to be the measure of the intra-subject difference of the paired observations of  $\theta$ s, statistical equivalency is obtained if  $\delta/\sigma$  lies within an established range  $[-\varepsilon, \varepsilon]$ ,  $\varepsilon > 0$  [83]. The alternative and null hypotheses are defined as:

$$\text{Alternative hypothesis } (H_1) : -\varepsilon \leq \delta/\sigma \leq \varepsilon$$

$$\text{Null hypothesis } (H_0) : \delta/\sigma < -\varepsilon \text{ or } \delta/\sigma > \varepsilon$$

## 5.4 Experiments and Results

As mentioned before, we consider two EP imaging approach (ECGI and TEPI, described in section 5.2) as testbeds for our experiments. The solution of ECGI is in the form of epicardial potential dynamics while the TEPI solution is in the form of transmural action potential dynamics. We conduct two sets of synthetic and real-data experiments.

### 5.4.1 Synthetic Experiments

Synthetic experiments are conducted on four subjects including one canine heart and three human hearts. A realistic human torso model with 370 vertices on the triangulated body surface is coupled with all the heart models to set up the phantom experiments [84]. For each subject, MR/CT images are down-sampled to generate 3 sets of images with different resolutions. A set of 7 ventricular models are developed using manual segmentation of MR/CT images with specific resolution performed by different experts (total 21 segmentations for each subject). This set serves the training set for constructing subject-specific SSM. From each subject-specific SSM, 20 ventricular models are generated using the 10 highest eigen values of the covariance matrix. Body surface potential

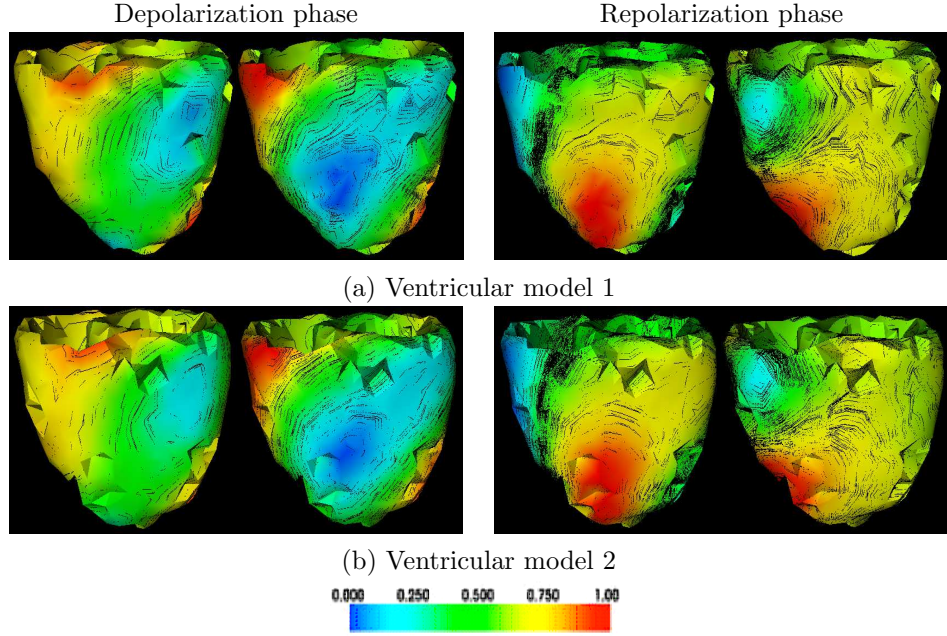


FIGURE 5.4: ECGI solution (epicardial potential) obtained on two ventricular models for the same subject in the healthy setting, at two different time instants of cardiac depolarization and repolarization phases.

(BSP) data, including 370 electrodes located on the vertices of the torso surface mesh, are simulated on the mean shape provided by the trained SSM for each subject and are corrupted with 20-dB white Gaussian noise. For each subject, the identical BSP data are coupled with the SSM-sampled ventricular models for EP imaging to ensure that the only factor affecting EP imaging outputs is the variation in the input ventricular shape.

In the synthetic experiments the ground truth is available in form of epicardial/action potential dynamics. Therefore, quantitative accuracy of the solution is evaluated in terms of average relative error (RE) and average correlation coefficients (CC) between estimated and true potentials over a cardiac cycle [31].

Experiments are conducted on both healthy and post-infarction settings; for the latter, the infarct region extends from basal to mid-anteroseptal and inferoseptal in each subject's ventricle.

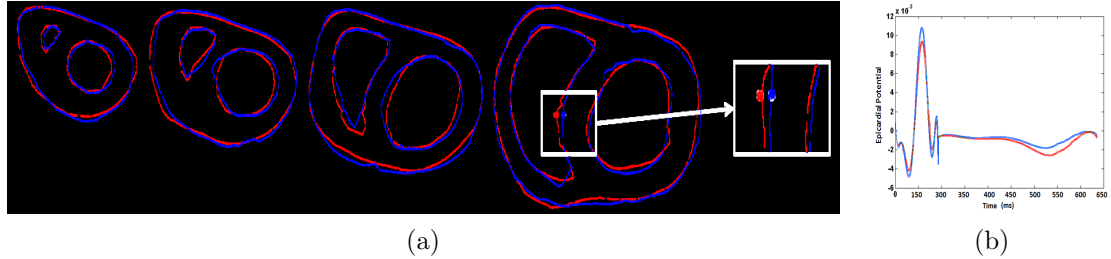


FIGURE 5.5: (a) Overlap of two ventricular models of one subject, shown in Fig. 5.4, in short-axis view from base to apex. (b) ECGI solution at two corresponding nodes on the two ventricular models in healthy setting.

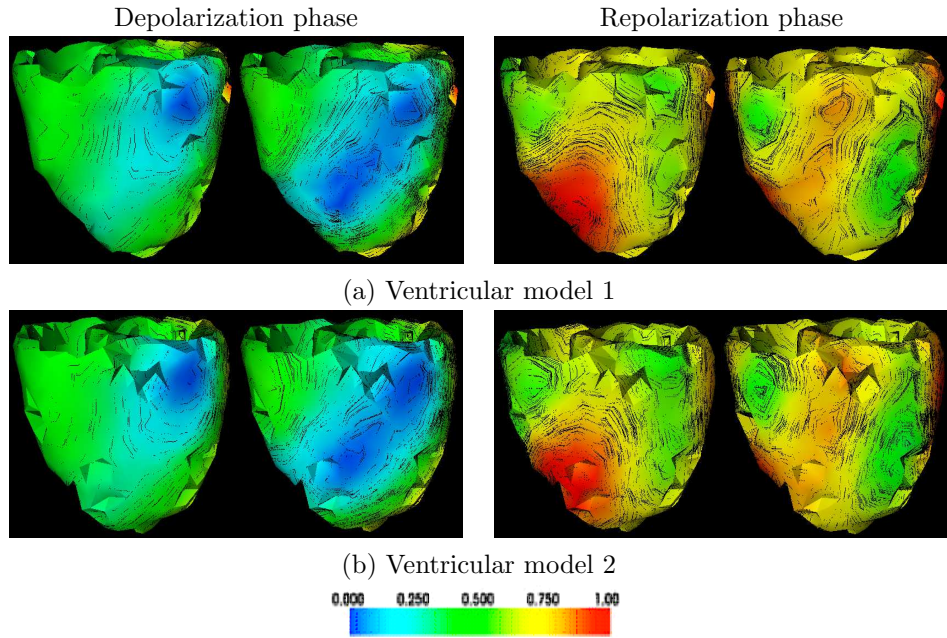


FIGURE 5.6: ECGI solution (epicardial potential) obtained on two ventricular models for the same subject in the post-infarction setting, at two different time instants of cardiac depolarization and repolarization phases.

**ECGI Results.** Fig. 5.4 gives an example of the epicardial potential reconstructed on two ventricular models for the same subject in the healthy setting at two time instants during depolarization and repolarization stages. Variation in two personalized anatomical models is also shown in short-axis views in Fig. 5.5a. Despite visible difference in anatomical details, similar epicardial potential patterns can be observed for two anatomical models during the cardiac cycle. Estimated epicardial potential dynamics for two corresponding nodes on the surface meshes of two ventricular models in the healthy setting are also very similar (Fig. 5.5b). An example of epicardial potential

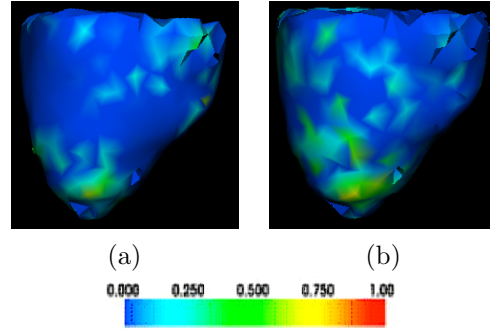


FIGURE 5.7: STD map of ECGI output on a mean anatomical model during ST segment of an ECG cycle for (a) healthy, and (b) post-infarction settings.

reconstruction for the same anatomical models in the post-infarction setting is shown in Fig. 5.6. Likewise, potential dynamics are consistent for the two ventricular models during depolarization and repolarization, indicating that variation in shape details does not have significant impact on the EP imaging solution.

The mean and variance of the ECGI outputs on a mean anatomical model are calculated according to equations (5.10, 5.11). Standard deviation (STD) map of ECGI outputs for healthy and post-infarction settings during the ST segment of an ECG cycle is presented in Fig. 5.7. STD ranges from  $2.63e - 9$  to  $1.4e - 4$  in the healthy setting while in the post-infarction setting the STD range ( $6.43e - 8, 0.007$ ) is higher. Low STD in both settings indicates robustness of ECGI outcomes to the variations in personalized anatomical models.

On ECGI outputs obtained on the 80 ventricular models for the four subjects, error measures RE and CC for the same subject are randomly paired up (40 pairs for the paired t-test) and RE difference and CC difference are calculated for each pair. Paired results of the four subjects have RE difference ( $d\theta$ ) with mean 0.03 and variance 0.19. Assuming the commonly used equivalence limits  $\varepsilon = 0.5$  [83], with 40 number of pairs,  $d\theta$  resides in the rejection region at  $\alpha$  level = 5%. The CC difference for the paired

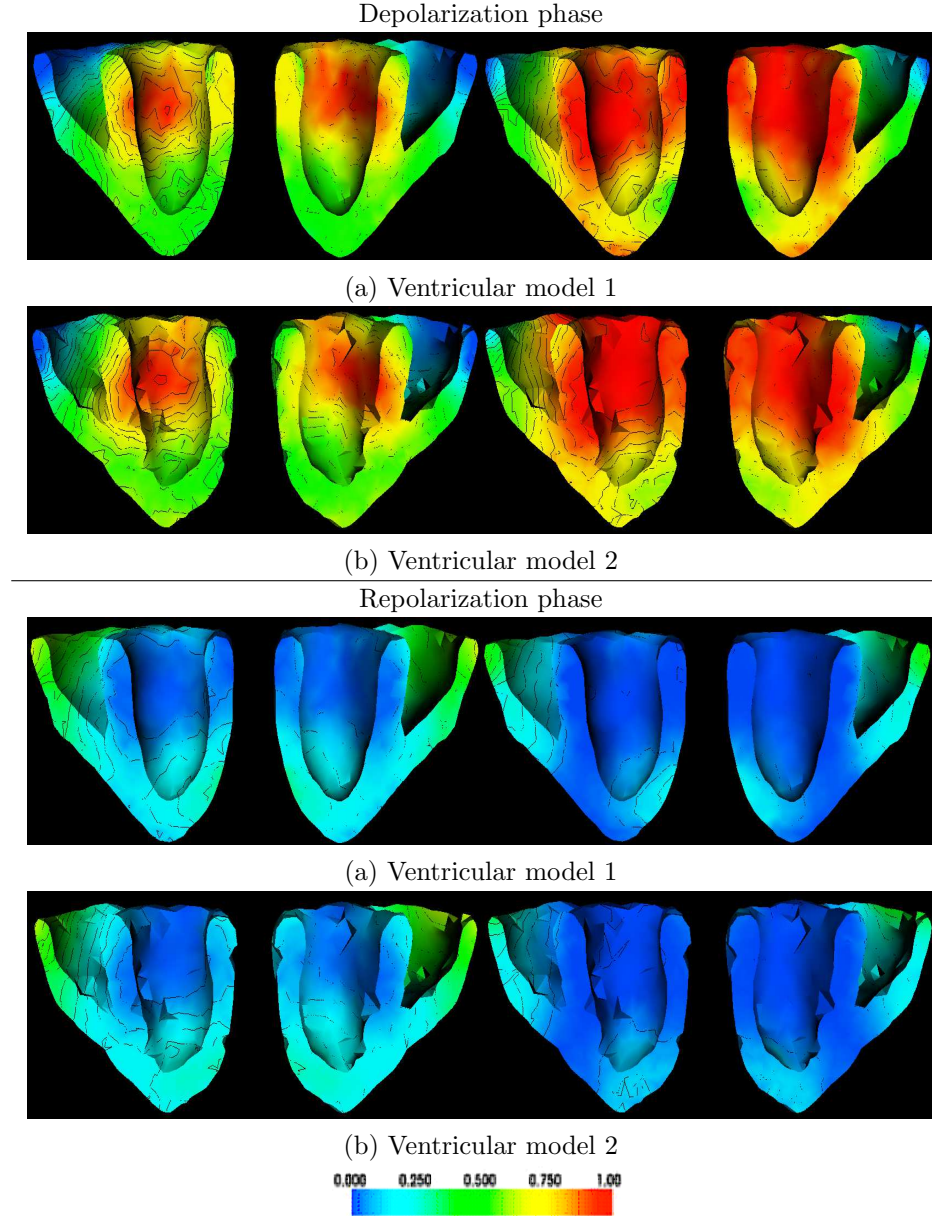


FIGURE 5.8: TEPI solution (transmural action potential) obtained on two ventricular models for the same subject in the healthy setting, at two different time instants of cardiac depolarization and repolarization phases. Color encodes the value of action potential.

population has normal distribution  $\mathcal{N}(0.04, 0.032)$ , also reporting the rejection of null hypothesis for the tolerance  $\varepsilon = 0.5$  at  $\alpha = 0.05$ .

**TEPI Results.** Fig. 5.8 presents four snapshots of transmural action potential estimation on two ventricular models of one subject in the healthy setting during depolarization and recovery stages. Transmural action potential propagates similarly through two

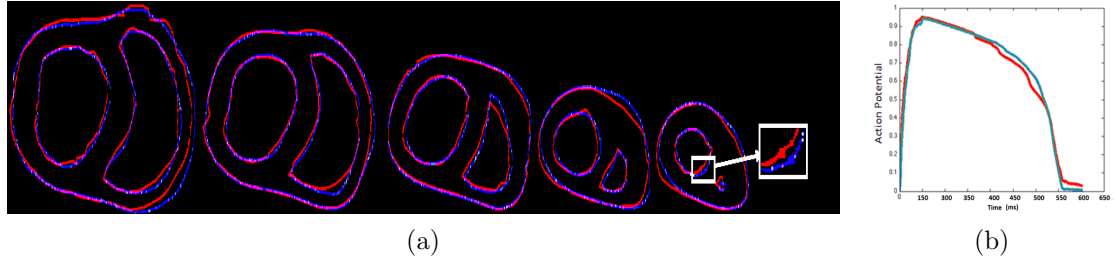


FIGURE 5.9: (a) Overlap of two ventricular models of one subject, shown in Fig. 5.8, in short-axis view from base to apex. (b) TEPI solution at two corresponding nodes on the two ventricular models in healthy setting.

models during cardiac cycle despite visible anatomical detail differences (shown in Fig. 5.9a). Estimated transmural action potential dynamics for two corresponding nodes on the two ventricular models during one cardiac cycle are presented in Fig. 5.9b. It can be seen that slight difference in the position of the corresponding nodes does not affect the estimated action potential dynamics. Fig. 5.10 shows snapshots of transmural action potentials obtained on two ventricular models of the same subject in the post-infarction setting, where late activation (left) and early repolarization (right) at infarct region are similar in two anatomical models.

Similarly, mean and variance of TEPI outputs are determined (equations 5.10, 5.11). STD map of TEPI outputs on a mean anatomical model during the ST segment of an ECG cycle for both healthy and post-infarction settings are shown in Fig. 5.11. TEPI output STD ranges between  $8.25e - 6$  to 0.03 for different ventricular models during a cardiac cycle in healthy setting. In post-infarction settings, STD range increases ( $9.25e - 6, 0.05$ ) compared to healthy setting. The small range of variation in TEPI output in both settings confirms its low sensitivity to the variations in input anatomical models.

Likewise, TEPI outputs on the entire population are collected and its errors in RE and CC on ventricular models for the same subject are randomly paired up (40 pairs in total for the four subjects). The difference of RE ( $d\theta$ ) for the paired results of all 4 subjects

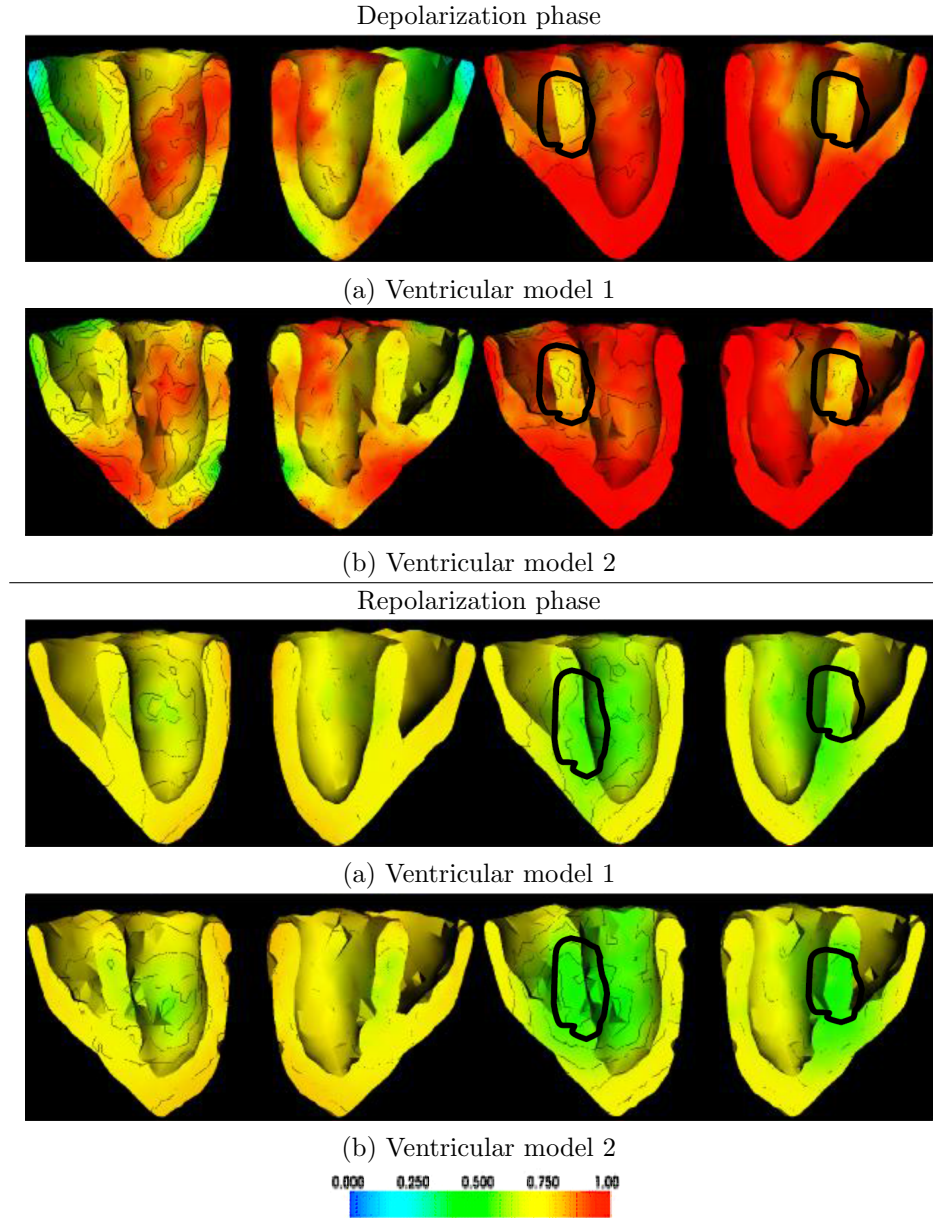


FIGURE 5.10: TEPI solution (transmural action potential) obtained on two ventricular models for the same subject in the post-infarction setting, at two different time instants of cardiac depolarization and repolarization phases. Color encodes the value of action potential.

has mean 0.01 and variance 0.03 that belongs to the rejection region at  $\alpha = 0.05$ , choosing equivalence limits to be  $\pm \varepsilon$  for  $\varepsilon = 0.5$  and a number of 40. The null hypothesis is thus rejected and the alternative hypothesis can be accepted. Similarly, the difference of CC for the paired population has a normal distribution  $\mathcal{N}(0.02, 0.016)$  that reports the rejection of the null hypothesis for the tolerance  $\varepsilon = 0.5$  at  $\alpha = 0.05$ . Therefore, in our

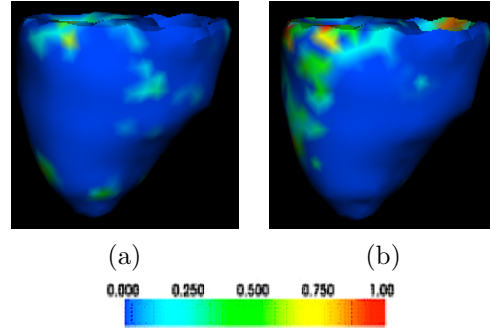


FIGURE 5.11: STD map of TEPI output on a mean anatomical model during ST segment of an ECG cycle for (a) healthy, and (b) post-infarction settings.

phantom experiments, the null hypothesis is successfully rejected, and we can conclude that local variations in personalized ventricular models do not affect the accuracy of either EP imaging methods being considered. In another word, variations in the shape level do not impact the accuracy of EP imaging systems.

#### 5.4.2 Real-Data Experiments

Real-data experiments are performed on four post-infarction human subjects [85]. The datasets include end-diastolic MR images of heart/torso geometries and 123-lead body-surface potential (BSP) recordings for each subject, described in detail in Chapter 3, section 4.2.

Similar to the phantom experiments, 7 ventricular models are built for each subject based on manual segmentations of 3 different images resolutions by different experts in order to create the SSM training set (in total 21 segmentations for each subject). Using trained SSM for each subject, 16 ventricular models are generated, giving 64 heart models in total among the four subjects. For each subject, 16 ventricular models are coupled with identical measured BSP data as inputs to the two EP imaging methods under study.

In real-data experiments, because the ground truth of epicardial/action potential dynamics (*e.g.*, intracardiac electrogram recording) is not available, infarct quantification is used to assess the solution accuracy. Infarct region can be identified based on the characteristic features of the estimated potential dynamics. In this study, we extract two most representative features of the infarct region: activation time (AT) and action potential duration (APD) which is defined as the difference between AT and repolarization time (RT). In ECGI, late activation time is used as a main characteristic of the infarct region. AT is set at the maximum negative derivative of the QRS segment of epicardial potential trace [86]. In TEPI, regions associated with late activation time and/or short action potential duration are identified as infarct regions [60]. AT is set at the maximum first derivative of action potential upstroke and RT is set at the maximum second derivative of action potential downstroke [87]. Infarct region is finally quantified in terms of infarct size and center that are calculated based on the 17 segments of the left ventricle (LV) [49]. Infarct size (IS) describes the ratio of estimated infarcted segments to the total number of segments. Infarct center (IC) represents the center of the infarct scar segments.

**ECGI Results.** Fig. 5.12a shows ECGI solutions for two ventricular models of case 3 and case 4 during depolarization. For each subject, despite the visible difference in anatomical details of the two ventricular models, similar potential dynamics can be observed. Infarct regions detected by ECGI methods for two ventricular models of the same subject are also identical, as highlighted with black contour with good match with the ground truth. Detected infarct region for case 1 corresponds to segments 1, 3, 4, 7, 9, 10, 13 and 15 with center located at segment 9. In case 2, segments 4, 5, 9, 10, 11 are associated with infarct region (center at segment 10). In case 3, detected infarct region is centered at segment 12 and extends to segments 3, 4, 5, 11 and 16. In case 4 the infarct

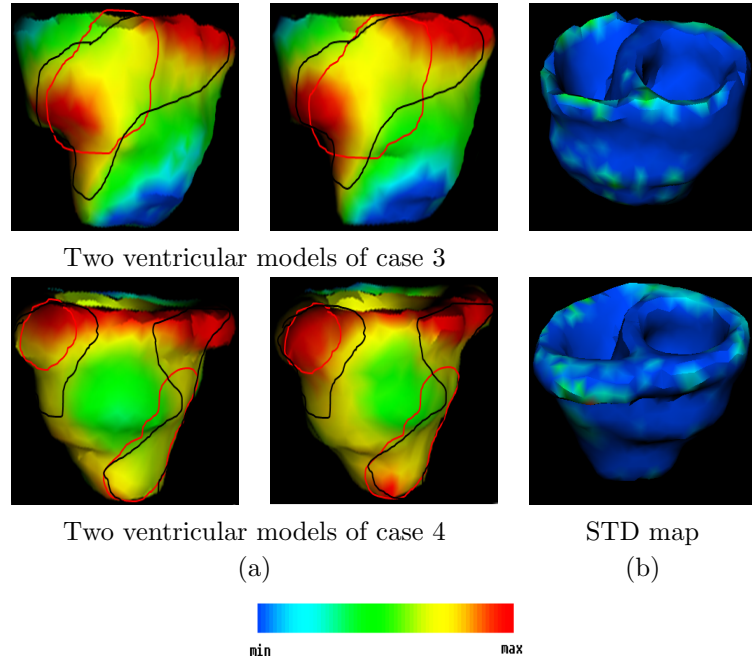


FIGURE 5.12: (a) ECGI solution for two ventricular models constructed for case 3 and case 4 during depolarization. Black and red contours show the ECGI estimated and the reference infarct region, respectively. (b) STD map of ECGI output on a mean anatomical model for case 3 and case 4 at the corresponding time instants. Color encodes the value of potential magnitude.

region is detected to be at segments 1, 3, 4, 5, 7, 10, 15, and 17 with center at segment 15. The STD map of ECGI solution for these two cases at the corresponding time instants are also shown in Fig. 5.12b. The low peak value on the STD map ( $0.004 \text{ mV}$ ) indicates robustness of the ECGI solutions to the variations in personalized anatomical modeling.

A hypothesis test of equivalence is conducted on randomly paired ECGI outputs of the same subject (32 pairs in total for four subjects) using IS and IC as accuracy measures. IS difference and IC difference for paired ECGI observations have normal distribution  $\mathcal{N}(0.1, 0.17)$  and  $\mathcal{N}(0.6, 1.17)$ , respectively, that falls within the rejection region of the null hypothesis. In another word, the alternative hypothesis is accepted meaning that variations in shape level have negligible impact on accuracy of ECGI output.

**TEPI Results.** Fig. 5.13a presents TEPI solutions for two ventricular models of case 3

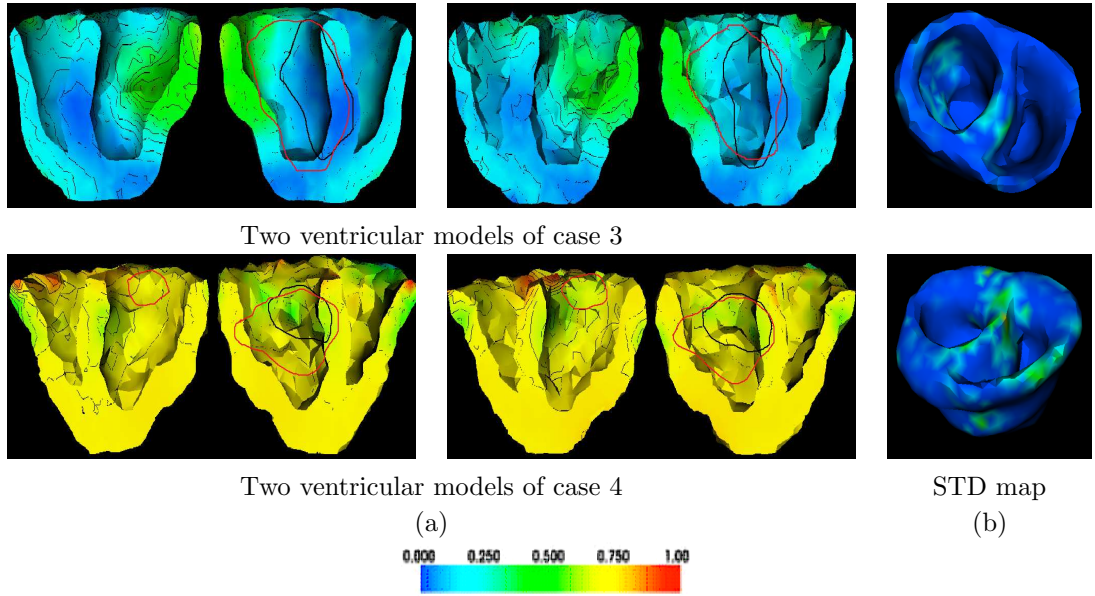


FIGURE 5.13: (a) TEPI solution for two ventricular models constructed for case 3 and case 4. Black and red contours show the TEPI estimated and the reference infarct region, respectively. (b) STD map of TEPI output on a mean anatomical model for case 3 and case 4 at the corresponding time instants. Color encodes the value of potential magnitude.

and case 4. Despite variations in anatomical details, similar potential dynamics can be observed on two anatomical models of the same subject. The infarct regions detected for the two anatomical models (highlighted with black contours) are consistent and match the ground truth (red contour) as well. In case 1, the detected infarct region (segments 1, 2, 7, 8, 9, 13, 14, and 15) centers at segment 8. The infarct region in case 2 extends to segments 2, 3, 8, 9, 14, and 15 with center 9. In case 3, segments 3, 4, 9, 10, and 15 are detected to be associated with infarct (center at segment 10). In case 4, infarct region is estimated to be at segments 9, 10, 11, and 15 (center at 15). The STD maps of TEPI solution for these two cases during repolarization are also shown in Fig. 5.13b. Maximum STD corresponds to low value of  $0.001 \text{ mV}$  that shows the low sensitivity of TEPI method to the variations in anatomical modeling.

TEPI outputs on ventricular models for the same subject are randomly paired up, and hypothesis tests of equivalence are performed on the 32 pairs for the 4 subjects. IS

difference and IC difference of paired observations for TEPI outputs have normal distribution  $\mathcal{N}(0.01, 0.06)$  and  $\mathcal{N}(0.4, 1.8)$ , respectively. For a sample of 32 pairs and the equivalence limit  $\varepsilon = 0.5$ , it reports the rejection of null hypothesis and acceptance of alternative hypothesis at 5% level. Therefore, the real-data experiments results confirm the findings of synthetic experiments.

## 5.5 Discussions

### 1) Validation against Intracardiac EP Data

In this study, the findings are limited to healthy and post-infarction settings. Furthermore, in real-data post-infarction setting, EP imaging methods are only validated against *gold standard* in terms of 17 segments of AHA standard due to the challenge of obtaining intracardiac validation data in humans. To date, transmural EP imaging validation against intracardiac measurements is only reported in animal studies [? ? ]. In future work, more analysis will be conducted on real cases with intracardiac EP measurements as *gold standard* to obtain sensitivity study in terms of RE and CC. The sensitivity of EP imaging methods to personalized anatomical models variations in other cardiac pathologies remains to be studied.

### 2) Impact of Heart Motion

It is a common practice in cardiac EP imaging to use a static heart model due to model complexity, computational cost, and more importantly, the challenge to acquire temporally-aligned body surface mapping and tomographic imaging data. However,

neglecting heart motion in cardiac EP imaging will affect the solutions. In the depolarization stage, this effect can be assumed to be minimal because, as a result of the delay between electrical activation and mechanical contraction, the depolarization of the ventricles can be expected to be close to completion before the heart starts to contract. The repolarization of the ventricles, however, will be accompanied by the deformation of the heart and it remains unclear how the neglect of this deformation would affect EP imaging. Because the current study focuses on the effect of shape variations instead of heart motion on cardiac EP imaging, we follow the common practice in the field to adopt a static heart model to isolate the factors of interest (shape variations).

### **3) Impact of Fiber Architecture**

In this study, fiber structures on sample ventricular models are obtained by mapping a detailed, experimentally-derived mathematical model [28] to the patient-specific geometry of our ventricular models. The 3D fiber architecture is fixed for each patient among the multiple ventricular models with shape variations, again to isolate the factor of shape variation and its effect on cardiac EP imaging. It therefore does not affect the observations of our sensitivity study.

### **4) Other Remarks**

Using PCA is based on the assumption that all the variables have linear relationships. This study considers a small range of variations in anatomical models, where PCA assumptions apply. Including a wider range of anatomical variations, such as respiration or heart motion, may contradicts the linearity assumption of PCA, requiring more appropriate techniques for dimension reduction.

## 5.6 Conclusions

Cardiac EP imaging focuses on non-invasive and mathematical reconstruction of cardiac electrical activity using body-surface measurements data. Its diagnostic potential in current practice of clinical EP study for different cardiac pathologies has been reported [15, 33, 88–90]. To move toward future clinical translation, several components within current EP imaging systems remain to be examined regarding both their clinical practicability and their influence on the robustness of these systems. One such component is personalized anatomically-detailed ventricular modeling, preparation of which involves inevitable variations and uncertainties that may impact reliability of EP imaging outcome. While global anatomical parameters (heart size, position and orientation) have been reported to be important, shape variation caused by personalized anatomical modeling errors has not been investigated.

In this work, for the first time, we investigated how modeling errors introduced during subject-specific modeling affect accuracy of EP imaging outcome, when global anatomical parameters are correctly captured. Our statistical sensitivity study quantitatively evaluated the uncertainty of EP imaging caused by the variations in personalized anatomical models in healthy and post-infarction settings, using two of the existing EP imaging systems (ECGI and TEPI methods) as testbeds for our study. The spatial STD maps of epicardial and transmural potential dynamics summarized the variations in the ECGI and TEPI solutions caused by the input anatomical variations. The presented approach is shown to be able to quantify the otherwise ambiguous uncertainties introduced in the EP imaging by anatomical modeling errors. Our experimental results showed that the current practice of EP imaging – relying on detailed personalized anatomical model –

is robust to modeling errors at the level of shape variations inherently associated with image quality, segmentation users, and segmentation methods.

While this study only considers two sources of variations in personalized ventricular models, the presented approach can be used to study a wider variety of anatomical variations such as that in modeling the torso model.

The finding of this study indicates the possibility that high-level complexity in personalized anatomical models might not be necessary for reliable EP imaging and, as a result, the process of anatomical modeling in current EP imaging systems may be simplified for improved clinical feasibility in future practice. Based on this finding, in the next chapter, we propose a cardiac minimal anatomical model that only incorporates subject-specific anatomical parameters while discarding the shape details. This minimal model is constructed using minimal resources and intervention, which facilitates application of EP imaging in future clinical settings.

## Chapter 6

# Cardiac Simplified Anatomical Model

### 6.1 Background

Cardiac electrophysiological (EP) imaging techniques rely on anatomically-detailed models of heart and torso, derived from whole-body tomographic scans of the individual subject under study. This common practice in EP imaging was set based on the findings of the previous studies that EP imaging fails if generic anatomical models are used rather than subject-specific ones, and certain subject-specific *global* anatomical parameters (heart size, position and orientation with respect to body-surface electrodes) need to be incorporated to allow accurate EP imaging [22, 25]. However, detailed personalized anatomical modeling largely relies on the quality of the tomographic images, which restricts the imaging choices to high-quality MR/CT scans, excluding more accessible and less expensive imaging modalities in clinical setting such as ultrasound. In addition, detailed anatomical modeling involves a time-consuming, expert-dependent process, the

complexity of which contradicts clinical applicability. At the same time, the anatomical modeling process involves uncertainties originating from image quality, inter- / intra-individual segmentation, or different segmentation tools that impact the solution of EP imaging. In chapter 5, we described a systematic statistical approach to study the impact of anatomical modeling variations on EP imaging. Our experimental results indicated that EP imaging is robust to the anatomical modeling variations in the level of shape details as long as the global anatomical parameters are correctly captured.

Based on this finding, we take one step further to study if the local shape details in a personalized anatomical model can be discarded without affecting the diagnostic characteristics of EP imaging. We propose a cardiac simplified anatomical model that only incorporates essential subject-specific anatomical parameters while discarding the anatomical shape details. This simplified anatomical model describes the heart using regular 3D geometrical shapes, parameters of which reflect the essential subject-specific anatomical parameters. Exploiting less resources and processing for personalization of the proposed cardiac simplified anatomical model, this simplified anatomical model improves anatomical modeling experience for future clinical application of EP imaging.

The performance of our proposed simplified anatomical model compared to anatomically-detailed heart model in cardiac EP imaging is investigated through a set of real-data experiments.

## 6.2 Personalized Simplified Anatomical Model of Heart

We propose a simplified ventricular model based on analytic descriptions of regular 3D geometrical shapes (Fig. 6.1). In this simplified ventricular model, the left ventricular

epicardium and endocardium are described by two concentric circles at short axis and an ellipsoid at long axis as:

$$R_{Lendo}^2 (\text{or } R_{Lepi}^2) = (\epsilon - \epsilon_0)^2 + (\eta - \eta_0)^2 + a_l^2(\zeta - \zeta_0)^2 \quad (6.1)$$

where  $\epsilon - \eta$  plane represents the short-axis plane and  $\zeta$  is the long axis of the heart,  $(\epsilon_0, \eta_0, \zeta_0)$  represents center of LV base,  $R_{Lendo}$  and  $R_{Lepi}$  are the radii of LV endocardium and epicardium ( $R_{Lepi} > R_{Lendo}$ ), respectively, and  $a_l$  describes ellipticity of the shape. This model is experimentally shown to better represent LV geometry compared to other geometrical shapes in [91].

The right ventricular surface is represented using two concentric circles intersecting with LV circles at short-axis ( $\epsilon - \eta$  plane) and a parabola at long axis ( $\zeta$  direction) [92] as:

$$\zeta = \zeta_0^r + a_r((\epsilon - \epsilon_0^r)^2 + (\eta - \eta_0^r)^2) \quad (6.2)$$

where  $(\epsilon_0^r, \eta_0^r, \zeta_0^r)$  is the center of the two concentric circles representing the free wall of RV endocardium. Radii  $R_{Rendo}$  and  $R_{Repi}$  are determined at the base-slice and kept fixed along the  $\zeta$  direction.  $(\epsilon_0^r, \eta_0^r, \zeta_0^r)$  always resides on LV endocardium so the distance  $d_r$  between  $(\epsilon_0, \eta_0, \zeta_0)$  and  $(\epsilon_0^r, \eta_0^r, \zeta_0^r)$  is equal to the radius of LV endocardium, and decreases along the long axis from the base to apex determined by the elongation of the shape (described by  $a_r$ ). This simplified ventricular model (Fig. 6.1) can be seen as an anatomically-plausible model that is personalized to a subject's heart anatomy without including realistic shape details.

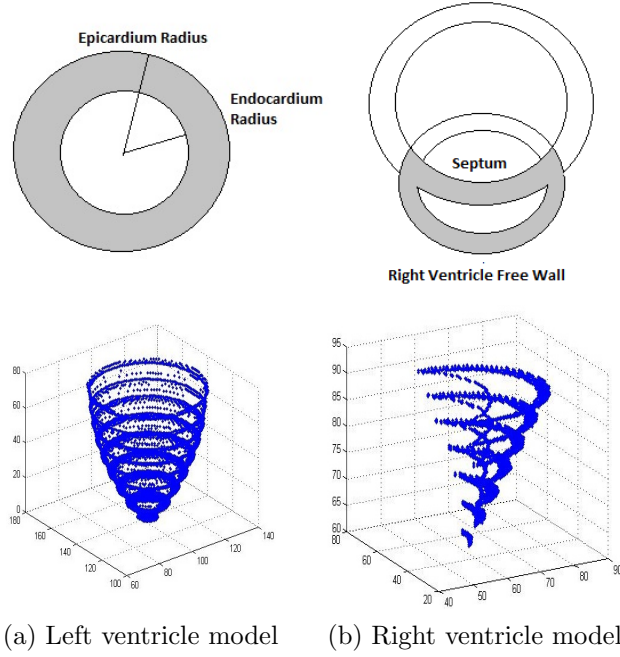


FIGURE 6.1: Cardiac simplified anatomical model

Subject-specific global anatomical parameters (heart size, position and orientation) are incorporated into this simplified model through parameters of the geometrical shapes such as center and radii of endocardium and epicardium circles as well as length of the ellipsoid. Specifically, heart position is determined by the center of the LV base that can be derived from the base-slice of the short-axis cardiac scans. It is incorporated in the simplified model of LV as  $(\epsilon_0, \eta_0, \zeta_0)$ . Heart orientation is determined by the normal direction of its short-axis (SA), horizontal long-axis (hLA) and vertical long-axis (vLA) view plane. These parameters can be quickly calculated from image meta-data (ImageOrientationPatient) and click interaction with the short-axis scans. For the anatomically-plausible ventricular model, the SA, hLA and vLA planes explicitly correspond to the  $\epsilon - \eta$ ,  $\epsilon - \zeta$  and  $\eta - \zeta$  planes. Heart size is incorporated through the radii, wall thickness ( $R_{Lendo}$ ,  $R_{Lepi}$ ,  $R_{Rendo}$ ,  $R_{Rep}$ ), and length of the ventricles ( $a_l$ ,  $a_r$ ). The first two sets of parameters can be obtained from the base SA scans. The length is determined by the distance between the base and apex. Table 6.1 summarizes the

TABLE 6.1: Summary of parameters, imaging data and operation involved in the proposed simplified ventricular modeling.

	Position	Orientation	Size
Anatomical parameters	Base center	SA, hLA, vLA planes	Radii, wall thickness & length of ventricles
Model parameters	$(\epsilon_0, \eta_0, \zeta_0)$	$\epsilon - \eta$ , $\epsilon - \zeta$ , $\eta - \zeta$ planes	$R_{Lendo}, R_{Lepi}, R_{Rendo}, R_{Repi}, a_l, a_r$
Image data	Base SA slice	Base SA slice	Base SA slice, total number of base-to-apex SA slices
Interaction	Click (1)	Click (1)	Click (4)
Operation	Translation	Rotation	Scaling

information and procedure required for preparation of cardiac simplified model including only 6 click interactions with the base scan of the ventricles and the knowledge of the total number of apex-to-base SA scans in order to incorporate subject-specific data. The anatomically-plausible model is substantially simpler to prepare and to customize (explicit parameters in Table 6.1) compared to anatomically-detailed model.

### 6.3 Experiments and Results

Following the same experimental settings as Chapter 5, we consider two EP imaging approach (ECGI and TEPI, described in section 5.2) as testbeds for our experiments. We conduct a set of real-data experiments on the four human subjects presented in chapter 5.

On the four heart models in real-data experiments of Chapter 5, we construct corresponding simplified anatomical model for each subject. Coupling our simplified model of each subject with its BSP measurements, we reconstruct EP outcomes for each subject using ECGI and TEPI methods. Similarly, infarct quantification is performed as explained in the real-data experiments section of chapter 5. The results of ECGI method for case 3 and 4 are presented in Fig. 6.2. As can be seen, the reconstructed epicardial

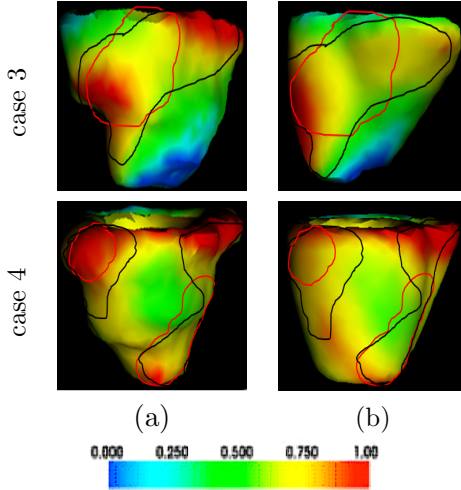


FIGURE 6.2: ECGI solution for simplified ventricular models of case 3 and case 4 during depolarization. Black and red contours show the ECGI estimated and the reference infarct region, respectively.

potential maps for the simplified model of both cases are similar to that of the more realistic anatomical models. TEPI results on simplified models of case 3 and case 4 are presented in Fig. 6.3. As highlighted in Fig. 6.3, there is a good agreement between the infarct region detected using detailed anatomical details and the one detected with the simplified model in both cases.

This preliminary study reports negligible role of anatomical details in EP imaging as well as potentials of the proposed simplified model that can be quickly personalized to a patient's global geometrical parameters. However, more comprehensive experiments including different cardiac pathologies are required to obtain a statistically accurate conclusion.

## 6.4 Conclusions

EP imaging techniques commonly utilize detailed personalized anatomical models of heart and torso to obtain the mathematical relation between cardiac bioelectrical sources and body-surface measurements. This practice requires high-quality tomographic data,

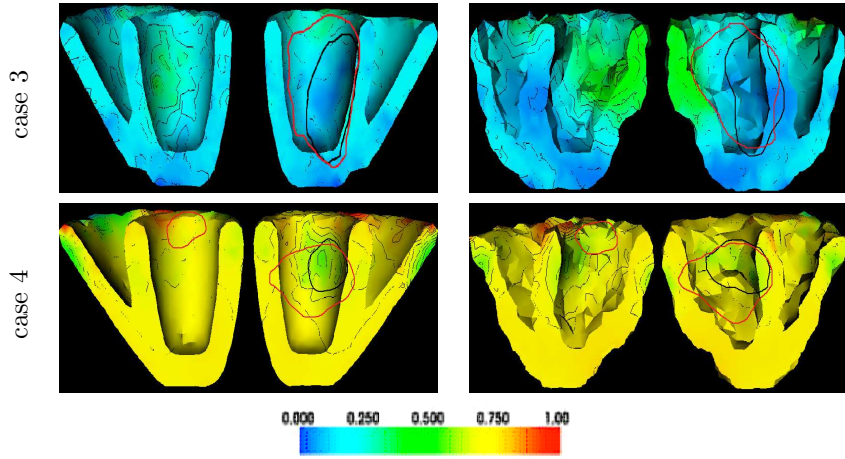


FIGURE 6.3: TEPI solution for simplified ventricular models of case 3 and case 4. Black and red contours show the TEPI estimated and the reference infarct region, respectively. Color encodes the value of potential magnitude.

high expertise in anatomical modeling, and a lot of time, making clinical translation of EP imaging challenging. It also involves uncertainties caused by image quality and anatomical modeling process. The robustness of EP imaging to the anatomical modeling variations in shape-detail level was established in Chapter 5 through a systematic statistical approach. It led us to propose a cardiac simplified anatomical model that only includes certain personalized anatomical parameters, while discarding anatomical details. Our proposed personalized cardiac simplified model provided promising EP imaging results in myocardial infarction setting, though more extensive experiments on different cardiac pathologies are required for a more statistically significant conclusion. Being easily and quickly customizable to a patient’s anatomy, the proposed cardiac simplified anatomical model has potential to improve anatomical modeling experience for future clinical application of cardiac EP imaging.

# Chapter 7

## Summary

### 7.1 Conclusions

Cardiac electrophysiological (EP) imaging involves solving an inverse problem that infers cardiac electrical activity from body-surface electrocardiography data on the physical domain defined by the body torso. To avoid unreasonable solutions that may fit the data, this inference is often guided by data-independent prior assumptions about models of different properties of cardiac electrical sources as well as the physical domain. However, these prior assumptions/models may involve errors and uncertainties that could affect the inference accuracy. For example, common prior assumptions on the source properties, such as fixed spatial and/or temporal smoothness or sparseness assumptions, may not necessarily match the true source property at different conditions, leading to uncertainties in the inference. Furthermore, prior assumptions on the physical domain, such as the anatomy and tissue conductivity of different organs in the thorax model, represent an approximation (rather than exact) of the physical domain, introducing errors to the inference. To determine the robustness of cardiac EP imaging for its future

clinical application, it is important to assess and reduce the impact of these uncertainties on the solution of cardiac EP imaging.

In this dissertation, we specifically focused on the quantification and reduction of the impact of uncertainties caused by prior assumptions about the source properties as well as anatomical modeling on the solution of EP imaging.

### **Uncertainties in Prior Assumptions on Cardiac Source Properties**

We demonstrated the inefficacy of fixed prior models in estimating spatiotemporally changing cardiac sources using a simple yet novel  $Lp$ -norm regularization method. Conducting phantom and real-data experiments with a focus on imaging source activity along the infarct border, we considered a wide range of source distributions with different structures and extents. Our experimental results reported the limitation of fixed prior models in accurate reconstruction of cardiac sources at different conditions. This empirical study also illustrated the ability of  $Lp$ -norm prior model, with varying  $p$  value, to reflect spatiotemporally changing property of cardiac sources, building the foundation for our multiple-model approach.

We then proposed a hierarchical multiple-model approach for volumetric cardiac source imaging that reduces the uncertainties caused by fixed prior models. Considering  $Lp$ -norm prior for current sources, where  $p$  is automatically inferred from the data, this method incorporates a continuous combination of prior models, each reflecting a specific source structure. In this way, our proposed method can automatically adapt to different structural properties of cardiac sources, unlike fixed prior models that only suit a specific source property. This capability of our proposed method was validated through a comprehensive set of synthetic and real-data experiments including various typical

pathological conditions and/or diagnostic procedures, such as myocardial infarction and pacing.

Our proposed multiple-model Bayesian framework allows for estimation of other unknown system parameters in addition to source distribution. Automatic rather than ad hoc selection of the parameters alleviates the challenge of attempting to pre-define accurate parameters that often arises in deterministic regularization.

Our framework also provides complete distribution of cardiac source estimations, giving more insight through statistical characteristics of the solution, in contrast to deterministic regularization methods that only provide a point estimation.

### **Uncertainties in Prior Assumptions on Anatomical Modeling**

We investigated the impact of uncertainties in highly-detailed anatomical models using a systematic statistical framework that first quantifies the uncertainties of personalized anatomical modeling and then assesses their impact on the solution of EP imaging. It was achieved by novel application of statistical shape modeling (SSM) to model/quantify the otherwise ambiguous anatomical modeling variations, followed by utilization of unscented transform (UT) to establish an otherwise complex relation between input and output uncertainties. Our experimental results showed the robustness of EP imaging to the anatomical modeling variations in shape detail in two different healthy and post-infarction settings. Furthermore, these results suggested that shape details can be discarded without affecting the diagnostic solution of EP imaging, which directed us to a cardiac simplified anatomical model.

We then proposed a cardiac simplified anatomical model that only incorporates subject-specific anatomical parameters while discarding anatomical shape details. The effectiveness of this simplified model for EP imaging was verified through a set of real-data experiments on post-infarction human patients. This model requires less resources and processing in order to be customized to patient's anatomy, improving anatomical modeling experience for clinical application of EP imaging.

## 7.2 Future Work

In addition to the above-mentioned contributions to the field of cardiac EP imaging, this dissertation opens new avenues for future directions of this field, as follows:

### Experimental Validation

Our current multiple-model hierarchical approach exhibited promising clinical potential, yet more real-data experiments and investigation are needed, particularly for different cardiac pathologies, where cardiac sources exhibit complex spatial distributions.

Our simplified model also needs to be validated for different conditions in addition to myocardial infarction. EP imaging in different cardiac pathologies may require different levels of anatomical accuracy that need to be determined through an extensive real-data study including different cardiac conditions.

### Integration with Temporal Model

Our current multiple-model hierarchical approach only focuses on spatial properties of cardiac sources. Combining it with physiological models of cardiac electrical propagation

not only enables automatic adaptation to spatial properties of the sources, but also improves evolution of source properties over time. This spatiotemporally integrated approach will improve consistency over time and robustness to noise, thanks to the guidance of the incorporated physiological model.

## **Application to Other Domains**

This study demonstrates the importance of a multiple-model in comparison to a fixed-model approach in constraining ill-posed inverse problems. While targeted at the application of non-invasive cardiac EP imaging in this work, the underlying concept and method can be customized to be applied to a broader variety of inverse problems that face the challenge of model-data mismatch.

## **Appendix A**

# **Publications**

### **Peer-Reviewed Journal Articles**

1. Azar Rahimi, and Linwei Wang, Sensitivity of Noninvasive Cardiac Electrophysiological Imaging to Variations in Personalized Anatomical Modeling, IEEE Transactions on Biomedical Imaging, in press, 2015
2. Azar Rahimi, Jingjia Xu, and Linwei Wang, Lp-Norm Regularization in Volumetric Imaging of Cardiac Current Sources, Computational and Mathematical Methods in Medicine, Hindawi, vol 2013, article ID 276478, 10 pages, 2013
3. Azar Rahimi, Jingjia Xu, and Linwei Wang, Imaging Transmural Cardiac Source Activity using a Hierarchical Multiple-Model Bayesian Approach, IEEE Transaction on Medical Imaging, under review

## Peer-Reviewed Conference Papers

4. Azar Rahimi, Jingjia Xu, and Linwei Wang, Multiple-Model Bayesian Approach to Volumetric Imaging of Cardiac Current Sources, IEEE International Conference on Image Processing (ICIP), Paris, France, October 2014, pp 3522-3526
5. Azar Rahimi, Jingjia Xu, and Linwei Wang, Hierarchical Multiple-Model Bayesian Approach to Transmural Electrophysiological Imaging. In Polina Golland, Nobuhiko Hata, Christian Barillot, Joachim Hornegger, and Robert Howe (Eds), Medical Image Computing and Computer-Assisted Intervention (MICCAI), Boston, USA, September 2014, Lecture Notes in Computer Science, Springer, 8674:538-545, 2014
6. Azar Rahimi, Jingjia Xu, and Linwei Wang: Electrophysiologic Imaging of Volumetric Infarct Border Using a Spatiotemporal L<sub>p</sub>-Norm Constraint, IEEE International Symposium on Biomedical Imaging (ISBI), Beijing, China, May 2014, pp 612-615 (best paper travel award)
7. Azar Rahimi and Linwei Wang, The Impact of Ventricular Shape Variations on Inverse Electrocardiography: A Feasibility Study. IEEE International Symposium on Biomedical Imaging (ISBI), pp 564-567, 2013 (podium presentation, acceptance rate 18
8. Azar Rahimi, Jingjia Xu, John R Fitz-Clarke, and Linwei Wang, Volumetric Imaging of Cardiac Current Source using L<sub>p</sub>-Norm Regularization, Computing in Cardiology (CinC), pp 715-718, 2013
9. Azar Rahimi, Jingjia Xu and Linwei Wang: Impact of Local Variations in Ventricular Anatomical Models on Transmural Electrophysiological Imaging. Computing in Cardiology (CinC), pp 957-960, 2012

10. Azar Rahimi, Hongda Mao, Pengcheng Shi, and Linwei Wang: Toward Clinically-Feasible Noninvasive Electrophysiological Imaging: Investigating the Impact of Local Anatomical Detail, MICCAI Workshop on Statistical Atlases and Computational Models of the Heart (MICCAI-STACOM), Toronto, Canada, September, Lecture Notes in Computer Science, vol 7085, Pp 188-197, 2012

# Bibliography

- [1] Anatomy and physiology: the conduction system of the heart. <http://bitesizenursing.blogspot.com/2012/04/anatomy-and-physiology-conduction.html>, 2012.
- [2] Standard 12-lead ECG. <http://www.ems12lead.com/2008/10/17/12-lead-ecg-lead-placement-diagrams/>, 2008.
- [3] 12-lead electrocardiogram EKG. <http://www.washingtonhra.com/31.html>, 2004.
- [4] F. D. Dawoud. Using inverse electrocardiography to image myocardial infarction. *Computers in Cardiology*, pages 177–180, Sept 2007.
- [5] BSPM. <http://www2.le.ac.uk/research/festival/meet/2013/science/vanheusden/page-two>, 2013.
- [6] D. H. Brooks, I. F. Ahmad, R. S. Macleod, and G. M. Maratos. Inverse electrocardiography by simultaneous imposition of multiple constraints. *IEEE Transaction on Biomedical Engineering*, 46:3–17, 1999.
- [7] S. Nazarian. Cmr for mapping the missing dimension in ventricular tachycardia ablation. *JACC Cardiovascular Imaging*, 3(3):286–288, 2010.
- [8] W. G. Stevenson. Ventricular scars and ventricular tachycardia. *Transactions of American clinical and climatological Association*, 120:403–412, 2009.

- [9] J. M. de Bakker, F. J. Van Capelle, M. J. Janse, S. Tasseron, J. T. Vermeulen, N. de Jonge, and J. R. Lahpor. Slow conduction in the infarcted human heart, zigzag course of activation. *Circulation*, 88(3):915–926, 1993.
- [10] I. F. Gorodnitsky and B. D. Rao. Sparse signal reconstruction from limited data using FOCUSS: a re-weighted minimum norm algorithm. *IEEE Transactions on Signal Processing*, 45:600–616, 1997.
- [11] R. Plonsey. *Bioelectric phenomena*. McGraw Hill, New York, 1969.
- [12] Y. Okamoto, Y. Teramachi, and T. Musha. Limitation of the inverse problem in body surface potential mapping. *IEEE Transactions on Biomedical Engineering*, 30(11):749–754, 1983.
- [13] B. Messnarz, B. Tilg, R. Modre, G. Fischer, and F. Hanser. A new spatiotemporal regularization approach for reconstruction of cardiac transmembrane potential patterns. *IEEE Transactions on Biomedical Engineering*, 51(2):273–281, 2004.
- [14] Y. Rudy and H. Oster. The electrocardiographic inverse problem. *Critical Review in Biomedical Engineering*, 20(1).
- [15] S. Ghosh and Y. Rudy. Application of l1-norm regularization to epicardial potential solutions of the inverse electrocardiography problem. *Annals of Biomedical Engineering*, 37(5):692–699, 2009.
- [16] G. Shou, L. Xia, F. Liu, M. Jiang, and S. Crozier. On epicardial potential reconstruction using regularization schemes with the l1-norm data term. *Physics in Medicine and Biology*, 56(1):57–72, 2011.

- [17] L. Wang, J. Qin, T. T. Wong, and P. A. Heng. Application of l1-norm regularization to epicardial potential reconstruction based on gradient projection. *Physics in Medicine and Biology*, 56(19):6291–6310, 2011.
- [18] J. Xu, A. R. Dehaghani, F. Gao, and L. Wang. Noninvasive transmural electro-physiological imaging based on minimization of total-variation functional. *IEEE Transactions on Medical Imaging*, 33(9):1860–1874, 2014.
- [19] L. Wang, H. Zhang, K. Wong, H. Liu, and P. Shi. Physiological-model-constrained noninvasive reconstruction of volumetric myocardial transmembrane potentials. *IEEE Transactions on Biomedical Engineering*, 57(2):296–315, 2010.
- [20] B. He, G. Li, and X. Zhang. Noninvasive imaging of cardiac transmembrane potentials within three-dimensional myocardium by means of a realistic geometry anisotropic heart model. *IEEE Transactions on Biomedical Engineering*, 50:1190–1202, 2003.
- [21] B. J. Messinger-Rapport and Y. Rudy. The inverse problem in electrocardiography: A model study of the effects of geometry and conductivity parameters on the reconstruction of epicardial potentials. *IEEE Transactions on Biomedical Engineering*, 33(7):667–676, july 1986.
- [22] G. Huiskamp and A. Van Oosterom. Tailored versus realistic geometry in the inverse problem of electrocardiography. *IEEE Transactions on Biomedical Engineering*, 36(8):827–835, 1989.
- [23] C. Ramanathan and Y. Rudy. Electrocardiographic imaging: II. effect of torso inhomogeneities on noninvasive reconstruction of epicardial potentials, electrograms, and isochrones. *Journal of Cardiovascular Electrophysiology*, 12(2):241–252, 2001.

- [24] S. E. Geneser, R. M. Kirby, and R. S. MacLeod. Application of stochastic finite element methods to study the sensitivity of ecg forward modeling to organ conductivity. *IEEE Transactions on Biomedical Engineering*, 55(1):31–40, 2008.
- [25] D. J. Swenson, S. E. Geneser, J. G. Stinstra, Kirby R. M, and R. S. MacLeod. Cardiac position sensitivity study in the electrocardiographic forward problem using stochastic collocation and boundary element methods. *Annals of Biomedical Engineering*, 39(12):2900–2910, 2011.
- [26] R. Hren, J. Nenonen, and B. M. Horacek. Simulated epicardial potential maps during paced activation reflect myocardial fibrous structure. *Annals of Biomedical Engineering*, 26(6):1022–1035, 1998.
- [27] P. ColliFranzone, L. Guerri, C. Viganotti, E. Macchi, S. Baruffi, S. Spaggiari, and B. Taccardi. Potential fields generated by oblique dipole layers modeling excitation wavefronts in the anisotropic myocardium. comparison with potential fields elicited by paced dog hearts in a volume conductor. *Circulation*, 51:330–346, 1982.
- [28] M. Nash. *Mechanics and Material Properties of the Heart using an Anatomically Accurate Mathematical Model*. PhD thesis, Univ. of Auckland, New Zealand, 1998.  
URL <http://www.esc.auckland.ac.nz/Nash/thesis/>.
- [29] G. Fischer, B. Tilg, R. Modre, G. J. M. Huiskamp, J. Fetzer, W. Rucker, and P. Wach. A bidomain model based bem-fem coupling formulation for anisotropic cardiac tissue. *Annals of Biomedical Engineering*, 28(10):1229–1243, 2000.
- [30] L. Wang, H. Zhang, K. Wong, H. Liu, and P. Shi. Electrocardiographic simulation on personalized heart-torso structures using coupled meshfree-bem platform. *International Journal of Functional Informatics and Personalized Medicine*, In press, 2009.

- [31] Y. Rudy and B. Messinger-Rapport. The inverse problem of electrocardiography: solutions in terms of epicardial potentials. *Critical Reviews in Biomedical Engineering*, 16:215–268, 1988.
- [32] A. J. Pullan, L. K. Cheng, M. P. Nash, C. P. Bradley, and D. J. Paterson. Noninvasive electrical imaging of the heart: Theory and model development. *Annals of Biomedical Engineering*, 29:817–836, 2001.
- [33] C. Ramanathan, R. N. Ghanem, P. Jia, K. Ryu, and Y. Rudy. Noninvasive electrocardiographic imaging for cardiac electrophysiology and arrhythmia. *Nature Medicine*, 10:422–428, 2004.
- [34] G. Huiskamp and F. Greensite. A new method for myocardial activation imaging. *IEEE Transactions on Biomedical Engineering*, 44(6):433–446, 1997.
- [35] P. M. van Dam, T. F. Oostendorp, A. C. Linnenbank, and A. van Oosterom. Noninvasive imaging of cardiac activation and recovery. *Annals of Biomedical Engineering*, 37(9):1739–1756, 2009.
- [36] Y. Serinagaoglu, D. H. Brooks, and R. S. Macleod. Improved performance of bayesian solution for inverse electrocardiography using multiple information sources. *IEEE Transactions on Biomedical Engineering*, 53(10):2024–2034, 2006.
- [37] B. He and D. Wu. Imaging and visualization of 3-d cardiac electric activity. *IEEE Transactions on Information Technology in Biomedicine*, 5(3):181–186, 2001.
- [38] B. F. Nielsen, M. Lysaker, and P. Grottum. Computing ischemic regions in the heart with the bidomain model: First steps towards validation. *IEEE Transactions on Medical Imaging*, 32(6):1085–1096, 2013.

- [39] S. Ohyu, Y. Okamoto, and S. Kuriki. Use of the ventricular propagated excitation model in the magnetocardiographic inverse problem for reconstruction of electrophysiological properties. *IEEE Transactions on Biomedical Engineering*, 49(6):509–519, June 2002.
- [40] A. Rahimi, J. Xu, and L. Wang. Hierarchical multiple-model bayesian approach to transmural electrophysiological imaging. *Medical Image Computing and Computer-Assisted Intervention MICCAI 2014*, 8674:538–545, 2014.
- [41] Z. Liu, C. Liu, and B. He. Noninvasive reconstruction of three-dimensional ventricular activation sequence from the inverse solution of distributed equivalent current density. *IEEE Transactions on Medical Imaging*, 25(10):1307–1318, 2006.
- [42] Howard S. Oster and Yoram Rudy. The use of temporal information in the regularization of the inverse problem of electrocardiography. *IEEE Transactions on Biomedical Engineering*, 39(1):65–75, 1992.
- [43] D. Wang, R. M. Kirby, R. S. MacLeod, and C. R. Johnson. Identifying myocardial ischemia by inversely computing transmembrane potentials from body-surface potential maps. In *International Conference on Bioelectromagnetism (NFSI ICBEM)*, pages 121–125, 2011.
- [44] F. Greensite. Second-order approximation of the pseudoinverse for operator deconvolutions and families of ill-posed problems. *SIAM Journal on Applied Mathematics*, 59(1):1–16, 1998.
- [45] Inc. CVX Research. CVX: Matlab software for disciplined convex programming, version 2.0 beta. <http://cvxr.com/cvx>, September 2012.

- [46] R. Aliev and E. V. Panfilov. A simple two-variable model of cardiac excitation, 1996.
- [47] Physionet/computers in cardiology challenge 2007: Electrocardiographic imaging of myocardial infarction. <http://physionet.org/challenge/2007/>, 2007.
- [48] L. M. Title, S. E. Iles, M. J. Gardner, C. J. Penney, J. C. Clements, and B. M. Horacek. Quantitative assessment of myocardial ischemia by electrocardiographic and scintigraphic imaging. *Journal of Electrocardiology*, 36(Suppl):17–26, 2003.
- [49] M. D. Cerqueira, N. J. Weissman, V. Dilsizian, et al. Standardized myocardial segmentation and nomenclature for tomographic imaging of the heart. *Circulation*, 105:539–542, 2002.
- [50] B. Erem, J. Coll-Font, R. Martinez Orellana, P. Stovicek, and D. H. Brooks. Using transmural regularization and dynamic modeling for noninvasive cardiac potential imaging of endocardial pacing with imprecise thoracic geometry. *IEEE Transactions on Medical Imaging*, 33(3):726–738, March 2014.
- [51] G. J. Schiller and P. S. Maybeck. Control of a large space structure using mmae/mmac techniques. *IEEE Transactions on Aerospace and Electronic Systems*, 33(4):1122–1131, 1997.
- [52] V. Lippiello, B. Siciliano, and L. Villani. Adaptive extended kalman filtering for visual motion estimation of 3d objects. *Control Engineering Practice*, 15(1):123–134, 2007.
- [53] M. Ficocelli and F. Janabi-Sharifi. Adaptive filtering for pose estimation in visual servoing. In *IEEE International Conference on Intelligent Robots and Systems*, volume 1, pages 19–24, 2001.

- [54] A. Gelman, J. B. Carlin, H. S. Stern, and D. B. Rubin. *Bayesian Data Analysis*. Chapman and Hall, 2003.
- [55] J. Kaipio and E. Somersalo. *Statistical and Computational Inverse Problems*, volume 160. Applied Mathematical Sciences, Springer.
- [56] G. E. P. Box and G. C. Tiao. *Bayesian Inference in Statistical Analysis*. John Wiley and Sons, Inc., 1973.
- [57] R. M. Neal. Slice sampling. *The Annals of Statistics*, 31:705–767, 2003.
- [58] W. R. Gilks, S. Richardson, and D. J. Spiegelhalter. *Markov Chain Monte Carlo in Practice*. Chapman and Hall, London, 1996 (ISBN: 0-412-05551-1).
- [59] R. R. Aliev and A. V. Panfilov. A simple two-variable model of cardiac excitation. *Chaos, Solitons & Fractals*, 7(3):293–301, 1996.
- [60] L. Wang, K. Wong, H. Zhang, H. Liu, and P. Shi. Noninvasive computational imaging of cardiac electrophysiology for 3D infarct quantitation. *IEEE Transactions on Biomedical Engineering*, (4):1033–1034, 2011.
- [61] D. Farina. Model-based approach to the localization of infarction. In *Proc. Computers in Cardiology*.
- [62] M. A. Mneimneh and R. J. Povinelli. Rps/gmm approach toward the localization of myocardial infarction. In *Proc. Computers in Cardiology*.
- [63] J. L. Sapp, F. Dawoud, J. C. Clements, and B. M. Horacek. Inverse solution mapping of epicardial potentials quantitative comparison with epicardial contact mapping. *Circulation: Arrhythmia and Electrophysiology*, pages 1001–1009, 2012.

- [64] L. Wang, F. Dawoud, S. Yeung, P. Shi, K. C. L. Wong, H. Liu, and A. C. Lardo. Transmural imaging of ventricular action potentials and post-infarction scars in swine hearts. *IEEE Transactions on Medical Imaging*, 32(4):731–747, April 2013.
- [65] A. Myronenko and X. Song. Point set registration: Coherent point drift. *IEEE Transactions on Pattern Analysis and Machine Intelligence*, 32(12):2262–2275, Dec 2010.
- [66] Emmanuel Vincent. Complex nonconvex lp norm minimization for underdetermined source separation. In *Independent Component Analysis and Signal Separation*, volume 4666 of *Lecture Notes in Computer Science*, pages 430–437. 2007.
- [67] J. Ringenberg, M. Deo, D. Filgueiras-Rama, G. Pizarro, B. Ibanez, R. Peinado, Jose L Merino, O. Berenfeld, and V. Devabhaktuni. Effects of fibrosis morphology on reentrant ventricular tachycardia inducibility and simulation fidelity in patient-derived models. *Clinical Medicine Insights: Cardiology*, 8:1–13, 2014.
- [68] J. Relan, P. Chinchapatnam, M. Sermesant, K. Rhode, M. Ginks, H. Delingette, CA. Rinaldi, R. Razavi, and N. Ayache. Coupled personalization of cardiac electrophysiology models for prediction of ischaemic ventricular tachycardia. *Interface Focus*, 1(3):396–407, 2011.
- [69] G. Fischer, B. Tilg, R. Modre, G. J. M. Huiskamp, J. Fetzer, W. Rucker, and P. Wach. A bidomain model based bem-fem coupling formulation for anisotropic cardiac tissue. *Annals of Biomedical Engineering*, 28:1229–1243, 2000.
- [70] L. K. Cheng, J. M. Bodley, and A. J. Pullan. Comparison of potential- and activation-based formulations for the inverse problem of electrocardiology. *IEEE Transactions on Biomedical Engineering*, 50(1):11–22, Jan 2003.

- [71] W. H. W. Schulze, F. E. Henar, D. Potyagaylo, A. Loewe, M. Stenroos, and O. Dossel. Kalman filter with augmented measurement model: An ecg imaging simulation study. volume 7945 of *Lecture Notes in Computer Science*, pages 200–207. 2013. ISBN 978-3-642-38898-9.
- [72] J. Xu, J. L. Sapp, A. Rahimi, F. Gao, and L. Wang. Bayesian integrate of physiological dynamic and spatial sparse priors for the robustness of 3d cardiac electrophysiology. In *Medical Image Computing and Computer-Assisted Intervention, MICCAI 2015*, Lecture Notes in Computer Science, accepted. 2015.
- [73] H. Arevalo, G. Plank, P. Helm, H. Halperin, and N. Trayanova. Tachycardia in post-infarction hearts: Insights from 3d image-based ventricular models. *PLoS ONE*, 8(7):e68872, 2013.
- [74] M. Wilhelms, O. Dossel, and G. Seemann. In silico investigation of electrically silent acute cardiac ischemia in the human ventricles. *IEEE Transactions on Biomedical Engineering*, 58(10):2961–2964, Oct 2011.
- [75] M. Wilhelms, O. Dossel, and G. Seemann. Comparing simulated electrocardiograms of different stages of acute cardiac ischemia. *Functional Imaging and Modeling of the Heart*, 6666:11–19, 2011.
- [76] P. Lamata, S. Niederer, D. Barber, D. Norsletten, J. Lee, R. Hose, and N. Smith. Personalization of cubic hermite meshes for efficient biomechanical simulations. *Medical Image Computing and Computer-Assisted Intervention MICCAI 2010*, 13:380–387, 2010.
- [77] T. Heimann and H. Meinzer. Statistical shape models for 3d medical image segmentation: A review. *Medical Image Analysis*, 13(4):543–563, 2009.

- [78] R. R. Dickerson, D. H. Stedman, and A. C. Delany. Direct measurements of ozone and nitrogen dioxide photolysis rates in the troposphere. *Journal of Geophysical Research: Oceans*, 87:4933–4946, 1982.
- [79] D. Xiu and G. E. Karniadakis. The wiener–askey polynomial chaos for stochastic differential equations. *SIAM Journal on Scientific Computing*, 24(2):619–644, 2002.
- [80] S. J. Julier and J. K. Uhlmann. A new extension of the kalman filter to nonlinear systems. In *Proc. Aerospace/Defense Sensing, Simulation and Controls*, pages 182–193, 1997.
- [81] F. Augustin, A. Gilg, M. Paffrath, P. Rentrop, M. Villegas, and U. Wever. An accuracy comparison of polynomial chaos type methods for the propagation of uncertainties. *Journal of Mathematics in Industry*, 3, 2013.
- [82] L. Wang, H. Zhang, K. C. L. Wong, and P. Shi. Coupled meshfree-bem platform for electrocardiographic simulation: Modeling and validations. *Medical Imaging and Augmented Reality, Lecture Notes in Computer Science*, 5128:98–107, 2008.
- [83] S. Wellek. *Testing Statistical Hypotheses of Equivalence and Noninferiority*. CRC Press, 2010.
- [84] R. S. MacLeod, C. R. Johnson, and P. R. Ershler. Construction of an inhomogeneous model of the human torso for use in computational electrocardiography. *IEEE Engineering in Medicine and Biology Society 13th Annual International Conference*, pages 688–689, 1991.
- [85] A. L. Goldberger et al. Physiobank, physiotoolkit, and physionet components of a new research resource for complex physiological signals. *Circulation*, 101:215–220, 2000.

- [86] J. E. Burnes, B. Taccardi, R. S. MacLeod, and Y. Rudy. Noninvasive ecg imaging of electrophysiologically abnormal substrates in infarcted hearts : A model study. *Circulation*, 101(5):533–540, 2000.
- [87] I. R. Efimov, T. D. Huang, J. M. Rendt, and G. Salama. Optical mapping of repolarization and refractoriness from intact heart. *Circulation*, 90:1469–1480, 1994.
- [88] T. Berger, B. Pfeifer, F. F. Hanser, F. Hintringer, G. Fischer, M. Netzer, T. Trieb, M. Stuehlinger, W. Dichtl, C. Baumgartner, O. Pachinger, and M. Seger. Single-beat noninvasive imaging of ventricular endocardial and epicardial activation in patients undergoing crt. *PLoS ONE*, 6(1), 2011.
- [89] P. S. Cuculich, J. Zhang, Y. Wang, K. A. Desouza, R. Vijayakumar, P. K. Woodard, and Y. Rudy. The electrophysiological cardiac ventricular substrate in patients after myocardial infarction: Noninvasive characterization with electrocardiographic imaging. *Journal of the American College of Cardiology*, 58(18):1893–1902, 2011.
- [90] P. S. Cuculich, Y. Wang, B. D. Lindsay, M. N. Faddis, R. B. Schuessler, R. J. Damiano, L. Li, and Y. Rudy. Noninvasive characterization of epicardial activation in humans with diverse atrial fibrillation patterns. *Circulation*, 122:1364–1372, 2010.
- [91] R G Wise, C L Huang, A I Al-Shafei, T A Carpenter, and L D Hall. Geometrical models of left ventricular contraction from mri of the normal and spontaneously hypertensive rat heart. *Physics in Medicine and Biology*, 44(10), 1999.
- [92] F. Czegledy, N. Aebischer, A. Tarnari, and A. Tortolani. A new mathematical model for right ventricular geometry. In *Proceedings of the Twelfth Annual International Conference of the IEEE Engineering in Medicine and Biology Society*, pages 1813–1814, nov 1990.